Surface Tension Driven Water Pumping: A Bio-Inspired Passive Water Pump

by
Justin Fraser

Thesis presented in partial fulfilment of the requirements for the degree
of Master of Engineering (Mechanical) in the
Faculty of Engineering at Stellenbosch University

Supervisor: Robert T Dobson

March 2015

DECLARATION

By submitting this thesis electronically, I declare that the entirety of the work contained therein is my own, original work, that I am the sole author thereof (safe to the extent explicitly otherwise stated), that reproduction and publication thereof by Stellenbosch University will not infringe any third party right and that I have not previously in its entirety or in part submitted it for obtaining any qualification.

Signature Date

Justin Fraser

ABSTRACT

The purpose of this study is to construct and test a surface tension driven water pump. The surface tension driven water pump is a passive water pump which uses a similar mechanism to that of trees to pump water. This study was conducted at the Department of Mechanical and Mechatronic Engineering at the University of Stellenbosch.

For the study an extensive literature survey was done encompassing aspects such as water properties, surface tension (basic principles, capillary forces, temperature and contaminant effects, wettability), bubble formation (nucleation theory and tensile strength of water) and, finally water and mineral transport in trees (plant structures and mechanisms, limiting factors, misconceptions and organic substance transport). Previous work by botanists who demonstrate the transpiration mechanism needed for water transport in trees was also considered. The study further required the development of a theoretical thermal-hydraulic model to simulate the pumping performance for the surface tension driven water pump. The developed water pump was also experimentally tested with particular focus on design improvement, pumping performance, pump behaviour, potential pumping head as well as water collection capability. The experimental data was statistically analysed by multi-linear regression. Both the experimental data and statically generated predictions were compared to the theoretical thermal-hydraulic model.

The results show that a working surface tension driven pump was constructed. Evaporation rates of up to 400 mL/hr.m^2 were obtained, with pumping head heights reaching up to 1.8 m and a maximum pump functional lifespan of 13 days. The results further suggest that there is a good correlation between the various statistical fits and the experimental data. The developed theoretical thermal-hydraulic model was also found to be in good agreement with the experimental results. A sensitivity analysis of the theoretical and statistical models showed that the statistical models fairs poorly under extrapolation. Additionally, the mechanistic causes of pump failure as well as the effect of heat and pumping head on water pumping performance were identified. Thereafter, the water collection efficiency was established to be 98% on average. Further testing revealed that the pumping performance of larger area or multiple grouped “leaves” are less accurately predicted with the theoretical model than a single “leaf”.

In conclusion, the results provide some support that the surface tension driven pump may be used as a water transport system in an artificial photosynthesis project, if the functional lifespan of the pump can be greatly improved. It is recommended that a more rigid hydrophilic material be used in the “leaf” interface and that multiple narrower conduits be used instead of a single larger pipe. Additional future work may include the development of pit-like structures to prevent air spreading throughout the system as well as a simple mechanism for evaporative control.

OPSOMMING

Die doel van hierdie ondersoek is om 'n oppervlakspanning-aangedrewe waterpomp te bou en te toets. Die oppervlakspanning-aangedrewe waterpomp is ‘n passiewe waterpomp wat gebruik maak van ‘n meganisme soortgelyke aan dié van bome om water te pomp. Hierdie ondersoek is by die Departement Meganiese en Megatroniese Ingenieurswese by die Universiteit van Stellenbosch uitgevoer.

Vir die ondersoek is 'n uitgebreide literatuurstudie gedoen wat aspekte soos water eienskappe, oppervlakspanning (basiese beginsels, kapillêre kragte, die uitwerking van temperatuur, onsuiwerhede asook benatbaarheid), lugborrelvorming (kernvormingsteorie en die treksterkte van water) en uiteindelik water- en mineraalvervoer in bome (plantstrukture en -meganismes, beperkende faktore, wanpersepsies en die vervoer van organiese stowwe) insluit. Vorige navoring deur plantkundiges, wat die watervervoermeganismes in bome demonstreer, is ook in ag geneem. Die ondersoek het die ontwikkeling van 'n teoretiese termies-hidrouliese model ingesluit, wat gebruik is om die oppervlakspanning-aangedrewe waterpomp se werking te voorspel. Die waterpomp is ook eksperimenteel getoets met die fokus op ontwerpverbetering, pompwerkverrigting, pompwerking, potensiële pompopvoerdrukhoogte sowel as die waterversamelingsvermoë. Die eksperimentele data is statisties ontleed deur middel van meervoudige liniêre regressie. Beide die eksperimentele data en statisties-gegenereerde voorspellings is vergelyk met die teoretiese termies-hidrouliese-model.

Die resultate toon dat 'n werkende oppervlakspanning-aangedrewe pomp gebou is. ‘n Verdampingstempo van tot 400 mL/hr.m^2, pompopvoerdrukhoogte van tot 1.8 m en 'n maksimum funksionele pompleeftyd van 13 dae is bereik. Die resultate dui verder daarop dat daar 'n goeie korrelasie tussen die verskillende statistiese lynpassings en die eksperimentele data is. Die teoretiese termies-hidrouliese-model wat ontwikkel is, toon 'n goeie ooreenkoms met die eksperimentele resultate. 'n Sensitiwiteitsanalise van die teoretiese en statistiese modelle het getoon dat die statistiese modelle swak voorspellings maak as geëkstrapoleerde data gebruik word. Verder is die meganismes wat pompweiering veroorsaak, die effek van hitte asook die effek van pompopvoerdrukhoogte op die pomp se werkverrigting geïdentifiseer. Daarna is die doeltreffendheid van waterversamelingsvermoë vir die waterpomp vasgestel op gemiddeld 98%. Verdere toetse het getoon dat die pompwerkverrigting van groter gegroepeerde "blare" minder akkuraat met die teoretiese model voorspel word as vir 'n enkele "blaar".

Ten slotte: Die resultate toon dat die oppervlakspanning-aangedrewe waterpomp as 'n water vervoer stelsel gebruik kan word in 'n kunsmatige fotosinteseprojek, indien die funksionele leeftyd van die pomp verbeter kan word. Dit word aanbeveel dat 'n sterker hidrofiliese materiaal in die "blaar"-koppelvlak gebruik word en dat verskeie nouer leipype gebruik word in plaas van 'n enkele groter pyp. Bykomende toekomstige werk kan die ontwikkeling van put-agtige strukture insluit wat die

verspeiding van lug deur die hele stelsel voorkom, sowel as 'n eenvoudige meganisme wat die verdampingstempo beheer.

ACKNOWLEDGEMENTS

I would like to express my gratitude to the following people who supported me throughout the entirety of the project. I give thanks to my supervisor, Mr. Dobson for all his effort, belief and patience. Further, to Mr. F. Zietsman who helped to construct the surface tension driven water pump. I especially thank my family and friends who continually encouraged me.

TABLE OF CONTENTS

LIST OF FIGURES

LIST OF TABLES

NOMENCLATURE

A_c	Cross sectional area
A_s	Surface area
A_2	Linear statistical fit constant
a	Van der Waals constant
a_1	Exponential statistical fit constant
B_2	Linear statistical fit constant
b	Van der Waals constant
b_1	Exponential statistical fit constant
C	Constant
C_2	Linear statistical fit constant
c_1	Exponential statistical fit constant
D_{AB}	Mass diffusivity
$D_{H20-air}$	Mass diffusivity of water in air
D_2	Linear statistical fit constant
d_1	Exponential statistical fit constant
E_{LJ}	Lenard Jones potential
EM	Error Margin
e_1	Exponential statistical fit constant
F	Force
g	Gravitational constant
h	Pumping head
h_{mass}	Convective mass transfer coefficient
K	Integration constant
L_c	Characteristic length
L_{cap}	Capillary length
$\dot{m}$	Mass flow rate
P	Pressure

P_0	Equilibrium vapour pressure for planar liquid surfaces
$\dot{Q}$	Heat transfer rate
R	Flow resistance
R^2	Coefficient of determination
R_{GC}	Specific gas constant
RH	Relative humidity
r	r-direction (radial) or radius
r_m	Molecular spacing
r_{m0}	Molecular spacing for a zero inter-particle potential
r_1	Primary interfacial curvature
r_2	Secondary interfacial curvature
T	Temperature
T_c	Critical temperature
t	Time
t_w	Wall thickness
u	Fluid velocity
$\dot{V}$	Volume flow rate
$\dot{V}"$	Volumetric flux rate
v	Specific volume
v_{air}	Air velocity
v_{avg}	Average flow velocity
v_f	Fluid velocity
w	Net reversible work per unit area
x	x-direction (flow direction)
x_A	Concentration of specie A
z_i	Equilibrium column height

Greek

α	Pipe incline angle (counter clockwise)

Γ_A	Surface excess mass of species A
ΔP	Pressure difference
Δr	Infinitesimal length in r-direction
Δx	Infinitesimal length in x-direction or pipe section length
$\Delta \phi$	Infinitesimal length in ϕ-direction
ε	Potential well depth
θ	Contact angle
κ	Intrinsic permeability of porous material
λ_k	Kelvin length
μ	Dynamic fluid viscosity
ν	Kinematic viscosity
ρ	Density
σ	Surface or interfacial tension
σ_{stress}	Normal stress
σ_x	Normal fluid stress component
τ_{rx}	Fluid shear stress
ϕ	ϕ-direction (circumferential)
$\emptyset$	Diameter

Subscripts

I	Bulk fluid I
II	Bulk fluid II
1	Point/condition 1
2	Point/condition 2
amb	Ambient
bub	Bubble
c	Cross sectional
cap	Capillary
$collected$	Collected

CV	Control volume
d	Dispersion forces
$entry$	Entry region
f	Fluid
g	Gas
$grav$	Gravity
h/m	Hydrogen or metallic bonds
LL	Liquid-Liquid interface
LG	Liquid-gas interface
LV	Liquid-vapour interface
l	Liquid
$leaf$	Artificial leaf
$lower$	Lower confidence bound
$upper$	Upper confidence bound
$pipe$	Pipe
$pred$	Predicted
$rx + \Delta r$	Point Δr further in r-direction
SL	Solid-liquid interface
SG	Solid-gas interface
SG,d	Solid-vapour interface, dispersion forces
SV	Solid-vapour interface
s	Surface
sat	Equilibrium saturation condition
t	Tube
tot	Total
v	Vapour
$valve$	Valve
v,s	Vapour, at surface
v,∞	Vapour, in free stream
w	Wall

x	x-direction component
$x + \Delta x$	Point Δx further in x-direction
σ	Surface tension

Abbreviations /Acronyms

PCD	Pitch circle diameter
PVA	Polyvinyl alcohol
SEM	Scanning electron microscope
PVC	Polyvinyl Chloride
SS	Stainless steel

1. INTRODUCTION

Water pumping is an essential part of daily life and allows access to much needed water. Nature, over millions of years, has found efficient ways to solve its problems. Biomimicry is a discipline that imitates designs and processes found in nature as creative, efficient and economical solutions to modern day problems (IBTimes, 2012; Leybovich, 2012). It is observed in nature that trees and plants are able to draw water from deep underground up to their leaves and shoots, as is simplistically shown in Figure 1.1, to be used in processes such as photosynthesis. The drive to develop "green" technologies has become quite important with emphasis on the reduction of carbon emissions (Banks, 2009). These imperatives have "inspired" the development of an "artificial" tree or a tree bio-inspired passive water pump.

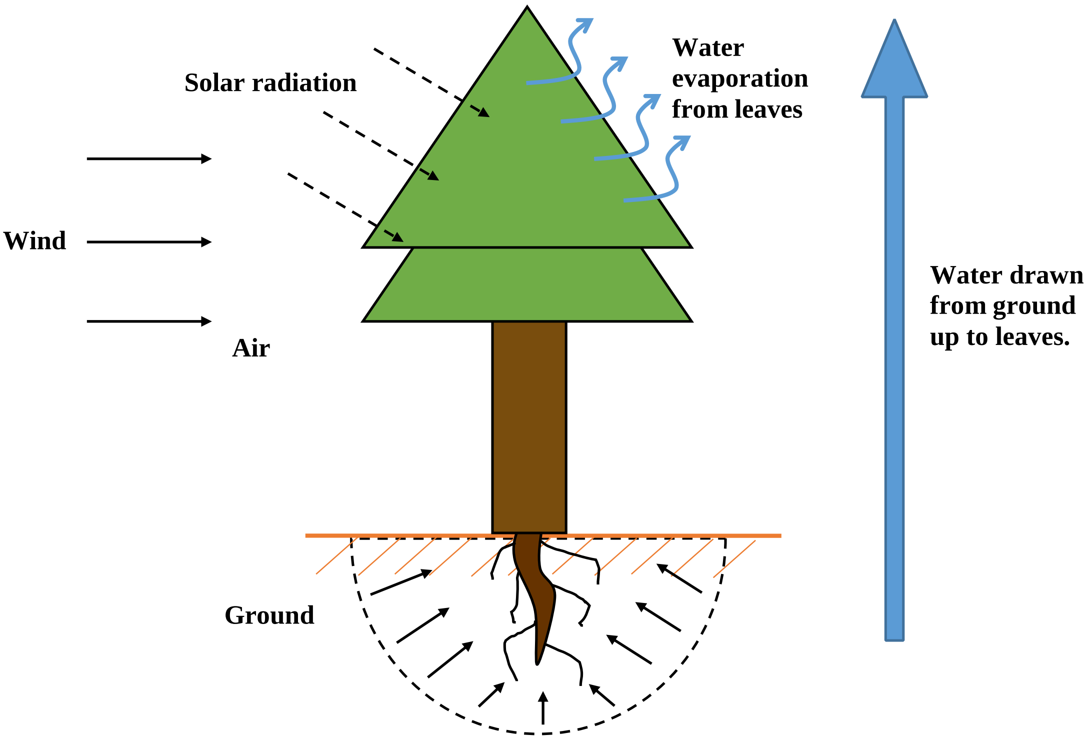

Figure 1.1: Simplified diagram of overall water transport in trees

This project is an in depth study of plant water and solute transport mechanisms as well as the surface tension phenomena with the purpose to construct a passive mechanical/"artificial" tree-like pump. The project was proposed by Mr R.T. Dobson and is the first step in a larger project where hydrogen, food (carbohydrates) and fuel will be artificially produced (Dobson, 2012) as conceptually shown in Figure 1.2. The thesis forms part of Mr J. Fraser's Mechanical Engineering Project 878 for the degree of Master of Engineering. The project is supervised by Mr R.T. Dobson. This report focuses on the objectives and motivations for the project, the literature overview necessary for the project, the surface tension driven water pump design, the experimentation conducted, the results obtained as well as a discussion thereof and concludes with some final remarks.

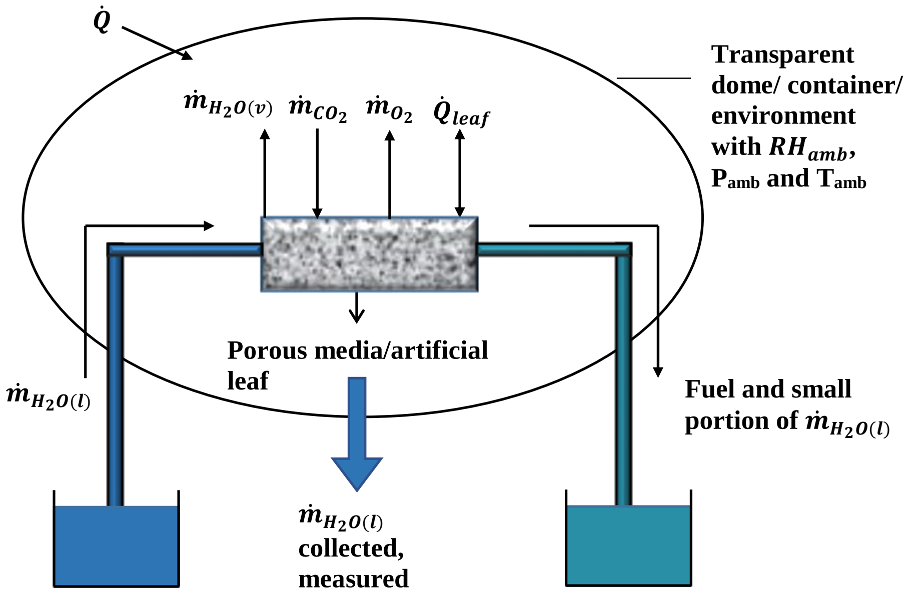

Figure 1.2: Conceptual diagram of an artificial photosynthesis process

1.1. Motivation

Engineers and designers often look in nature for solutions to modern day problems, which is generally referred to as biomimicry. Examples include honeycomb structures for improved strength of lightweight structures, whale fin inspired wind turbine blades designed for extra lift and efficiency, kingfisher inspired bullet trains (nose) to increase aerodynamics, anti-drag artificial shark skin materials and many more (IBTimes, 2012). Koch and Barthlott (2009) focus on super- hydrophobic and hydrophilic plant surfaces as inspiration for biomimetic materials. They explain the potential for super hydrophobic materials with self-cleaning as well as reduced drag properties and enhanced capillary liquid transport for super hydrophilic materials.

Energy conservation is a key area in biomimicry and natural methods of energy production are being considered. Trees and plants are able to draw water from deep underground to their leaves to be used in processes such as the production of oxygen and carbohydrates during photosynthesis. Giant Redwood trees are able to grow up 100 m tall, and are therefore capable of pumping water to this height. This mechanism of water transport would seem to be a natural, energy efficient and eco-friendly method for water transport. Published research on the use of tree water transport mechanisms for water pumping are fairly limited with some botanists, such as Susman et al. (2009) and Martinez Vilalta et al. (2003), that relate to the subject as an attempt to model water transport in plants for students. Related research includes: the employment of selective hydrophobic patterning on liquids pinned in micro-channels for transpiration-based micro-pumps with continuous ultra-low flow rates by Namasivayam et al. (2003) from Michigan University; microfluidic systems formed in synthetic hydrogel by Wheeler and Stroock (2008) from Cornell University; microfluidic transport through electro-wetting by Berry and Kedzierski (2008) at Lincoln Laboratory; charged-pumping in a synthetic leaf by Borno et al. (2009) from Michigan-, MIT and Berkeley University; artificial leaf wireless solar water splitting by Reece et al. (2011) from MIT and finally artificial trees for carbon absorption (Biello, 2013; Banks, 2009).

Research of water transport mechanisms for larger systems inspired by trees, however, has not seen much development. The study and understanding as well as further development of such systems might facilitate and inspire future designs for eco-friendly processes in industry. Possible applications of such passive water pumps, outside microfluidic water transport, can include: to supply water to an "artificial" leaf which is able to produce fuel, to serve as a stand-alone passive water pump which should work in most environments for green buildings or poverty stricken communities in Africa and be used as efficient cooling for building rooftops.

1.2. Objectives

The project is intended to analyse the mechanisms through which water transport in plants/trees occur. Together with the study of water and solute transport mechanisms in plants it was deemed important to conduct an extensive literature study stretching from water properties, surface tension and bubble formation in liquids to understand the underlying theory which allows the transport of water in plants to occur. Utilising the knowledge gained from the above study a passive mechanical or "artificial" tree-like pump was developed. An experimental simulation of the mechanically constructed water pump was also conducted. A theoretical thermal-hydraulic simulation model was developed to predict the transport mechanism's behaviour and was validated against the experimental model. After validation of the theoretical model, the possible use of such a surface tension driven water pump in an artificial photosynthesis program was established.

2. LITERATURE STUDY

Much research was required to attempt the construction of a surface tension driven pump inspired by plant water transport mechanisms. A short overview of water at a molecular level was conducted followed by a broad study on surface tension. Thereafter, nucleation theory was considered with the primary focus on bubble formation in liquids at non-equilibrium conditions. Finally, plant cells, structures and water transport mechanisms where studied in detail. The most important aspects of surface tension and water transport in plants are listed here in Section 2, however much more background and additional information is given in Appendix F.

2.1. Water Structure

Life as we know it would not be sustainable if it were not for the interesting and remarkable properties of water (Coder, 1999). An illustration of the composition of a water molecule can be seen in Figure 2.1. Water is such an unusual substance that it has been attributed with two special types of intermolecular effects namely, hydrogen bonds and the hydrophobic effect. The high melting and boiling points of water suggests that stronger intermolecular interactions exist than with other common liquids (even highly polar). Water has a maximum density at 4°C as well as a tetrahedral coordination which proposes that water molecules prefer to be farther apart and have less dense lattice packing characteristics. Further, water has a low compressibility and unusual solubility properties where it can be either solvent or solute (Israelachvili, 2011). The structure of water molecules allow it to attach to each other and form clusters through the process of *cohesion*. Alternatively, *adhesion* is the process where water molecules are attracted to polarizable or charged surfaces/substances (Peramaki, 2005; Coder, 1999).

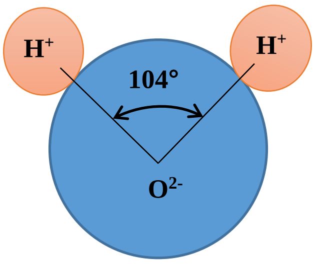

Figure 2.1: Composition of a water molecule [Modified from Peramaki (2005)]

Hydrogen bonds exist in varying degrees between covalently bound H^+ atoms with electronegative atoms (such as O, N, F, as well as Cl). Therefore hydrogen bonds are not distinctive only to water. It has been generally accepted that the hydrogen bond is predominantly an electrostatic interaction and has been found to be much stronger than van der Waal's bonds, but weaker than covalent, ionic or metallic bonds (Israelachvili, 2011). Water molecules will tend to rather bond with each other when it comes into contact with non-polar molecules which are unable to form hydrogen bonds. The water molecules attempt to configure themselves such that the greatest amount of the four charges per molecule will have a hydrogen bond. In other words, the water molecules will arrange themselves to point the least number of tetrahedral charges toward the most unaccommodating species to allow other charges to partake in hydrogen bonding. The nature of the incompatibility of inert substances in water is known as the *hydrophobic effect*. Such substances are called *hydrophobic substances* and in the same way surfaces which are not wetted by water are called *hydrophobic surfaces*. On such surfaces water tends to form small lenses or balls and characteristically have large contact angles (Israelachvili, 2011).

Certain molecules or groups that are water soluble tend to prefer to be in contact with the water rather than with themselves. These molecules or groups are called *hydrophilic* and display the predisposition to strongly repel each other in water. Some hydrophilic groups often take up water from vapour and are called hygroscopic. Hydrogels are hydrophilic polymer networks which are able to swell 1000 times their original size due to water uptake. It, however, must also be noted that some uncharged or non-polar molecules with the right geometry are able to form hydrogen bonds with water. Similarly, not all polar groups are hydrophilic nor are all non-polar groups hydrophobic (Israelachvili, 2011). Koch and Barthlott (2009) explain how super hydrophilic and super hydrophobic surfaces are essentially a combination of micro- and nanostructures on surfaces as well as the surface chemistry. Super hydrophobic surfaces are highly non-wetting and display self-cleaning characteristics, whereas super hydrophilic surfaces are highly wetting and increases absorption, spreading and the potential for capillary transport (Koch and Barthlott, 2009).

2.2. Surface Tension

Surface tension is a very important phenomenon in nature and without it life as we know it would not exist. Its phenomenological effect is to create an almost elastic membrane at the surface interface between two fluids and may even deform when weight is placed on it. In nature, surface tension in water allows small insects to stand on water surfaces (Sang Kug et al., 2009) and allow some bacteria to propel on water surfaces (Angelini et al., 2009). Surface tension may be altered locally through the addition of surfactants or temperature differences (Carey, 1992). As proposed by Okawa et al. (2009), sunlight or even lasers may be used as medium to generate localised surface tension gradients. Another more controversial way to locally affect surface tension is by magnetic fields (Amiri and Dadkhah, 2006). There are many other examples where surface tension is used to produce useful work, for example, the mechanism through which a tree transports water from its roots up to its leaves. Further, industries concerned with paints, inks, surface preparation and soil sciences find surface tension of great importance. In this section, surface tension fundamentals will be considered which includes its origin, definitions and resulting consequences.

2.2.1. *Surface Tension Fundamentals*

Surface tension, σ, at the interface between two or more bulk fluids arises due to molecular interactions in the interfacial region. The interfacial region is defined as a very thin region, typically only a few molecules wide. In this region the transition from one bulk fluid to another occurs and therefore rapid changes in the fluid/material properties, such as density, occur within this region (Carey, 1992). When considering a liquid-vapour interface, the interfacial region may be seen as in Figure 2.2. Within the bulk liquid phase the molecules are densely packed, whereas, in the interfacial region the molecules start to become less dense until the bulk vapour phase is reached and the molecules are packed loosely. Figure 2.2 may also be interpreted with respect to the material density as shown in Figure 2.3.

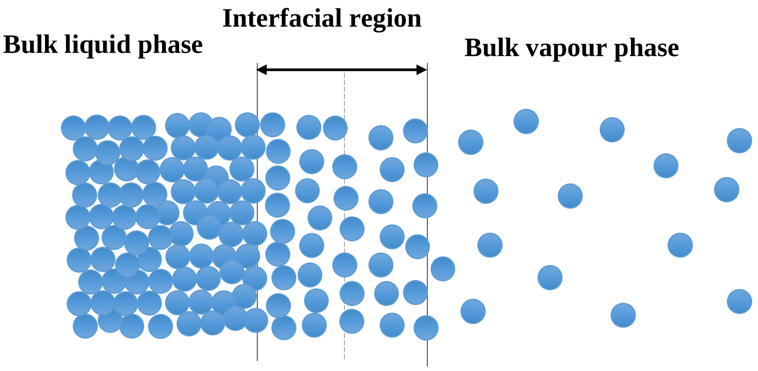

Figure 2.2: Molecular spacing across interfacial region for liquid-vapour interface [Modified from Carey (1992)]

The reason why interfacial tension exists is due to molecular forces interacting on one another. The Lenard-Jones intermolecular potential, shown in Figure 2.4, may be used to describe the repulsive and attractive nature of molecules depending on the distance to their neighbouring molecules. From Figure 2.4 it can be seen that for molecules spaced $r_m < r_{m0}$, a strongly repulsive interaction will dominate and for molecules spaced $r_m > r_{m0}$, a strongly attractive interaction will dominate (Carey, 1992).

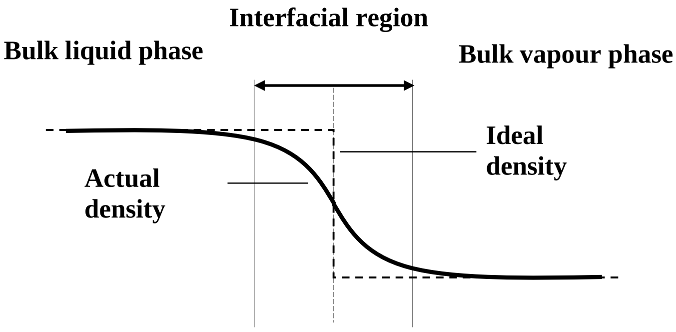

Figure 2.3: Density distribution across liquid-vapour interface [Modified from Carey (1992)]

The reason why surface tension exists and why it is parallel to the surface (and perpendicular to the density gradient) can be explained through a force interpretation of the molecular interactions as described by Carey (1992). The molecular force interaction is conceptually explained in Figure 2.5. Considering a case as shown in Figure 2.3 a molecule which is within the bulk liquid is fully balanced by repulsive and attractive forces due to molecular interactions equal from all sides. Molecules in the bulk liquid will experience repulsive forces from close neighbouring molecules and attractive forces from all others. On average the resultant force on a molecule is zero, because both attractive and repulsive forces act symmetrically in all directions. This is due to the average molecular spacing being uniformly spread throughout the bulk liquid.

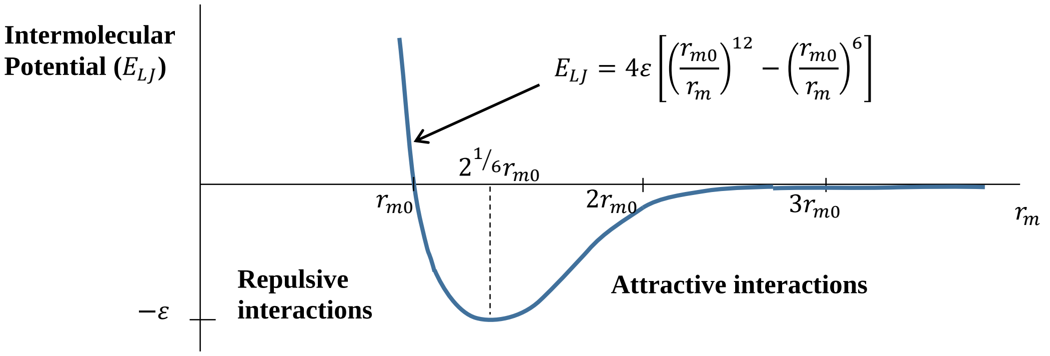

Figure 2.4: Lenard-Jones intermolecular potential (E_{LJ}) [Modified from Carey (1992)]

The Lenard-Jones model shows that close range repulsive forces vary rapidly with molecular spacing as opposed to the longer range attractive forces. In the interfacial region, the mean spacing of molecules perpendicular to the interface is greater than in the bulk liquid and is increasing until the bulk vapour is reached. A minor increase in molecular spacing leads to the repulsive forces being weakened significantly where the attractive forces from the bulk liquid side will not be significantly affected. At the same time, the bulk vapour phase average molecular spacing is much greater than that of the bulk liquid and the resultant attractive and repulsive interactions have almost no effect on molecules at the interface. This combination results in a force imbalance which draws molecules closer to the bulk liquid such that the molecular spacing normal to the interface decreases slightly until the attractive and repulsive forces, perpendicular to the interface, are balanced.

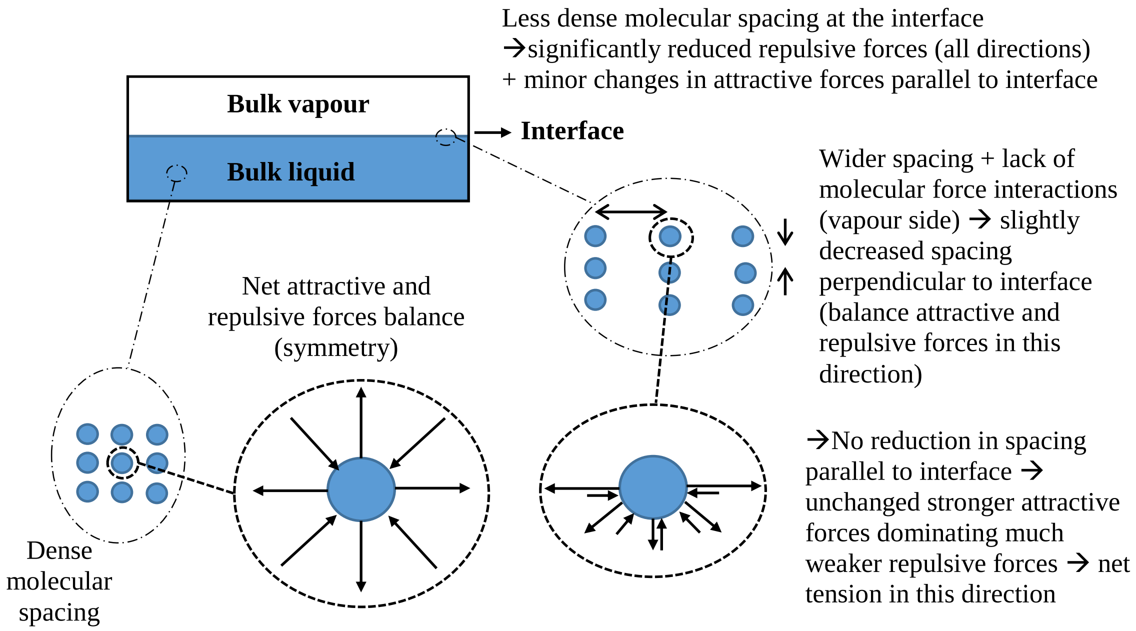

Figure 2.5: Summary of surface tension

However, parallel to the interface the density distribution remains more or less uniform on all sides of the molecules. Therefore, there is no force imbalance to decrease the mean molecular spacing in this direction which would have resulted in much smaller attractive forces parallel to the interface. The significantly decreased repulsive forces, at the interface, coupled with much stronger attractive forces, parallel to the interface, induces a net tension among the molecules at the interface. This net tension is parallel to the interface and equal in all directions (Carey, 1992). Liquid molecules at the interface are at an unfavourable energy state is the fundamental reason why surface tension tries to minimise the fluid surface area. Due to the various intermolecular forces, the total surface tension may divided into a contribution from dispersion forces, σ_d, and forces arising from hydrogen or metallic bonds, $\sigma_{h/m}$, (Carey, 1992) and shown as

$$\sigma = \sigma_d + \sigma_{h/m} \tag{2.1}$$

Table 2.1 is taken from Carey (1992) and shows examples of a metallic, polar and non-polar liquid with their respective surface tensions. The reason why non-polar liquids have much weaker surface tensions than water can be explained thus; the molecular forces due metallic bonds prevalent in liquid metals are much higher than the forces due to hydrogen bonds, found in water. Therefore, the surface tension due to the metallic bonds are larger than the surface tension due to the hydrogen bonds. In non-polar liquids the presence of either metallic or hydrogen bonds are absent. Thus only the surface tension contribution due to dispersion forces are present and consequently the net surface tension is much lower for non-polar liquids.

Table 2.1: Surface tension for various liquids in contact with air or its own vapour at saturation

Liquid	Temperature (°C)	Surface tension (mN/m)
Mercury (Hg)	20	484
Water (H_2O)	20	72.8
n-Butanol ($C_4H_{10}O$)	20	24.6

2.2.2. *Capillary Forces*

Capillary forces are a direct result of surface tension and it occurs at all times. One example is the building of sand castles where the dry sand is not able to hold much shape, but the addition of some water to wet the sand allows for more complex shapes to be built. The forces due to a liquid meniscus are called capillary forces. These forces are not only due to liquid menisci present in a gaseous environment but may be formed due to a capillary bridge as result of one liquid in another immiscible liquid. The importance of capillarity is quite evident as fields concerning powders, soils, granular materials, adhesion between particles to surfaces, sintering of ceramic and/or metallic particles all deal with capillary forces (Butt and Kappl, 2009).

There are three fundamental equations used to describe liquid surfaces. The Young-Laplace equation describes the shape of a liquid surface and ultimately relates the interfacial pressure difference to the interface geometry at equilibrium as well as the surface tension. The Kelvin equation relates the curvature of a liquid's surface to its vapour pressure. Thirdly, Young's equation describes the liquid-vapour-solid interaction as well as the wetting of a liquid on solid surfaces (Butt and Kappl, 2009).

2.2.2.1. Young-Laplace Equation

The Young-Laplace equation for small systems may be written as follows (Carey, 1992)

$$\Delta P = \sigma \left(\frac{1}{r_1} + \frac{1}{r_2} \right) \tag{2.2}$$

where ΔP is the pressure difference across the interface (also called the Laplace pressure), σ is the surface tension, r_1 and r_2 are the radii of curvature. The pressure difference may be defined as

$$\Delta P = P_I - P_{II} \tag{2.3}$$

which signifies the pressure difference between a bulk fluid *I* and bulk fluid *II*. If we consider a typical liquid-vapour interface, the definition of the Laplace pressure is typically

$$\Delta P = P_l - P_g \tag{2.4}$$

The local curvature is then defined with respect to bulk fluid *I*, where a concave interface is positive, as seen in Figure 2.6(a). Two examples of very simple interface curvatures can be seen in Figure 2.6 (b) and (c). It is clear that for the case of a spherical interface curvature, the radius of curvature will be: $r_1 = r_2 = r_s$. For the second case, however, the cylindrical shape presents a planar axis. Thus the radius of curvature will be: $r_1 = r_s$ and $r_2 = \infty$. The Young-Laplace equation has some important implications. If the shape or curvature of the interface is known, the pressure difference may be calculated. The pressure inside the fluid will remain uniform if there are no external forces, such as gravity, acting on the fluid. This implies the Laplace pressure is constant and the interface curvature remains the same everywhere. Otherwise the flow of fluid from high to lower pressure regions would be observed. Finally, the equilibrium shape of the interface may be determined if the pressure difference is known (Butt and Kappl, 2009).

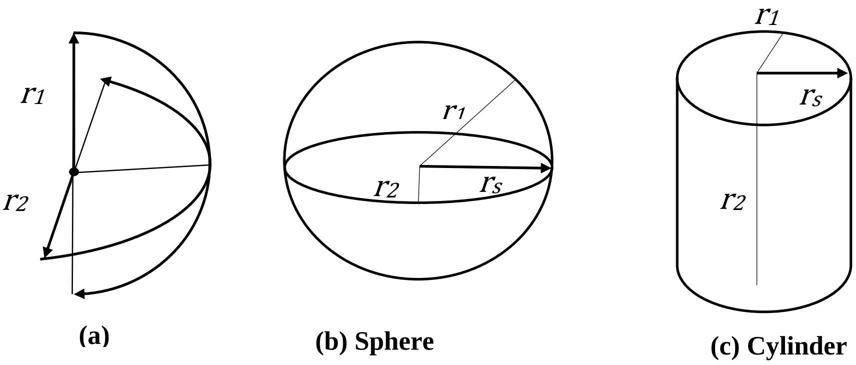

(a) (b) Sphere (c) Cylinder

Figure 2.6: Local geometry of interface curvature

There are numerous examples of interfacial curvatures that can be determined using the Young-Laplace equation. Examples of interface geometries such as a sessile drop can be found in Appendix F.1.1. The difficulty of finding analytical solutions for certain problems are rather tedious and numerical solutions may be preferred. It is, however, useful to develop analytical solutions where possible as some useful and dimensionless numbers and key parameters may be found, such as the capillary length, L_{cap} (Carey, 1992).

$$L_{cap} = \left[\frac{\sigma}{(\rho_l - \rho_g)g}\right]^{1/2} \tag{2.5}$$

The following equation regarding capillary tubes, as shown in Figure 2.7, can easily be derived with either the Young-Laplace equation, described in Carey (1992), or by a simple force balance method.

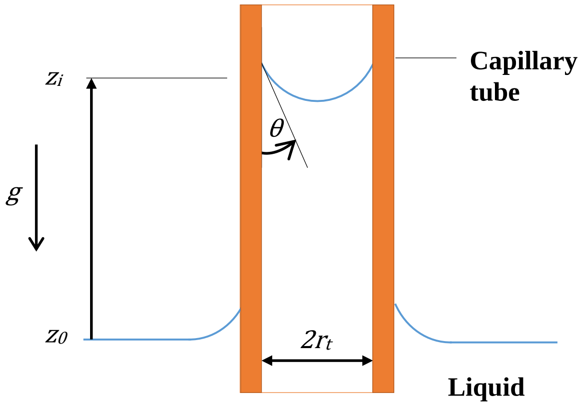

Figure 2.7: Capillary tube [Modified from Carey (1992)]

With the assumption that the liquid has a free surface with an extensive area, that the liquid is wetting ($\theta < 90°$) and that the tube radius, r_t is much less than the capillary length, Equation 2.6 then describes the equilibrium height of the column. It indicates that as the tube radius becomes smaller z_i may become quite large. This explains why blotting paper, which has very fine pores, is able to exert strong "suction" on wetting fluids such as water (Carey, 1992).

$$z_i = \left[\frac{2\sigma\cos(\theta)}{g(\rho_l - \rho_g)r_t}\right] \tag{2.6}$$

If the fluid were to be non-wetting ($\theta > 90°$) the above equation is still valid and it is clear that z_i will be negative. More on derivation of capillary forces and analysis of interface geometries can be found in Butt and Kappl (2009). The basic principles involved in surface tension are usually employed in the measurement thereof. Appendix F.1.2 discusses the various methods of surface tension measurement.

2.2.2.2. Kelvin Equation

Vapour pressure is the pressure a vapour exerts with its condensed phase at a certain temperature when in thermodynamic equilibrium, in a closed system. This is also understood as the mean saturated vapour pressure and gives an indication of how volatile a liquid might be. Saturated liquid tables, found in many sources, contain the vapour pressures for various liquids. These vapour pressures however are based on liquids in closed systems that are in thermodynamic equilibrium and of having planar interfacial surfaces. Butt and Kappl (2009) states that the liquid interface curvature has an effect on the vapour pressure. The Kelvin equation relates the equilibrium vapour pressure to the interfacial curvature and is derived from the Young-Laplace equation as well as the ideal gas equation. An interfacial curvature resulting in an increase in the Laplace pressure will produce an increase in vapour pressure. An example would be a liquid droplet, where the interfacial curvature results in a positive Laplace pressure which causes the liquid droplet molecules to evaporate more easily. On the other hand, for a bubble surrounded by a liquid, the resulting Laplace pressure is negative. Therefore, a reduction in vapour pressure will be noted. Thus molecules will evaporate with more difficulty into the bubble. The Kelvin equation is expressed by (Butt and Kappl, 2009)

$$R_{GC}T\ln\frac{P_v}{P_0} = \sigma\left(\frac{1}{r_1} + \frac{1}{r_2}\right) \tag{2.7}$$

where P_v is the resulting vapour pressure, P_0 is the equilibrium vapour pressure for planar liquid surfaces or P_{sat}, R_{GC} is the specific gas constant, T is the temperature in K and r_1 and r_2 are the radii of curvature for the interface. Consider now a liquid drop in a gaseous environment. From the previous section, a spherical drop's surface curvature is known, and by applying Equation 2.7 it can be found that

$$R_{GC}T\ln\frac{P_v}{P_0} = \left(\frac{2\sigma}{r_s}\right) \tag{2.8}$$

After rearranging, the above equation becomes

$$P_v = P_0 \exp\left(\frac{2\sigma}{R_{GC}Tr_s}\right) \tag{2.9}$$

and when imposing the following

$$\lambda_k = \frac{2\sigma}{R_{GC}Tr_s}$$

becomes

$$P_v = P_0 \exp(\lambda_k) \tag{2.10}$$

where λ_k is the Kelvin length. The Kelvin length gives an indication of how volatile a liquid is and can be found in many sources such as Butt and Kappl (2009). From the above expression it is clear that smaller drops have resulting higher vapour pressures. Thus more liquid evaporates from smaller drops and tend to condense on larger drops. Therefore, larger drops can be said to grow at the expense of smaller drops. This is known as Ostwald ripening. A critical drop size is said to exist, where drops smaller than this size will evaporate and larger drops will grow. Through this the existence of oversaturated vapours or fog can possibly be explained (Butt and Kappl, 2009). Through the application of the Kelvin equation to a simple capillary tube as shown in Figure 2.7 it can be shown that

$$P_v = P_0 \exp\left(\frac{-2\sigma\cos(\theta)}{R_{GC}Tr_s}\right) \tag{2.11}$$

From Equation 2.11 it is evident that the vapour pressure is reduced due to the meniscus and that the degree thereof will be related to the contact angle and capillary radius. Therefore lower contact angles and smaller capillary radii will result in reduced vapour pressures as well as lower evaporation rates.

2.2.3. *Temperature and Contaminant Effects on Surface Tension*

The surface tension between two bulk fluids can be varied through certain mechanisms such as contaminants, temperature and magnetism (Amiri and Dadkhah, 2006). If these mechanisms are employed correctly, surface tension gradients can be formed which effectively pulls liquid from regions of weaker surface tension to regions of higher surface tension. When surface tension non-uniformities are somehow maintained, the resulting pulling action due to the surface tension gradients may be balanced locally by viscous shear stresses in the flow and a steady flow pattern may emerge. The motion of liquid due to surface tension gradients at the interface is called the Marangoni effect (Carey, 1992). More on the Marangoni effect can be found in Appendix F.1.3. The effects of temperature and concentration of contaminants on surface tension will be further discussed. More detail can be found in Carey (1992) as well as Butt et al. (2006) on temperature and contaminant effects. The effects of magnetism on surface tension is still controversial and Amiri and Dadkhah (2006) explains more on the subject.

2.2.3.1. Temperature Effects

Consider a pure liquid in contact with its vapour. As the temperature of the liquid is increased to a certain critical temperature, the properties of the two fluids will eventually become identical at the interface. Thus the surface tension will ultimately disappear. Thus, it is possible to deduce that an increase in temperature will effectively decrease surface tension and ultimately cause it to vanish when the critical temperature, T_c,is reached. Below is an empirically interpolated relation which describes the surface tension for pure water in contact with its own vapour with respect to temperature (Carey, 1992).

$$\sigma = 235.8\left(1-\frac{T_{sat}}{T_c}\right)^{1.256}\left[1-0.625\left(1-\frac{T_{sat}}{T_c}\right)\right] \qquad (2.12)$$

where all temperatures are in K and the resulting surface tension is in mN/m. The equation is valid for temperature ranges between 0.01 and 300 °C and is accurate to $\pm 0.5\%$. Above 300 °C the data deviates by only 13%. Due to the almost linear decrease in surface tension with temperature for most liquids, the following equation was developed: (Carey, 1992)

$$\sigma = C_0 - C_1 T \qquad (2.13)$$

where T is in °C and C_0 as well as C_1 can be found in Table 2.2, which is a modified selection from Carey (1992).

Table 2.2: Surface tension constants for various substances [Modified from Carey (1992)]

Substance	C_0 (mN/m)	C_1 (mN/m.°C)	Temperature range (°C)
Mercury	490.6	0.2049	5 ↔ 200
Water	75.83	0.1477	10 ↔ 100
Acetone	26.26	0.1120	25 ↔ 50

2.2.3.2. Contaminant Effects

Surface tension is typically a strong function of contaminant concentration. Thus the presence of additional substances dissolved in the liquid is a major factor that influences surface tension. Take a mixture of two species where species A and B are the solute and solvent, respectively, in which species A displays ideal mixture behaviour in species B. It can be shown that the surface excess mass of species A, Γ_A is related to the change in surface tension with concentration of species A (Carey, 1992)

$$\Gamma_A = -\left(\frac{x_A}{R_{GC}T}\right)\left(\frac{\partial\sigma}{\partial x_A}\right)_T \qquad (2.14)$$

where x_A is the solute concentration. From the above equation it can be seen that as the concentration of the solute increases and the surface tension decreases with it simultaneously, the solute will tend to accumulate at the surface. Solutes that exhibit this behaviour are deemed surface-active materials. If the surface-active material concentrates at the interface to the extent that it significantly alters the surface tension, it is called a surface-active agent or more commonly a surfactant. Typical surfactants are household soaps and detergents in liquid water. The soap structure contains a polar and non-polar (hydrocarbon chains) group. Due to the water's aversion for the non-polar groups and its affinity towards the polar groups, the soap will form a monomolecular layer at the water-vapour interface as seen in Figure 2.8.

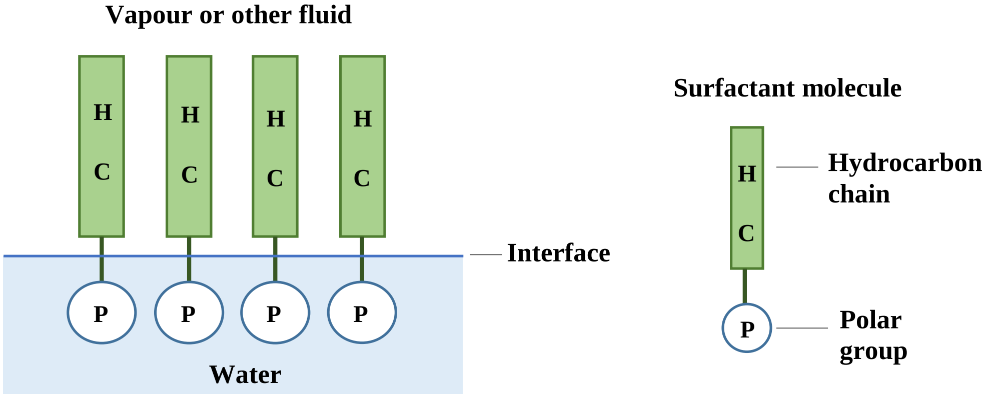

Figure 2.8: Typical orientation of surfactant molecules at interface [Modified from Carey (1992)]

This configuration is preferred and therefore soap molecules will concentrate at the interface which results in the reduction of surface tension (Carey, 1992). Because there are many different types of polar groups, even a minute amount of many various substances may act as a surfactant in water. It is therefore quite easy to alter the surface tension of water and because of this contamination should be considered when dealing with interfacial phenomena (Carey, 1992).

It has been shown that the presence of another species in the interfacial region will decrease the surface tension and that the concentration of that species will be higher at the interface than in the bulk fluid. This effect gives rise to a change in the interfacial composition and lowered surface tension from the bulk fluid, for a mixture of fluids. In most cases the pure fluid with the lowest surface tension will tend to have a higher concentration at the interface region. Therefore the resulting surface tension from a mixture will not simply be equal to the mole fraction average of the pure component surface tensions. Generally, the mixture surface tension is less than the mole fraction average of the pure component surface tensions and can be of a highly non-linear relationship. There are numerous proposed computational methods to predict mixture surface tensions. However, there is no single model that can accurately predict the resulting surface tension for all mixture concentrations (Carey, 2008).

2.2.4. *Wettability and Contact Angles*

In the study of interfacial phenomena, most commonly a liquid-vapour phase is in contact with a solid surface or wall. The manner in which the two phases contact the solid wall will greatly affect the heat and mass transfer of the system. Therefore, this is especially important for heat transfer equipment where condensation or vaporisation occurs. The liquid-vapour contact with a solid may vary with different liquids as well as solids. The affinity liquids have for solids is quite often referred to as wettability. In general liquids with weak affinities for solids will collect themselves into discrete drops where liquids with high affinities for solids will tend to spread and form a thin film. The contact angle, θ, is a measure to quantify the wettability of a liquid. The contact angle is the angle that a tangent line to the liquid-vapour surface makes with the solid surface. A liquid is said to be wetting if the contact angle is between 0° and 90°. For contact angles between 90° and 180°, the liquid is considered to be non-wetting. Thus as θ approaches 0°, the liquid will in fact spread more over the surface, as can be seen in Figure 2.9 (Carey, 1992; Çengel and Cimbala, 2010).

2.2.4.1. Young's Equation

It is important to note when analysing the contact line of a liquid, vapour and solid in contact, that the system has three interfaces, namely, a liquid-vapour (LV) interface, a solid-liquid (SL) interface and a solid-vapour (SV) interface, as shown in Figure 2.9. Each interface has its own associated interfacial tension, that is, σ_{LV}, σ_{SL} and σ_{SV}, where σ_{LV} is commonly just referred to as surface tension, σ. At equilibrium, the force balance at the contact line of the liquid yields the following interfacial tension relation (Carey, 1992)

$$\sigma_{LV}\cos\theta = \sigma_{SV} - \sigma_{SL} \tag{2.15}$$

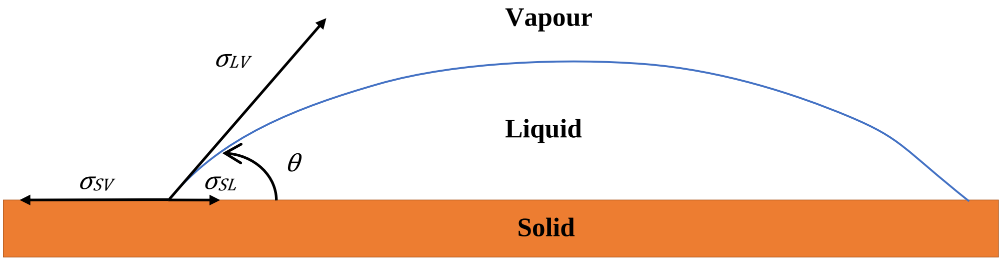

Figure 2.9: Surface tension on contact line [Modified from Carey (1992)]

This expression is commonly known as Young's equation. As seen in Figure 2.9, the vertical reaction force on the solid due to $\sigma_{LV} \sin \theta$ is commonly omitted. This attractive force is usually very small when compared to the large modulus of elasticity of a solid, therefore, deformation of the solid surface is rarely noticed (Carey, 1992). Significant insight can be gained through closer inspection of Equation 2.15. If $\sigma_{SV} - \sigma_{SL}$ is positive, the contact angle will be smaller than 90° and the liquid will wet the surface. Otherwise, if $\sigma_{SV} - \sigma_{SL}$ is negative, the contact angle will be larger than 90° and the liquid will not fully wet the surface. This is an issue when coating hydrophobic surfaces with an aqueous solution, as the thin film will spontaneously rupture (Butt and Kappl, 2009). Young's equation is a relatively simple formulation which does not account for a pre-wetting or adsorbed liquid film on the solid surface. In this case the force balance as well as the liquid-vapour interface will be affected. The equation is also only valid at equilibrium and difficult to apply in practice. This is due to the solid-liquid and solid-vapour interfacial tensions which cannot ordinarily be measured and therefore very little data is available (Carey, 1992).

2.2.4.2. Cohesion and Adhesion

Carey (1992) explains, if one considers a cylindrical column formed by a liquid phase in contact with a solid phase, which are both surrounded by a gaseous phase, as shown in Figure 2.10.

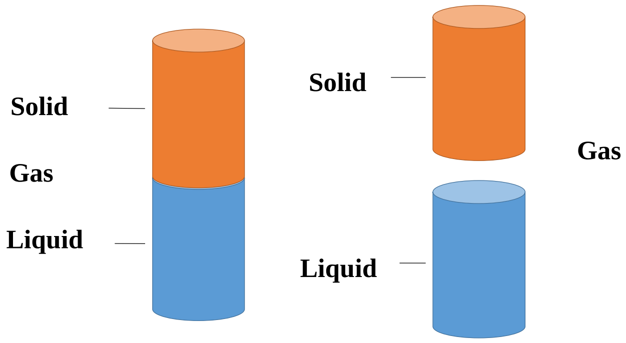

Figure 2.10: Solid-liquid column surrounded by gas [Modified from Carey (1992)]

The net reversible work per unit area required to separate the liquid-solid phase and generate a liquid-gas and solid-gas phase may be represented by

$$w_{SL} = \sigma_{LG} + \sigma_{SG} - \sigma_{SL} \tag{2.16}$$

This minimum (reversible) work required to tear the liquid off the solid is known as the work of adhesion. Similarly, considering two same-liquid columns in contact, the separation thereof will create two new liquid-gas interfaces

$$w_{LL} = 2\sigma_{LG} \tag{2.17}$$

This is called the work of cohesion and is simply the work required to break the internal bonds in the liquid (Carey, 1992). Therefore adhesion forces may be described as the attractive forces between liquid and solid molecules, whereas cohesion forces are the attractive forces between molecules of the same substance.

2.2.4.3. Surface Tension and Contact Angle

Considering a solid-liquid interface in the presence of a gas where the interfacial tensions are mainly due to dispersion forces, the critical surface tension occurs when the surface tension is equal to the solid-gas interfacial tension (Carey, 1992)

$$\sigma_{LG} = \sigma_{SG,d} \tag{2.18}$$

Figure 2.11 shows a combination of surface tension and contact angles found on Teflon for various hydrocarbon liquids.

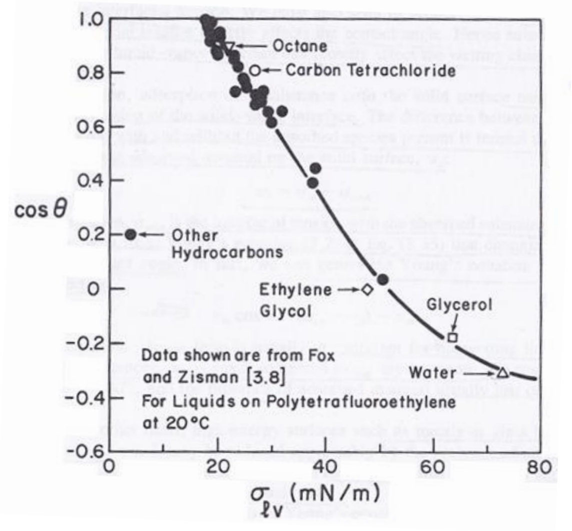

Figure 2.11: Observed contact angle on Teflon versus various liquid-vapour surface tension (Carey, 1992)

The critical surface tension may be used to determine whether a liquid will spread on a certain surface. It can be said that solids may be divided into two categories, namely, high surface energy solids and low surface energy solids. Glass and metals have high-energy surfaces ranging from 500 mN/m and higher, whereas hydrocarbons, polymers and plastics generally have low-energy surfaces, ranging from 15 to 40 mN/m. Non-metallic liquids' interfacial tensions typically range between 15 and 17 mN/m. Thus it can be shown for these liquids that clean high-energy surfaces are almost always wettable, as the critical surface tension will be much larger than the liquid-gas interfacial tension. The above conclusion would imply that metal surfaces would almost always be fully wetted by liquids. This however is not the case as a contact angle of 20° is usually observed for water on metal surfaces. This is due to the surface not being free of imperfections nor being perfectly clean. The high surface energy of metals also allows contaminants to easily wet its surface. This can significantly affect the spreading and efficiency of the working fluid which is of importance in heat transfer equipment (Carey, 1992).

This effect where a solid or liquid tends to retain solid, liquid or gas molecules at the interface is generally known as *adsorption*. It has also been shown that the liquid-vapour surface tension directly affects the contact angle and therefore adsorption may affect the wetting characteristics of a liquid on a solid. In some cases Young's equation is modified to allow for adsorbed material. However, the derivation of Young's equation does not account for additional adsorbed material at the interface and the adsorbed layer is not necessarily spread uniformly, which questions the validity of the adaptation. Ultimately, the above discussion shows that the wetting characteristics of solid metal surfaces, with the presence of adsorbed materials, may deviate significantly from a perfectly clean surface. Therefore, exposure to substances or materials which may be adsorbed on the surfaces of systems which are sensitive to liquid wetting characteristics must be avoided if possible (Carey, 1992). The theory behind thin film spreading is given in Appendix F.1.4.

2.2.4.4. Contact Angle Hysteresis

With a three-phase interface the contact line might be in motion. In this case the contact angles measured are dynamic contact angles. Static contact angles refer to the angles measured after a situation or event occurred. If a droplet expands the contact angle is advancing, whereas if the droplet contracts the contact angle is receding. Typically advanced and receded contact angles indicate a static case, whereas advancing and receding contact angles indicate a dynamic situation. The maximum and minimum contact angles are always the advancing/advanced and receding/receded contact angles, respectively.

For a perfectly smooth, clean and contaminant free solid surface there would seem to be no reason why these two angles should differ. This, however, is not the case and generally there is some difference. The difference between the advancing (maximum) and receding (minimum) contact angle is known as contact angle hysteresis. It is generally accepted that contact angle hysteresis is the result of surface inhomogeneity, surface roughness and impurities on the surface. Both surface roughness and inhomogeneity usually result in a greater advancing contact angle than receding contact angle. The adsorption of contaminants onto the surface further contributes to the non-uniformity of the surface wetting characteristics, with a net effect comparable to surface inhomogeneity (Carey, 1992).

The behaviour of liquid droplets can be significantly altered due to contact angle hysteresis. Liquid droplets may be suspended on vertical or inclined walls. The difference between the advanced and receded contact angle can be of such a nature that the resulting Laplace pressures are able to resist gravity (Carey, 1992). Quere (2002) states that effect of surface roughness is not always simple and can have some interesting consequences and that a roughness length scale is of importance. As the surface roughness is increased, at a smaller and smaller scale, the contact angle hysteresis may increase and then suddenly vanish. For a hydrophobic surface, this effect is characterised in an amplification of hydrophobicity, if the surface is rough enough at a small enough scale. Similarly a hydrophilic surface can become more hydrophilic with surface roughness at smaller scales. This then leads to the underlying theory of super-hydrophobic and -hydrophilic surfaces. Examples of super-hydrophobic surfaces include *Nelumbo* (lotus) leaves, anti-drag swimming suits and many more. Much more detailed information on surface roughness and wetting can be read in Quere (2002).

2.3. Bubble Formation

The following sections focus on vapour bubble formation in liquids. A brief discussion on the various modes of nucleation, their causes, the implications thereof as well as water under tension will be discussed with the purpose to better understand bubble formation and possibly prevent unwanted bubble initiation sites.

2.3.1. *Nucleation Theory*

In the macroscopic study of fluids, the fluid properties are assumed to be well defined at each point in space. However, when dealing with nano-sized control volumes the fluid properties may vary due to random molecular motion. When considering phase stability, localised micro variations might lead to the onset of phase transitions. Carey (2008) explains how, for a physically realisable system to be stable, the mechanical stability criterion must be obeyed, as shown by

$$\left(\frac{\partial P}{\partial v}\right)_T < 0 \tag{2.19}$$

where P is the system pressure, v is the specific volume and T is the system temperature. This indicates that at a constant temperature, the system volume must decrease or increase when the system pressure is increased or decreased for the system phase to remain stable. It has been found experimentally that liquids can be superheated and vapours super cooled to well within their equilibrium states, without phase transition occurring. It is said that vapour which is super cooled below and liquid which is superheated above their equilibrium saturation temperature is in a non-equilibrium state or metastable state (Carey, 2008).

The van der Waal’s equation of state model

$$P = \frac{R_{GC}T}{v-b} - \frac{a}{v^2} \tag{2.20}$$

can be used as a crude way to predict such metastable behaviour. Where R_{GC} is the specific gas constant, T is temperature in K, P is pressure, v is specific volume and a and b are constants determined for various fluids. A so-called spinodal curve can be generated which is simply the locus points of

$$\left(\frac{\partial P}{\partial v}\right)_T = 0$$

The spinodal curve indicates when a metastable state has reached its *intrinsic* limit of stability or *spinodal* limit and phase transition is imminent (Carey, 2008).

Nucleation is the formation of vapour or small droplet embryos which ultimately grow into larger bubbles or droplets, respectively. Nucleation which occurs completely within a fluid is called homogeneous nucleation and is contrasted by heterogeneous nucleation which occurs at the interface of a metastable phase in contact with another phase, usually a solid. Both homogeneous and heterogeneous bubble nucleation is shown in Figure 2.12 (Carey, 2008).

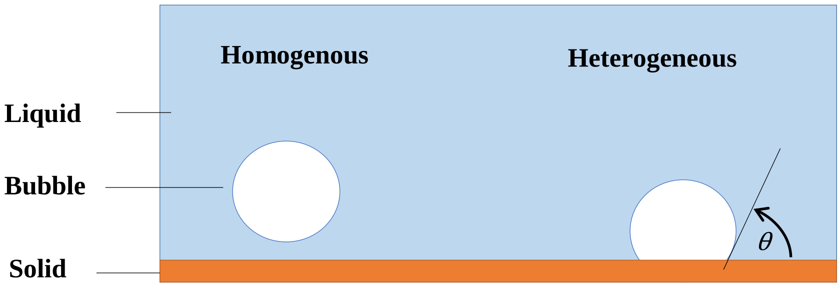

Figure 2.12: Homogenous and heterogeneous bubble nucleation

When considering a metastable liquid, molecular density variations may occur which exceed the spinodal limit. Localised regions where molecular density is close to that of saturated vapour may be generated, which gives rise to small embryo-bubbles of vapour within the liquid and is called hetero-phase fluctuations. Carey (2008) further shows that there exists a critical bubble radius for which bubbles of larger radii will spontaneously grow. Additionally, bubbles of smaller radii than the critical radius will reduce and collapse spontaneously.

Due to the fact that heat is usually added across a solid surface, nucleation tends to occur near the surface. This is mainly due to the liquid near the wall being superheated to above that of the bulk liquid. However, in very close proximity to the wall, attractive forces between the solid molecules and fluid molecules may affect homogeneous nucleation mechanisms. Near wall interactions for a highly wetted surface, on a nanometer scale, tend to increase the spinodal limit as the wall is reached. Thus near wall interactions may act to inhibit nucleation (Carey, 2008). Heterogeneous nucleation on smooth surfaces can be analysed similarly to homogeneous nucleation with the addition of contact angle. When compared to homogeneous nucleation, the temperature at which heterogeneous nucleation occurs was found to decrease for contact angles of $\theta > 70°$ and increase for $\theta < 65°$. Therefore the probability of heterogeneous boiling is greater on high contact angle surface interfaces (Carey, 2008).

Nucleation temperature values experimentally observed, however, are much lower than smooth wall nucleation models. The discrepancy in nucleation temperatures is attributed to the fact that real surfaces are indeed not entirely smooth. Narrow microscopic and macroscopic crevices, which are a result of natural imperfections or mechanical machining, are almost always present on real surfaces. Entrapped gas or vapour in such cavities might explain the experimental discrepancy from the smooth surface model. For a surface which is not completely wetted many cavities which contain entrapped gas may exist. Carey (2008) further states that a high contact angle at the interface will aid in vapour trapping. With a liquid at a metastable state, vaporisation may then tend to occur at the liquid gas interface in these cavities at lower temperatures than estimated previously. Contact angle hysteresis is a mechanism that aids the entrapment of vapour in crevices due to the difference between the advancing and receding contact angles (Carey, 2008). The density and number of active cavities which act as vaporisation initiators depend on the initial gas concentration in the liquid, the elapsed time from filling the system as well as any temperature and pressure variations or heat application. Dissolved gas in a liquid at room temperature and atmospheric pressure can be released from the solution to form bubbles in more cavities as the temperature rises or pressure decreases. A temperature increase or pressure decrease will both decrease the gas solubility and will provide more nuclei for vapour bubble formation. Cavities may be deactivated when heat is added to such a system and the non-condensable gas allowed to escape through the formation of bubbles and then allowed to cool down (Carey, 2008).

2.3.2. *Tensile Strength of Water*

The study of water under tension (or as often termed “negative pressures”) is of importance as it is often misunderstood or simply ignored in physical chemistry, yet it occurs frequently in nature. Water tension is believed to play a role in the ascent of sap in trees as well as water retention in porous materials (Mercury et al., 2012). Various studies have been conducted to understand water in this state. However, anomalous discrepancies in the value for the vaporisation threshold for water between various experimental methods as well as theoretical estimates have puzzled scientists (Davitt et al., 2010). Classical nucleation theory as well as the van der Waals equation of state estimate rather high tensile strengths of water ranging from 190 MPa to 230 MPa, respectively (Caupin et al., 2012; Peramaki, 2005).

Various independent research of water under tension has been conducted with the most well-known being that of Briggs, who in 1950 revisited Reynold’s centrifugal technique in Z-shaped tubes. Tensile strength estimates of water ranging from 3 to 28 MPa have been reported. Most consistently, however, ultimate water tensions near 30 MPa are obtained through various techniques including centrifugation, acoustic techniques and capillarity. The highest tensile strength that has thus far been reported is 140 MPa with liquid inside micro-cavities or quartz inclusions (Caupin et al., 2012). Liquid on such a scale is believed to be stabilised from the effect of impurities through near wall molecular interactions (Mercury et al., 2012). Most of the above techniques except quartz inclusions are believed to be susceptible to heterogeneous nucleation, with this being the reason for the lowered vaporisation threshold (Caupin et al., 2012).

Further research includes water under dynamic stress loading and was reported by Sedgewick and Trevena (1976) and Williams et al. (1999). In their study, Sedgewick and Trevena (1976), showed through experimentation that boiling or deionisation of water increased water's ability to withstand larger tensions. By boiling, most of the dissolved atmospheric air in the water was released. Similarly with deionization, it is suggested that charged particles make the onset of vaporisation more probable and therefore removing these ionic impurities reduce the possible nuclei cavities on which bubbles might grow (Sedgewick and Trevena, 1976). The studies that applied dynamic stress loading to the water all obtained much lower tensile strengths when compared to the static stressing cases. For example, a dynamic tensile strength of 1.4 MPa as compared to a static tensile strength of 30 MPa for boiled deionized water.

In summary, the above two sections on nucleation theory and water tensions indicate that to increase water's potential to sustain high tensions and remain in a metastable state, that the water must be free from impurities, that as much dissolved air must be removed as possible, that microscopic gas filled cavities must be prevented or deactivated, that a highly wetting surface be used and, finally, that the water be deionized.

2.4. Water Transport in Plants

In this section the uptake of water by the plant roots as well as the driving mechanisms thereof will be discussed. Much more background information on plant structures and cells can be found in Appendix F.2. The transport of organic substances, such as sugars, from plant leaves to the plant cells will not be discussed in such detail.

2.4.1. *Water and Mineral Transport*

Plant physiology is typically concerned with two main areas: above the ground, where shoots and leaves acquire sunlight and CO_2, and below the ground, where the root system acquires water and minerals (Campbell and Reece, 2008). Therefore, many aspects of plant structure and function are to expose a large surface area to the environment in order to enhance uptake of raw materials needed to sustain life (Starr et al., 1978). Xylem is a plant vascular tissue used to transport water and minerals (xylem sap) from a plant's roots up to its leaves. The most widely believed theory on water transport in plants is the *cohesion-tension-* or *transpiration pull*-theory. This is typically explained through the "T.A.C.T" mechanism which stands for transpiration, adhesion, cohesion and tension, respectively (House, 2010; Campbell and Reece, 2008).

Inside the plant, a continuous column of water stretches from the plant's roots up to its leaves. Within the leaf, water saturated mesophyll cells (discussed in Appendix F.2.3.) are exposed to large intercellular air spaces. The primary cell walls of the mesophyll cells contain very fine cellulose fibre like strands (or microfibrils) which provide strength and flexibility to the connective tissue. This together with the intercellular spacing acts as a very fine capillary network. Initially, a thin film of liquid water rests between cells or on the microfibrils of the primary cell walls (Peramaki, 2005). As time passes, water from the cell walls start to evaporate (or transpire) and decreases the thin film layer. The air-water interface is then forced to retreat further between and into the cell walls which leads to a curved interface (meniscus). Due to an increase in the evaporation rate as well as the surface tension of water, the interface curvature results in a local pressure drop that can generate a vacuum or even tensions. In large trees, this tension pulls water from surrounding cells and airspaces toward the interface. Ultimately water from the xylem is pulled toward the surrounding cells and airspaces to replace the lost water. The tension extends from the leaf through the xylem to the root into the ground (Campbell and Reece, 2008; House, 2010). This process is depicted in Figure 2.13 as well as Figure 2.14.

The combination of transpiration and surface tension are able to explain how water tensions may be generated which are able to pull a vast volume of water extremely high. However, this assumes that a continuous column of water must exist throughout the vascular tissue. Here adhesion and cohesion comes into play. Adhesion refers to the attractive forces between the water molecules and the xylem channels. The xylem consists of cellulose, presenting a polar surface, which causes strong attractive forces to water molecules and helps to offset the downward force of gravity. Cohesion involves the attraction of neighbouring water molecules toward each other, where water is known for its relatively strong cohesive bonds (House, 2010). It is important to realise that adhesion and cohesion are a significant part of the surface tension phenomena, but in this case it also allows long columns of water to exist in the narrow xylem channels without breaking. Therefore these properties give water a rather high tensile strength able to withstand typical water tensions of 1.2 to 3.5 MPa, which may sometimes range as high as 17 MPa, in certain stem segments of various plant species (Peramaki, 2005).

In tall trees, the bulk flow of water flows passively from the soil to the roots due to the immense tensions generated. In smaller pants however, especially at night, the method through which water is absorbed from soil into the roots is by osmosis. This is the diffusion of water across a membrane from a higher water concentration to a lower water concentration. This results in a so called root pressure since a net pressure is induced which pushes water from the root xylem into the stem.

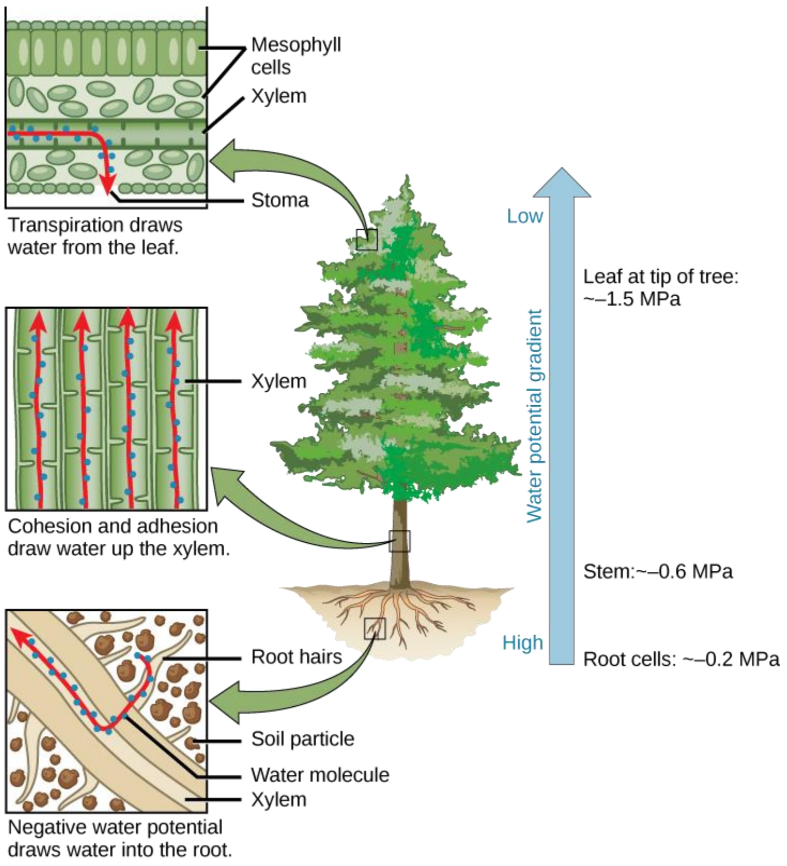

Figure 2.13: Schematic of water transport in plants (Brower, 2013)

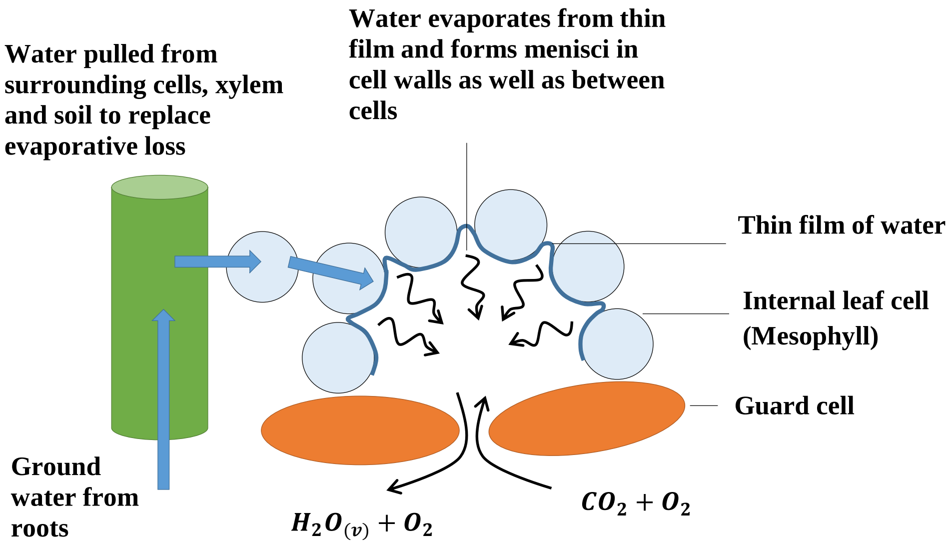

Figure 2.14: Transpiration-pull in leaf

At night, the root pressure may sometimes cause more water to enter the leaf than is transpired, which results in water droplets exuding from the tips of some plant leaves. This is commonly referred to as guttation. In most plants, root pressure is only able to push water a few meters at most and is a minor mechanism driving xylem sap transport. Many plants, especially taller trees, in fact do not generate root pressure at all. It has been found that root pressure is rather insignificant when compared to transpiration pull rates, even in plants that display guttation (Campbell and Reece, 2008).

2.4.2. *Limiting Factors*

The whole water transport process is remarkably energetically efficient, although it is limited in the sub atmospheric water pressure that it can generate. There are three limits of importance. Firstly, the capillary failure limit, which is simply the maximum pressure drop the meniscus can generate without giving way or the limit to the forces sustaining the meniscus (Sperry, 2011)

$$\Delta P_{cap} = \frac{2\sigma \cos\theta}{r_{cap}} \tag{2.21}$$

where r_{cap} is the effective capillary radius. If the pressure exceeds this limit, the tiny air bubbles stream into the tube by capillary failure. The second limit is the boiling point of water. Pure water at 20 °C has a saturated vapour pressure of 2.34 kPa (Çengel et al., 2011) and therefore at 1 atm results in a maximum pressure drop of 98.99 kPa. As mentioned in Section 2.3 boiling can either be homogenous or heterogeneous. If the heterogeneous boiling is suppressed, the liquid water phase can be sustained at pressures much lower than the boiling point. The water is then said to be in a super-heated or metastable state. When nucleation is supressed, experimental water tensions up to 30 MPa can be reached, as discussed in Section 2.3. A major cause of embolisms are “bubble nucleation” that initiated due to the presence of gas bubbles in the sap (Sperry, 2011). The Young-Laplace equation may be used to find the relative internal pressure of a bubble:

$$\Delta P_{bub} = \frac{2\sigma}{r_{bub}} \tag{2.22}$$

where, r_{bub} is the spherical radius of a bubble. If the pressure in the xylem is below the bubble pressure the gaseous phase will expand. The final parameter is the capillary tube strength or ability to withstand implosion. As demonstration, looking at the hoop stress of a simple cylinder:

$$\Delta P_t = \sigma_{stress}\left(\frac{t_w}{r_t}\right) \tag{2.23}$$

where, t_w is the tube wall thickness, r_t is the tube radius and σ_{stress} is the tensile stress in the member. It is possible to see that the thickness-to-radius ratio will limit the maximum vacuum pressures or tensions before implosion will occur. This equation is not valid in the analysis of real xylem conduits as much more structural complexities come into play. These three parameters then effectively constrain the maximum vacuum pressures or tensions achievable in plants (Sperry, 2011).

Plants, however, can operate at very large tensions ranging from 1.1 MPa (10 m tall tree at midday) to 5 MPa (desert plants) in leaf veins. Plants regularly face these great tensions in xylem conduits, especially at midday or peak environmental conditions. This problem is worsened by environmental conditions such as drought, freezing and salinity, increasing tensions even further. Therefore, gas leaks or cavitation which leads to embolisms are inevitable. Due to the vacuum or severe water tension conditions in the xylem, air or vapour is sucked into the transpiration stream and uncontrolled spreading can result in branch die-back or plant fatality. As embolisms occur, a cycle is initiated were conductivity decreases and so water tensions increase further resulting in more embolisms forming. Therefore coping with this problem is of utmost importance. Thus, multiple smaller conduits exist in parallel and series coupled by pits that act as "check valves" (Appendix F.2.2) to prevent the spreading of gas-filled or "*embolised*" conduits (Sperry, 2011).

Pit failure, however, is also inevitable and usually occurs through "air-seeding". The most common pits are membrane and torus-margo pit structures. Pit-membrane structures contain minute pores to prevent a critical bubble size from spreading to the neighbouring conduit. However, statistically due to the sheer number of pits, it is impossible that dysfunctional pit-membranes cannot exist. Thus the occasional pore is just too large and air is sucked into the functioning xylem channel. For the torus-margo pit structures, the centred torus is allowed to collapse inward on the pit pore when a pressure difference arises. If the pressure differences, however, are too large, the torus may slip and bubbles escape in to the flowing water stream (Choat et al., 2008).

2.4.3. *Nature of Hydraulic Needs and Plant Adaptations*

Plants require water for cell tissue and photosynthesis. The water is pulled upward to the photosynthetic regions by evaporative losses in the leaf through the stomatal openings. The exchange rate of water for carbon is very poor. The diffusivity and concentration difference of water vapour is much higher than that of carbon dioxide (Peramaki, 2005). This results in hundreds of H_2O molecules lost per CO_2 molecule, to the extent that 95% of water in the plant is evaporated under typical conditions. Plants however require carbon content for growth and the production of sugars etc. and must transpire water. The stomata are thus a crucial and essential mechanism in an effort to control the net water losses due to this process (Sperry, 2011). Transpiration may be affected by various aspects and for each plant the transpiration rate will differ as a response to its needs and environmental conditions. The major factors that affect transpiration are listed by BBC (2013) in Table 2.3.

Plants require water transport to take place effectively and efficiently. Due to the large cumulative leaf surface area for more carbon uptake from the air, to promote photosynthesis and growth, larger volumes of water are necessary. This presents a new set of problems as faster flows and plant height increases demand larger water tensions to allow such flows. This can cause water in the xylem to be in a metastable state which is susceptible to cavitation and ultimately embolisms. Many smaller conduits are thus preferred with pits to prevent the spreading of embolisms, as the loss of one smaller conduit does not have such a significant impact as opposed to losing a larger conduit. This in turn has negative consequences as narrower conduits and pits result in much more resistance to flow, where pits account for almost a 50% loss in hydraulic conductivity (Choat et al., 2008). Extremely large water tensions are then required to effectively pull water upward which increase the chances of embolisms. Plants have therefore adapted to use vessels and tracheids in the xylem tissues, as typical vessels are wider than tracheids and present less flow resistance. Pit variations also exist as to promote less flow resistance. It can be said that the plants' needs require plants to operate at near catastrophic failure (Tyree and Sperry, 1988). It would seem plants gamble in predicting environmental conditions and results in the growth of various adaptations and plant tissues as way to find some optimal balance.

Table 2.3: Factors that affect transpiration

Factor	Description	Explanation
Light	Higher frequency light increases transpiration	The stomata opens wider to allow more carbon dioxide into the leaf for photosynthesis
Temperature	Higher temperatures causes an increase in transpiration	Higher temperatures increase evaporation and diffusion
Wind	Faster wind speed increases transpiration	Evaporation of water from the leaf is increased due to forced flow over the leaf surface (forced convection)
Humidity	Higher humidity conditions slows down transpiration	As the air is nearing saturation the amount of evaporation must decrease

2.4.4. *Common Misconceptions*

Trees such as Giant Redwoods found in California can grow larger than 100 m, shown in Figure 2.15. The mechanisms through which water and essential nutrients are transported to the top of such giants have baffled humans for many centuries. Many still believe that some pumping mechanism from below or simply capillary action can explain how this is possible. The process however can be more closely compared to a complex wicking proses where the flow is driven by evaporation of water molecules into the environment. There are multiple lines of evidence which suggest that a living push or pumping mechanism from the bottom up to the leaves does not exist. Firstly, dissections show that there are no anatomical areas in stems or roots that could serve as a pump. Secondly, when physiologists placed a cut tree in picric acid as to destroy any living cells, the tree continued to transport water and implies that a living cellular stem pump is not involved. Thirdly, a root or stem pump would result in water gushing out of a decapitated stump. Finally, measured root pressures are in the range 0.2 to 0.3 MPa which is far below the typically required 1.2 to 3.5 MPa pressure difference required (Saupe, 2009).

Capillary action in xylem tubes are contested as sole water transport mechanism by considering various xylem conduit diameters. Typical tracheid and vessel diameters (discussed in Appendix F.2.2.) range between 5 to 80 μm and 15 to 500 μm, respectively. However rare, considering the narrowest conduit size of 5 μm will give the limiting height for a xylem tube. Employing the capillary height Equation 2.6 for this conduit diameter, a complete wetting surface and water at 20 °C:

$$z_i = \frac{2\sigma}{g\rho_l r_t}$$

$$h = \frac{2(73)10^3}{(9.81)(998)(5)} = 2.98\text{ m}$$

Trees however do indeed grow much taller than three meters, for instance 100 m Giant Redwoods. It is possible to see that xylem tissue is just too wide and cannot be the sole responsible mechanism for water transport in plants. It must also be noticed that capillary tubes on their own can only pull water upwards once and cannot continually move water upward (Saupe, 2009).

Figure 2.15: Giant Redwood (Nichols, 2014)

Transpiration pull would seem to provide a more plausible and complete mechanism through which water may be transported in plants. Several lines of evidence suggest sub atmospheric pressures in xylem conduits. Firstly, water in a cut stem snaps upward and water does not gush out. Secondly, measuring tree diameters showed that the stem diameter shrinks during the day as transpiration rates reach a maximum. This suggests that tensions do exist in tall trees as it pulls the xylem conduit walls inward. Thirdly, dye solutions are rapidly sucked into a tree trunk when punctured. Finally, bubble formation in xylem conduits can be heard when placing a sensitive microphone on the tree. This should only occur when the water is at lower pressures than the saturated vapour pressure (Saupe, 2009). Pressure bomb experiments, which measure the water potential of plant tissues, also indicate that water tensions do exist in leaf veins. Other evidence such as the Brigg's centrifugal Z-tube experiments and other experiments indicate water can indeed sustain a so-called metastable state at large tensions and has a rather high tensile strength (Sperry, 2011). The tensile strength of water has been the point on which many have challenged the validity of the transpiration-pull theory. One main contester is Canny's compensating pressure theory which implies that a compensating pressure, derived from an osmotic pressure gradient in living cells, can quickly refill embolised conduits. Many authors, such as Comstock (1999) as well as Stiller and Sperry (1999), have suggested evidence which disproves the compensating pressure theory. For further reading on current controversies regarding cohesion-tension theory see Tyree (1997).

2.4.5. ***Transport of Organic Substances in Plants***

Organic substances, such as sugars are transported in the phloem, as discussed in Appendix F.2.2. This process is called translocation. As energy producing cells are not always the same or near other energy requiring parts of the plant, an effective transport system or mechanism is required. The most common and widely believed theory which applies to most vascular plants is *pressure flow* or *mass flow* theory. The basis of the theory relies on a "source-to-sink" transport pattern. At the sugar source (mainly photosynthetic tissue) organic molecules are stored. Through active mechanisms, which rely on energy input, usually in the form of *Adenosine triphosphate* (ATP), and so-called transport proteins, organic molecules are moved into the phloem from the sugar source. Active transport occurs when cells directly use metabolic energy to drive solute flow against the passive transport direction. The most important transport proteins are the proton pumps, which use ATP to pump protons (H^+) out of the cell to generate a proton gradient resulting in a membrane potential. Together, this can drive the transport of solutes into or out of the phloem (Campbell and Reece, 2008). When the organic solutes enter the phloem, the water concentration drastically lowers and causes water from the xylem to diffuse to this area. A high pressure region is generated which drives the fluid within the phloem to a lower pressure region where the sugar sink resides. The solutes are then actively transported from the phloem into the sugar sink where it will be used. The pressure at the sugar sink region is relieved with a consequent loss of water returning to the xylem by osmosis. In the full leaf-to-root translocation cycle, the xylem is able to recycle the water from sink to source. Active transport, however, does not yield significant pressure drops that are able to achieve long distance transport. Usually the transport occurs from a source is to its nearest sink. Therefore, active transport mechanisms are only short distance solutions and cannot be used for long distance water and mineral transport (Starr et al., 1978; Campbell and Reece, 2008).

3. SURFACE TENSION DRIVEN WATER PUMPING

Construction of artificial trees to show the water pumping ability of plants have been attempted before by botanists such as Susman et al. (2009). Their ultimate goal is the modelling of plant water transport mechanisms and to physically simulate transpiring trees. The “artificial” tree produced in this project is geared at demonstrating the pumping potential of such a passive water pump rather than merely being a demonstrative tool for class lectures. Therefore the entire model is interpreted in a mechanical approach and the thermo-hydraulic modelling of the process is simplified as well as solved using engineering concepts. This section contains two previous attempts by botanists as well as the surface tension driven water pump design developed.

3.1. Previous Approaches and Artificial Trees

Section 2 laid the fundamental framework for the development of a surface tension driven water pump. It is clear that for a successful model to function correctly, an evaporative surface with minute pores is required which is able to hold a large column of water. A clear and definitive description of what materials will suite this purpose is difficult to find. Two main sources were considered both of whom independently constructed an artificial tree, namely Susman et al. (2009) and Martinez Vilalta et al. (2003).

Susman et al. (2009) presents an artificial tree for exhibitions as well as classroom experiments to demonstrate water transport in tall trees. For the evaporative surface, a 2-layer membrane with a pore density of 1.4 $(10)^9$ pores/cm^2 as well as an average pore size of 20 µm was used. The membrane used was a GoreTex^{TM} membrane and glued to a funnel. A transparent tube was used to connect the “leaf” to a beaker of water. The whole system was then filled with deaerated or boiled water and equipped with temperature-, relative humidity- and pressure sensors for continuous measurement. A ventilator was also used to allow forced flow over the artificial tree’s evaporative surface. A scale was used to measure the mass of the water filled beaker after certain time intervals. The laboratory trees built were claimed to work flawlessly for heights up to roughly 3 m. Their experiments show that increasing the height of such trees increases the likelihood of gas bubbles forming and ultimately causing an embolism. However, the severe pressure differences for higher trees of 6 to 8 m damaged the membranes allowing only 2 to 3 days before failure.

Martinez Vilalta et al. (2003) presents a transpiring tree model to illustrate cohesion-tension theory to students. It was built from products which are available from Merck Millipore, namely the filters as well as the filter holders. The evaporative surface used was a Ø47 mm hydrophilic 0.22 µm MF-Millipore™ membrane filter (properties in Appendix D.1.4.). PVC tubing ranging from 4 to 7.5 mm was used to transport water from a water source to the artificial "leaf". A scale was used to measure the mass of the water filled container over time. The initial filling was done with a peristaltic pump using boiled water (deaerated) to impede air bubble formation. The water was also deionized and acidified to a pH of 2 to inhibit micro-organism growth. The tree model height from the ground up was approximately 1.5 to 1.7 m and operation lasted a maximum of 4 days. Rates of almost 10 mg/min were observed on average with air temperatures and relative humidity of roughly 25 ˚C and 50%, respectively. System failure was primarily due to bubble formation in the tubes overnight, presumably due to temperature changes. It was found that covering the membrane filter surface or using even smaller pored membrane filters slowed evaporation rates and slightly increased the artificial tree's lifespan. The system longevity was found to be more dependent on tree height as smaller trees (1 m or less) operated up to 10 days at most whereas larger trees (up to 4 m) failed after a few hours. The addition of low levels of colorant seemed not to have a significant effect on evaporation rates nor longevity of the transpiring tree model.

3.2. Mechanical Approach

A biomimicry project allows one great freedom in research to try and find ways to mimic mechanisms found in nature. However, nature has had millions of years to evolve, adapt and develop desired mechanisms to increase the likelihood of survival. When considering plant water transport mechanisms it is clear from Section 2 that the internal leaf and water transporting tissues are rather complex. Due to limited technologies, time and cost the ultimate design of a surface tension driven water pump cannot incorporate all the features a plant would have. It is therefore important to identify the relevant and crucial elements for the design and simplify them, if need be, so that they are realisable.

The following section is a detailed description of the final design with the reasoning behind certain design choices. Figure 3.1 shows a simplified schematic drawing of the final "leaf" design. The final design shown here was developed by considering the designs presented by Susman et al. (2009) and Martinez Vilalta et al. (2003). However, the aforementioned artificial trees both contained large internal 'leaf' areas where bubble formation can easily occur and improvements on these designs were possible. Therefore, through rigorous testing the final design was ultimately developed and aiming at closer replicating the actual plant leaf. For manufacturing drawings of the design see Appendix B. The final "leaf" design consists of an upper and a lower disc which wedges the internal "leaf" material between them. The two discs were constructed from marine grade aluminium (Al-alloy 5083) which is a relatively light, strong and corrosion resistant material. To ensure a lightweight and tightly sealed design, the "leaf" was designed to be as thin as possible with 12 M8 bolts holding the discs together with a set of two O-rings to seal against any air that might slip through minute gaps along the outer edges.

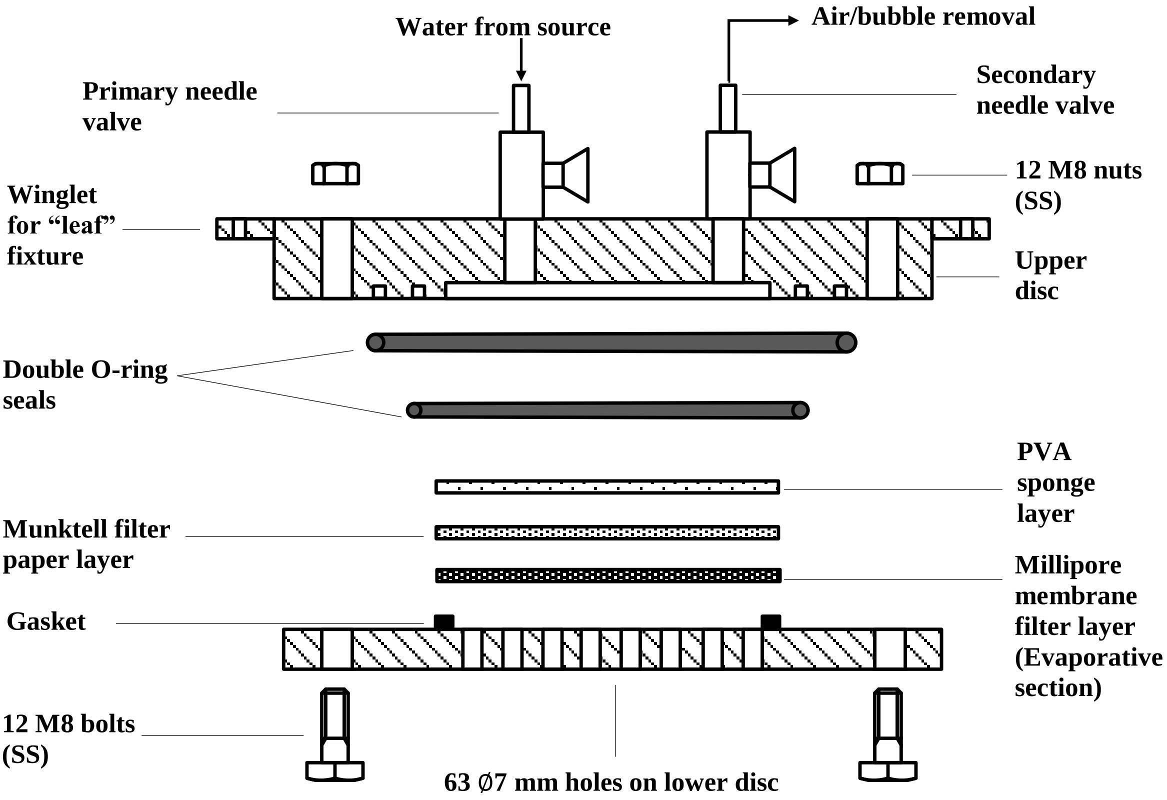

Figure 3.1: Schematic of the final "leaf" design

Furthermore, two brass needle valves fit into the upper plate to carefully regulate flow in and out of the "leaf". The upper disc contains a small chamber just large enough for the internal "leaf" material to rest. Susman et al. (2009) and Martinez Vilalta et al. (2003) both allowed large internal "leaf" space. However, a large internal "leaf" area was deemed unnecessary and would only increase the chances of embolisms occurring within the "leaf". The primary needle valve is used to shut off the water feed to the "leaf", while the secondary needle valve is used to remove trapped air in the "leaf" and alleviate the pressure build up during filling. Another feature on the upper disc is the winglets that allow the "leaf" to be easily bolted onto a frame or supporting structure. The lower disc features 63 Ø7 mm holes, at varying PCD's up to 80 mm, to allow water vapour to enter the surrounding air. In addition, the collection of smaller holes effectively protects the sensitive internal "leaf" material against external factors as well as pressure build up during filling. A similar design incorporated a single large lower opening of Ø80 mm with a fine copper mesh (40 linear openings per 25.4 mm) installed at the bottom to keep the “leaf” material safe and secure. Lastly, a gasket is placed on the lower disc to prevent air leaking past the internal “leaf” material.

As the evaporative section of the “leaf” is key in holding a large column of water, much experimentation was done to find a suitable material for this purpose. The material specifications for the following materials are given in Appendix D. Many materials were inspected such as Hartmann Hydrofilm (Appendix D.1.1), Munktell grade 393 Ø90 mm filter paper (quantative), 1 to 2 µm pores (Appendix D.1.2), and super absorbent sponges of high density polyvinyl alcohol (PVA) with estimated 200 µm effective pores (Appendix D.1.3).

All the materials tested where found to be unsuitable as either water dripped from the surface or air leaked into the system. The aforementioned materials, however, were still found useful as a means to closer replicate internal leaf tissues such as the leaf mesophyll cells as shown in Figure F.12. Membrane filters were identified to be a possible solution as their bubble pressure specification is rather large and this pressure is needed to ensure that the required capillary limit is obtained. To prevent unnecessary premature failure of the “leaf”, the internal “leaf” material consisted of three layers that contain progressively finer pores. The first layer, as seen in Figure 3.1, is a PVA sponge layer which is a hydrophilic material that helps to retain water in the “leaf”. Thereafter, the Munktell filter paper acts as the second layer and assists in this process. Additionally, the Munktell filter paper traps larger particles before reaching the final layer to prevent unnecessary clogging of the finer membrane filter. The final layer is the most important layer and is responsible for both the evaporation of water from the “leaf” as well as the strong surface tension forces that allow a column of water to be held up from the water source to the “leaf”. For the third and final layer, MF-Millipore™ membrane filters (0.22 µm) were used. Another Millipore membrane filter, Durapore® (0.22 µm) was also tested, but found not to work as effectively as the MF-Millipore™ membrane filters for this purpose. Figures 3.2 and 3.3 show SEM images taken for the PVA sponge, Munktell filter paper and Millipore membrane filters (Durapore® and MF-Millipore™).

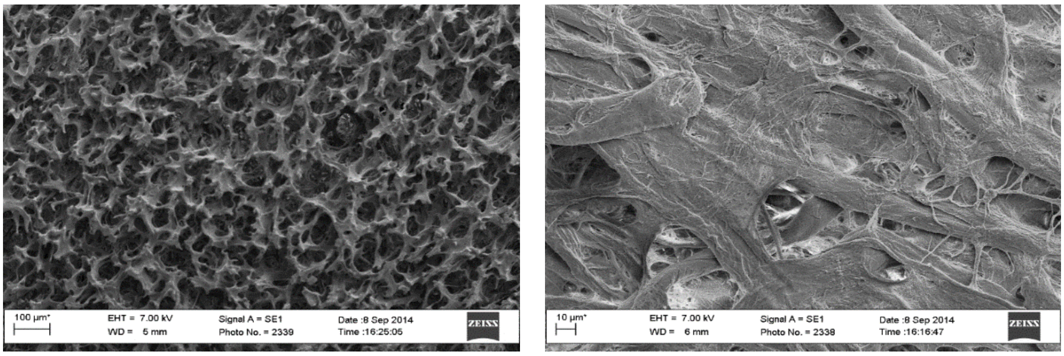

(a) PVA Sponge **(b) Munktell Filter paper**

Figure 3.2: SEM image of (a) PVA sponge 200x magnification and (b) Munktell filter paper 1000x magnification

Therefore the MF-Millipore™ membrane filters were used during all further testing. For detailed specifications of the Millipore membrane filters see Appendix D.1.4.

The membrane filters used are expensive relative to ordinary filter paper and are not stocked locally, nor where they available in larger sizes than Ø90 mm at the time of purchase. As result, the "leaf" size was much smaller than initially desired, however the compact shape in turn increased mobility and facilitated easy filling.

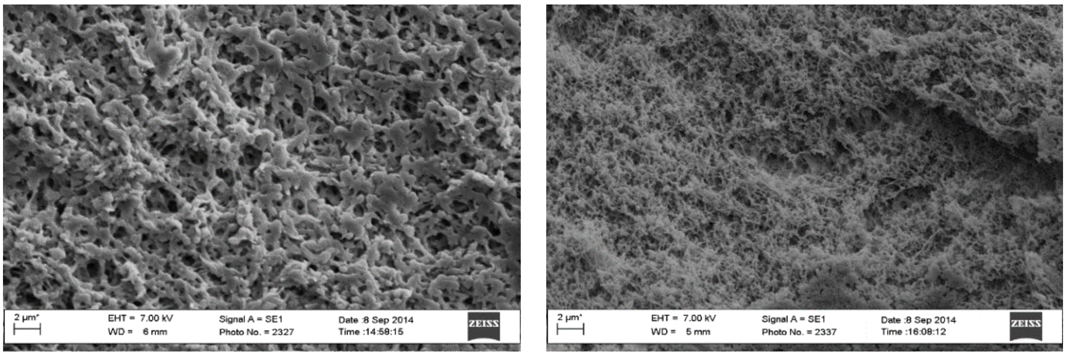

(a) Durapore® **(b) MF-Millipore™**

Figure 3.3: SEM image of Merck Millipore membrane filters (a) Durapore®7000x magnification and (b) MF-Millipore™ 7000x magnification

The operational flow diagrams for a single and multiple branch "leaf" systems are shown in Figure 3.4 and Figure 3.5, respectively.

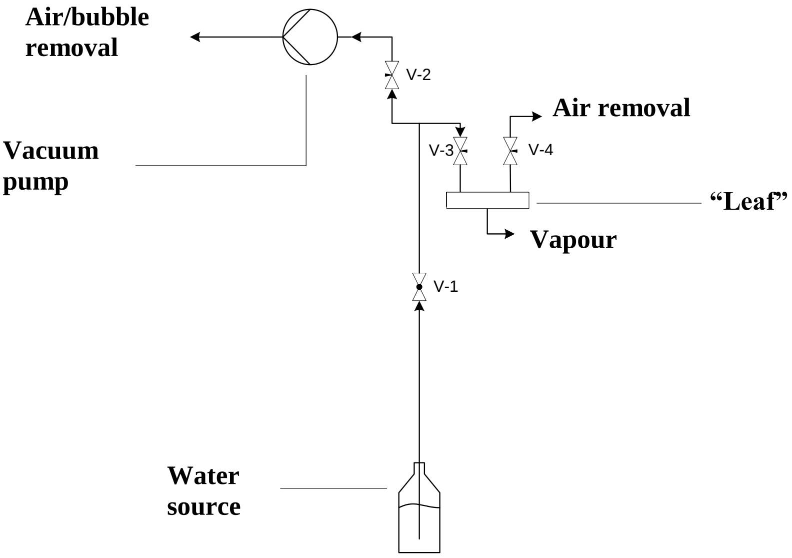

Figure 3.4: Flow diagram for a single "leaf" water pump system

The overall system is connected by 8 mm thick walled transparent PVC hose. Various options for the water transport channels were considered which include 3D printed micro tubes, powder metallurgy based tubes and bundles of smaller diameter thick walled PVC hoses. The primary reason for the use of thick walled hose above the any other options is its combination of flexibility, strength, simplicity and ease of use. The design incorporated brass gas line fittings to ensure a tightly sealed system between hose connections and prevent any possible air leakages into the system. Further, as shown in Figure 3.4, the basic system consists of a water source which is connected by a hose to the "leaf". A ball valve (V-1) shuts off flow to and from the water source, where an in-line needle valve (V-2) is used during the filling process for air removal and for bubble removal during operation. A vacuum pump was used to withdraw air and bubbles through the in-line needle valve. The in-line needle valve is placed at the highest point for bubble collection. As mentioned before, two needle valves were installed directly onto the "leaf". The primary needle valve (V-3) controls flow in and out of the "leaf" where the secondary needle valve (V-4) allows air and bubbles to escape during the filling process of the "leaf". Using the winglets, see Figure 3.1, the "leaf" can be secured to a frame at any desired height with the water source placed below the "leaf".

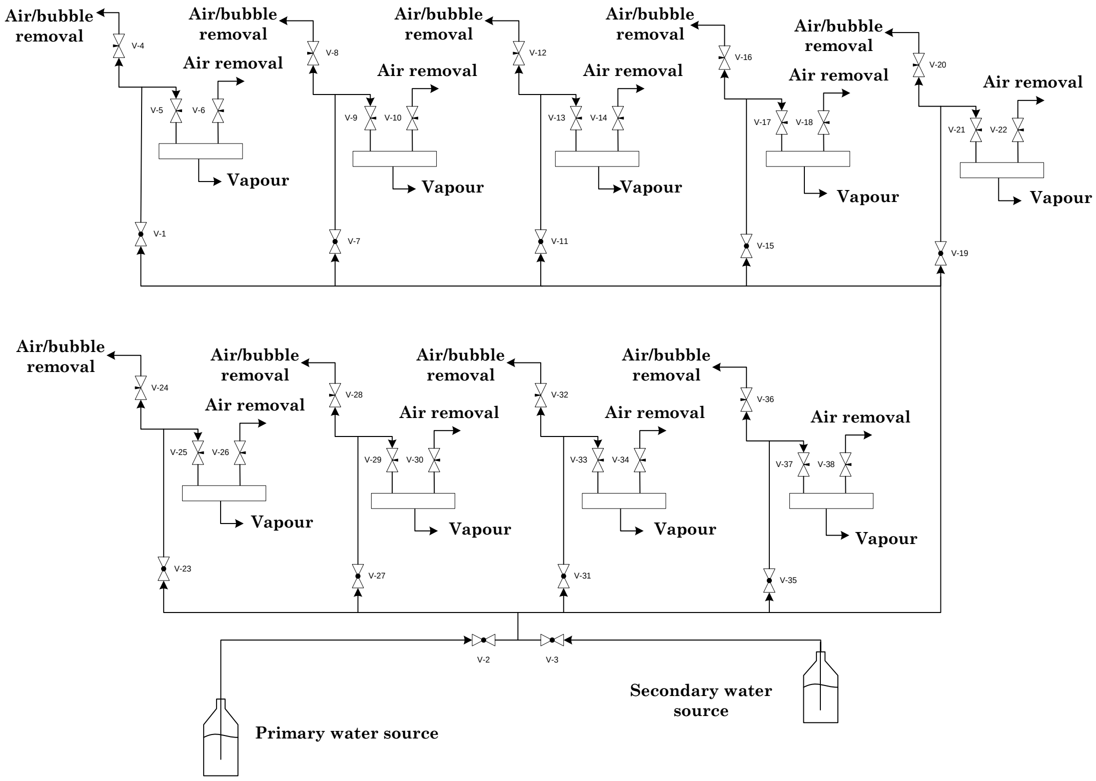

Figure 3.5: Process diagram of multiple branch system connected with a manifold

The multiple branch system, shown in Figure 3.5, consists of nine "leaves". The "leaves" where mounted onto an 8 mm thick Perspex plate, see Figure 3.17, and placed at a desired height. Each "leaf" is connected to a particular branch which has a similar setup to the single branch setup. All valves and fittings are once again brass gas line fittings to prevent any air leakages into the system. Each branch functions with a ball valve to shut off flow from the water source and an in-line needle valve to remove air and bubbles. The multiple branch system, however, includes a manifold which consists of a number of brass T-pieces which connects the various branches to a single water source. The layout for the "leaves" of the multiple branch system is shown in Figure 3.6.

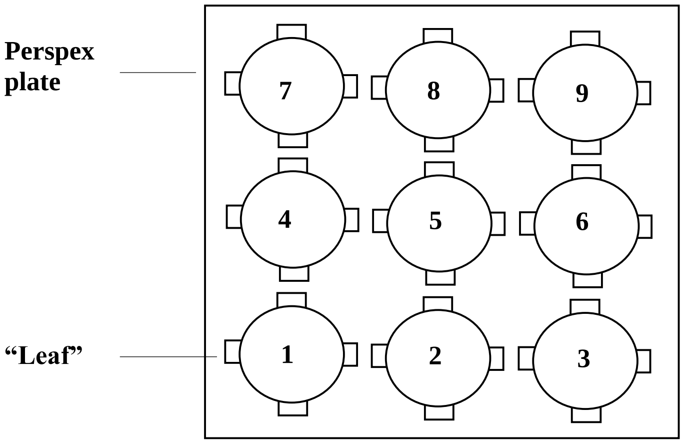

Figure 3.6: Multiple branch system "leaf" layout

In addition a primary and secondary water source is connected to the manifold and brass ball valves used to govern the flow from each. The primary source is placed lower than the "leaves" and is the water source used during system operation. When the system is initially filled or a branch requires refilling or even bubble extraction, the flow from the primary source is shut off and the valve to the higher secondary source opened. Water is then extracted from the secondary source to aid with filling or refilling. The multiple branch system was also adapted such that each "leaf" is able to draw water from a separate secondary water source. By removing the manifold from the system, failure of a certain branch was allowed to occur without corrupting the entire system.

3.3. Theoretical Thermo-Hydraulic Model

As mentioned earlier, the thermo-hydraulic modelling for the surface tension driven water pump is not intended to simulate or predict plant transpiration rates, but rather the potential water pumping capability of a man-made device subjected to a set of certain environmental conditions (temperature, relative humidity, pressure, wind speed). Figure 3.7 shows a flow resistance diagram for one of the branches. The resistance diagram shows that the flow of water from the water source to the "leaf" is directly related to the amount of water evaporated from the "leaf" if no other water extraction is taking place. This can be argued by simply considering the law of mass conservation. Therefore, evaporative mass transfer is the first step in analysis of a branch. The following concepts and equations on convective mas transfer are sourced from Çengel et al. (2011).

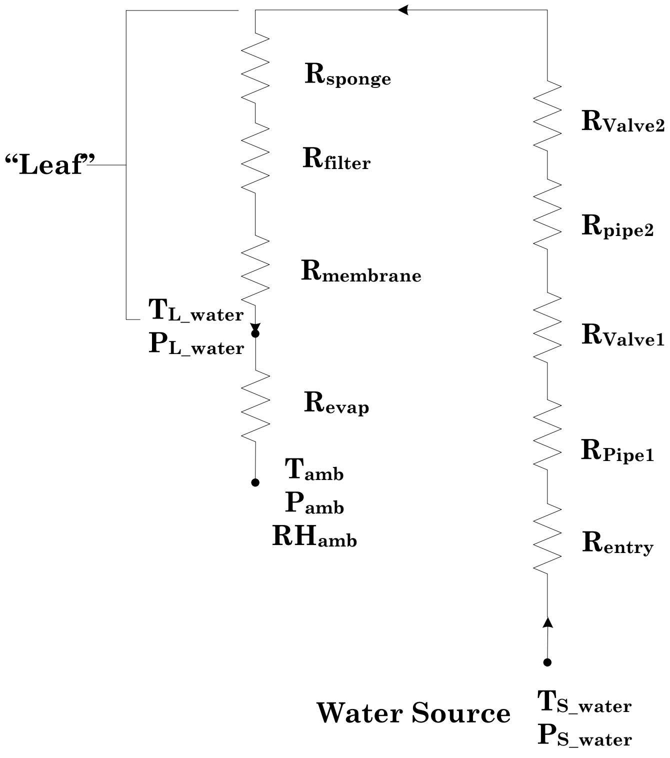

Figure 3.7: Single branch flow resistance diagram

Convective mass transfer is directly analogous to convective heat transfer and has the general form of

$$\dot{m}_v = h_{mass} A_s \left(\rho_{v,s} - \rho_{v,\infty}\right) \tag{3.1}$$

where $\dot{m}_v$ is the rate of evaporation, h_{mass} is the convective mass transfer coefficient, A_s is the surface area open to evaporation, $\rho_{v,s}$ is the density of the vapour near the evaporative surface and $\rho_{v,\infty}$ is the vapour density far away from the surface. The convective mass transfer coefficient is defined by

$$h_{mass} = \frac{\mathrm{Sh} D_{AB}}{L_c} \tag{3.2}$$

where Sh is the dimensionless Sherwood number, D_{AB} is the mass diffusivity of species A in B and L_c is a characteristic length. The Sherwood number relations can be found in Table 3.1 for various flows over a horizontal flat plate (Çengel et al., 2011). Three further dimensionless numbers are required to use the equations in Table 3.1, namely, the well-known Reynolds number, Re, Schimdt number, Sc, and Grashof number, Gr

$$\mathrm{Re} = \frac{v_f L_c}{\nu} \tag{3.3}$$

$$\mathrm{Sc} = \frac{\nu}{D_{AB}} \tag{3.4}$$

$$\mathrm{Gr} = \frac{g(\rho_\infty - \rho_s){L_c}^3}{\rho \nu^2} \tag{3.5}$$

Table 3.1: Sherwood number relations for flow over a horizontal flat plate

Convective surface	Region		Sherwood number	
	Forced Laminar	$\mathrm{Re} < 5(10)^5$ $\mathrm{Sc} > 0.5$	$\mathrm{Sh} = 0.664{\mathrm{Re}_L}^{0.5}\mathrm{Sc}^{1/3}$	(3.7)
	Forced Turbulent	$5(10)^5 < \mathrm{Re} < 10^7$ $\mathrm{Sc} > 0.5$	$\mathrm{Sh} = 0.037{\mathrm{Re}_L}^{0.8}\mathrm{Sc}^{1/3}$	(3.8)
Top surface	Natural	$10^4 < \mathrm{Gr\,Sc} < 10^7$ $\rho_s < \rho_\infty$	$\mathrm{Sh} = 0.54(\mathrm{Gr\,Sc})^{1/4}$	(3.9)
Top surface	Natural	$10^7 < \mathrm{Gr\,Sc} < 10^{11}$ $\rho_s < \rho_\infty$	$\mathrm{Sh} = 0.15(\mathrm{Gr\,Sc})^{1/3}$	(3.10)
Bottom surface	Natural	$10^5 < \mathrm{Gr\,Sc} < 10^{11}$ $\rho_s < \rho_\infty$	$\mathrm{Sh} = 0.27(\mathrm{Gr\,Sc})^{1/4}$	(3.11)

A relation for the mass diffusivity of water in air is also given by Çengel et al. (2011)

$$D_{AB} = D_{H20-air} = 1.87(10)^{-10}\frac{T^{2.072}}{P} \tag{3.6}$$

where T is in Kelvin and P in atmospheres. Thus if the surface and ambient air temperature, relative humidity, ambient pressure, evaporative surface area and air velocity is known, the above equations may be used to determine the mass transfer rate from the “leaf”.

The next step is to find the resistance due to fluid flow through the narrow tubes. Consider a Newtonian, incompressible fluid flowing through a pipe with a constant diameter which is much narrower than its length. It is assumed that the flow is steady as well as laminar. There are no external forces acting on the fluid except that of gravity. Consider a small control volume of water flowing in a pipe of radius r_s that is inclined at an angle α from the horizontal, as shown in Figure 3.8.

Firstly, the law of mass conservation is applied to the control volume

$$\frac{dm}{dt}_{CV} = \dot{m}_{x+\Delta x} - \dot{m}_x = 0$$

$$\dot{m}_x = \dot{m}_{x+\Delta x}$$

$$\dot{m}_x = \dot{m}_x + \frac{\partial \dot{m}_x}{\partial x}\Delta x$$

$$\frac{\partial \dot{m}_x}{\partial x} = 0$$

with

$$\dot{m}_x = \rho u_x r \Delta\phi \Delta r \tag{3.12}$$

$$\frac{\partial (u_x)}{\partial x} = 0 \tag{3.13}$$

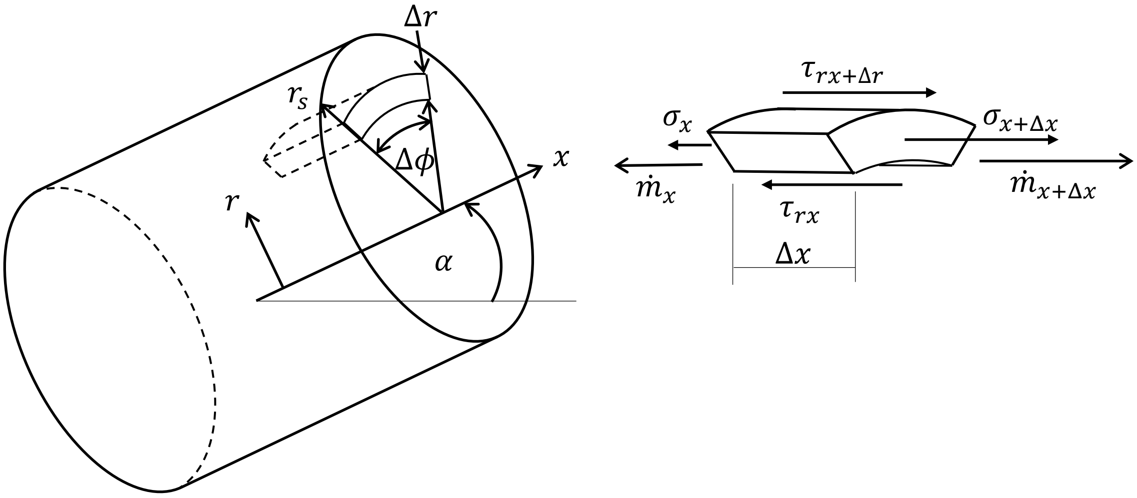

Figure 3.8: Pipe section with infinitesimal control volume

Secondly, the general conservation of momentum is applied to the control volume

$$\sum F_x = \frac{d(mu)_x}{dt}$$

$$\sum F_x = (\dot{m}u)_{x+\Delta x} - (\dot{m}u)_x$$

$$\begin{aligned} -mg\sin(\alpha) + (\sigma_{x+\Delta x} - \sigma_x) r\Delta\phi\Delta r \\ + (\tau_{rx+\Delta r} r - \tau_{rx} r)\Delta\phi\Delta x \end{aligned}$$

$$= (\dot{m}u)_{x+\Delta x} - (\dot{m}u)_x$$

$$\begin{aligned} -\rho g\sin(\alpha) r\Delta x\Delta\phi\Delta r + \sigma_x r\Delta\phi\Delta r + \frac{\partial \sigma_x}{\partial x} r\Delta x\Delta\phi\Delta r \\ - \sigma_x r\Delta\phi\Delta r \end{aligned}$$

$$
\begin{aligned}
&+\tau_{rx} r\Delta\phi\Delta x + \frac{\partial(\tau_{rx} r)}{\partial r}\Delta r\Delta\phi\Delta x - \tau_{rx} r\Delta\phi\Delta x \\
&= (\dot{m}u)_x + \frac{\partial(\dot{m}u)_x}{\partial x}\Delta x - (\dot{m}u)_x \\
&-\rho g\sin(\alpha) + \frac{\partial\sigma_x}{\partial x} + \frac{1}{r}\frac{\partial\tau_{rx} r}{\partial r} = \frac{1}{r\Delta r\Delta\phi}\frac{\partial(\dot{m}u)_x}{\partial x}
\end{aligned}
\tag{3.14}
$$

With the assumptions made for the flow analysis the normal and shear stress terms are simplified such that

$$
\begin{aligned}
&\sigma_x = -P \\
&\tau_{rx} = \mu\left(\frac{\partial u_x}{\partial r} + \frac{\partial u_r}{\partial x}\right) = \mu\left(\frac{\partial u_x}{\partial r}\right)
\end{aligned}
$$

Substituting this into Equation 3.14 yields

$$
-\rho g\sin(\alpha) - \frac{\partial P}{\partial x} + \frac{1}{r}\frac{\partial}{\partial r}\left(r\mu\frac{\partial u_x}{\partial r}\right) = \frac{1}{r\Delta r\Delta\phi}\frac{\partial(\dot{m}u)_x}{\partial x} \tag{3.15}
$$

Thereafter the change in momentum term from Equation 3.15 may be further simplified using the chain rule together with Equation 3.13, derived from the conservation of mass

$$
\begin{aligned}
&\frac{\partial(\dot{m}u)_x}{\partial x} = \frac{\partial(\rho u_x^2)}{\partial x} r\Delta r\Delta\phi \\
&\frac{\partial(\rho u_x^2)}{\partial x} = u_x\frac{\partial(\rho u_x)}{\partial x} + \rho u_x\frac{\partial(u_x)}{\partial x} \\
&\frac{\partial(\rho u_x^2)}{\partial x} = 0
\end{aligned}
\tag{3.16}
$$

By noting that the flow is only influenced by a pressure gradient in the x-direction and substituting the result from Equation 3.16, Equation 3.15 becomes

$$
-\rho g\sin(\alpha) - \frac{dP}{dx} + \frac{1}{r}\frac{\partial}{\partial r}\left(r\mu\frac{\partial u_x}{\partial r}\right) = 0 \tag{3.17}
$$

By assuming the following boundary conditions

$$
\begin{aligned}
&\frac{\partial u_x}{\partial r}(0) = 0 \\
&u_x(r_s) = 0
\end{aligned}
$$

Equation 3.17 may be solved

$$
\frac{\partial u_x}{\partial r} = \frac{1}{r\mu}\left(\frac{dP}{dx} + \rho g\sin(\alpha)\right)\int r\,\partial r
$$

$$\frac{\partial u_x}{\partial r} = \frac{1}{\mu}\left(\frac{dP}{dx} + \rho g \sin(\alpha)\right)\left(\frac{r}{2} + \frac{K_1}{r}\right)$$

$$u_x = \int \left(\frac{1}{\mu}\left(\frac{dP}{dx} + \rho g \sin(\alpha)\right)\left(r + \frac{K_1}{r}\right)\right)\partial r$$

where $K_1 \ = 0$ due to the first boundary condition

$$u_x = \frac{1}{2\mu}\left(\frac{dP}{dx} + \rho g \sin(\alpha)\right)\left(\frac{r^2}{2} + K_2\right)$$

where

$$K_2 = -\frac{{r_s}^2}{2}$$

and therefore

$$u_x = \frac{1}{4\mu}\left(\frac{dP}{dx} + \rho g \sin(\alpha)\right)(r^2 - r_s^2) \qquad (3.18)$$

The mean flow velocity is defined as

$$v_{avg} = \frac{1}{\rho A_c}\int_{A_c} \rho u_x \, dA_c$$

or in cylindrical coordinates for constant density

$$v_{avg} = \frac{2}{r_s^2}\int_0^{r_s} u_x r \, dr \qquad (3.19)$$

By substituting Equation 3.18 into 3.19

$$v_{avg} = \frac{2}{{r_s}^2}\int_0^{r_s} \frac{1}{4\mu}\left(\frac{dP}{dx} + \rho g \sin(\alpha)\right)(r^2 - r_s^2) r \, dr$$

$$v_{avg} = \frac{1}{2{r_s}^2\mu}\left(\frac{dP}{dx} + \rho g \sin(\alpha)\right)\int_0^{r_s} (r^3 - r_s^2 r)\, dr$$

$$v_{avg} = \frac{1}{2{r_s}^2\mu}\left(\frac{dP}{dx} + \rho g \sin(\alpha)\right)\left(\frac{r^4}{4} - \frac{r^2}{2} r_s^2\right)\Bigg| \binom{r_s}{0}$$

$$v_{avg} = \frac{-{r_s}^2}{8\mu}\left(\frac{dP}{dx} + \rho g \sin(\alpha)\right) \qquad (3.20)$$

This result may be used to manipulate Equation 3.18 to yield

$$u_x = 2v_{avg}r_s^2(r_s^2 - r^2) \tag{3.21}$$

Equation 3.21 is known as the Hagen-Poiseuille equation and describes laminar flow in pipes. Tree hydraulics are regularly analysed by employing the Hagen-Poiseuille equation as with Denny (2012). It can be shown from Equation 3.20 that the total pressure drop for a section of inclined pipe is related to the volumetric flow and the vertical height

$$\begin{aligned} \Delta P &= \frac{8\mu\Delta x\dot{V}}{\pi {r_s}^4} + \rho g \sin(\alpha)\Delta x \\ \Delta P &= \Delta P_{pipe} + \Delta P_{grav} \end{aligned} \tag{3.22}$$

Therefore the equivalent pipe section flow resistance without gravity can be written as

$$R_{pipe} = \frac{8\mu\Delta x}{\pi {r_s}^4} \tag{3.23}$$

where Δx is the pipe section length. The gravitational pressure loss term may be written as

$$\Delta P_{grav} = \rho g h \tag{3.24}$$

where h is the vertical height of the pipe section. Equation 3.24 agrees with hydrostatic pressure losses which increases linearly with fluid depth. The evaporative mass transfer at a specific time must be equal to the mass flow through system by law of mass conservation.

Due to the expected very slow volumetric flow rates through the system, Darcy's law for flow through porous materials is assumed to describe the flow through the porous "leaf" material. Sap flow models generally include Darcy's law as conducted by Peramaki (2005). Figure 3.9 shows a porous material. Consider a fluid passing through such a porous material at a very low flow rate. Equation 3.25, Darcy's law, may then be used to describe the pressure drop over the porous material which has a length of Δx and cross sectional area of A_c.

$$\Delta P = \frac{\mu\Delta x}{\kappa A_c}\dot{V} \tag{3.25}$$

where κ is the intrinsic permeability of the porous material, μ is the fluid dynamic viscosity and $\Delta P = P_1 - P_2$. The intrinsic permeability for the internal "leaf" was determined using the falling head test, as described in Appendix A.5. Therefore the effective leaf resistance is

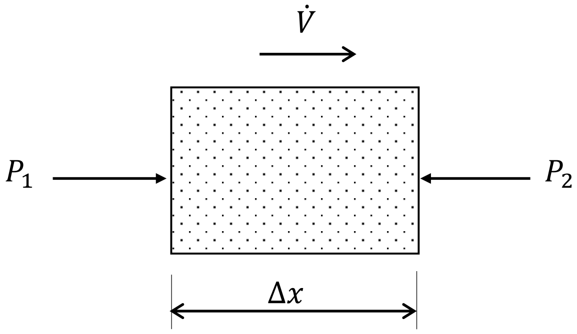

Figure 3.9: Darcy flow for a porous materials

$$R_{leaf} = \frac{\mu \Delta x}{\kappa A_c} \tag{3.26}$$

Finally, due to the assumption that the flow through each branch is very slow, it can be assumed that the pressure losses due to entry effects as well as various valves and fittings are negligible and therefore

$$R_{valve} \approx 0$$
$$R_{entry} \approx 0$$

The resistances may be summated in series to find the total branch resistance

$$\begin{aligned} R_{tot} &= R_{leaf} + R_{pipe} \\ R_{tot} &= \left(\frac{\mu \Delta x}{\kappa A_c}\right)_{leaf} + \left(\frac{8 \mu \Delta x}{\pi {r_s}^4}\right)_{pipe} \end{aligned} \tag{3.27}$$

The total pressure drop over the system can then be described as

$$\begin{aligned} \Delta P_{tot} &= R_{tot} \dot{V} + \Delta P_{grav} \\ \Delta P_{tot} &= R_{tot} \dot{V} + \rho g h \end{aligned} \tag{3.28}$$

where, h is the pumping head against gravity for the branch. The internal "leaf" pressure may then be estimated through this simplistic model to determine whether the capillary limit is exceeded, as a design constraint.

3.4. Experimental Setup and Procedure

To determine whether the constructed surface tension driven water pump is a potential passive water pump, various aspects such as water pumping ability, system longevity, potential pumping head as well as water collection capability were considered. Therefore, the experimentation was divided into various stages, namely, preliminary and small scale water pump testing, large scale water pump testing, capable water pumping head testing as well as water collection testing. This section focusses on the experiments conducted and gives a detailed description of the experimental setup as well as the necessary equipment and procedures.

3.4.1. *Materials*

The equipment and materials used for the various tests are listed below. For more material and equipment information as well as specifications see Appendix D.

- Nine "leaves" as discussed in Section 3.2.
- Two Cooler Master MegaFlow axial flow fans (Ø200 mm)
- One Cooler Master SickleFlow X axial flow fan (Ø120 mm).
- Nine 9 W heating pads (210 x 150 mm)
- 17 T-type (Copper-Constantan) thermocouples (temperature measurement). For a comprehensive description of the calibration procedure and results for the thermocouples used see Appendix E.
- One Agilent 34970A Data Acquisition Unit (acquire temperature data from the thermocouples)
- Three Huato S100-EX+ data loggers (monitor and log the relative humidity and ambient air temperature)
- One RS232 BTU-PSYCHROMETER AZ 8912 (measure the average air speed)
- Nine 250 mL, one 500 mL, two 2 L transparent bottles and one 10 L water canister (water sources)
- One de-aeration system which consists of:
    - One Stainless steel pressure cooker modified with a brass needle valve
    - One laboratory water ejector vacuum pump
- One Hailea HC-150A aquarium water chiller
- One BICISA 2500 water pump

3.4.2. *Preliminary and Small Scale Water Pump Testing*

The preliminary water pump testing focussed on finalising the surface tension driven pump design. Here, various concepts and materials were tested and the results evaluated to determine which concept designs would be more appropriate. The system setup for the preliminary and small scale water pump tests were as described in Section 3.2 for a single branch as shown in Figure 3.4. Installation of the internal "leaf" material was done carefully and sterile latex gloves were used to minimise the contamination of the rather sensitive membrane filters. The membrane filters where gently placed on the lower "leaf" disc followed by the Munktell filter paper and PVA sponge to complete the triple layered internal "leaf" material. Both the PVA sponge and Munktell filter paper were pre-wetted in a sterile container before installation. The “leaf” was closed and care taken to ensure that all seals and internal “leaf” materials were still in place.

In the preliminary stages normal tap water was used to fill each branch. Each branch was slowly filled to prevent unnecessary damage to the fragile membrane filters and to remove any air pockets from the “leaf” or piping system. All the valves were initially opened to allow water to easily fill the air filled tubes of each branch. The in-line needle valve was closed as soon as the entire tube was filled with water and void of all bubbles. The secondary needle valve, in the “leaf”, was only closed when all observable bubbles ceased to flow out of the “leaf”. The bottom end of each tube was carefully placed in a filled transparent 2 L water bottle which would serve as water source to each branch. Thereafter, each “leaf” was carefully mounted onto a separate frame which suspended each “leaf” roughly 1 m above the ground. The water source for each branch was placed below the specific “leaf” and the initial water level marked.

In the preliminary testing phase two lower disc designs were compared. One features a large Ø80 mm opening in the lower disc which is covered by a 40 grid copper mesh where the other design features 63 Ø7 mm laser cut holes, as shown in Figure 3.10.

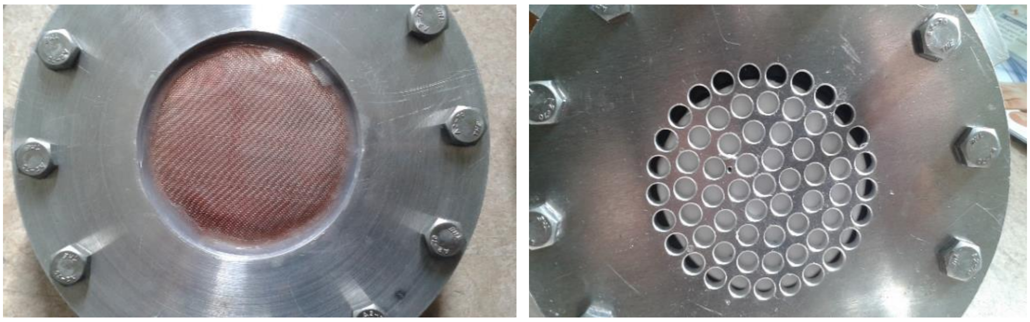

(a) Mesh **(b) Holes**

Figure 3.10: Lower “leaf” disc with (a) supporting mesh and (b) supporting holes

The ease of use as well as pumping performance of both designs were compared and the most promising design used in further testing. Thereafter, the two Millipore membrane filters, namely the Durapore® and MF-Millipore^{TM} membrane filters, were compared in a similar fashion using the “finalised” design. The small scale water pump testing evaluated the pumping performance of the surface tension driven pump for various environmental conditions. All tests were conducted with the MF-Millipore^{TM} membrane filters. The test setup during the preliminary and small scale water pump testing is shown in Figure 3.11 with the relative humidity sensors attached. A schematic diagram of the preliminary and small scale water pump testing can be seen in Figure 3.12.

To prevent water vapour escaping from the water source itself, the source opening was sealed. A single drop of food colouring was added to the water of the water source as a visual mechanism to observe the water movement up toward each “leaf”. The Huato data loggers were used to log the environmental conditions (ambient temperature and relative humidity) at 1 minute intervals during the tests. After the water level had dropped a sufficient amount, the new water level of each water source was marked and the time and date logged manually. Later, the Ø200 mm axial flow fans were used to increase evaporative rates. The average velocity of air flow over each “leaf” was measured using the psychrometer. By analysing the volumetric differences marked on the water source for each time interval, the average volumetric flow rates for each branch during a specific time interval was determined. Utilising the logged data, the measured flow rates were then compared to theoretically determined mass transfer rates.

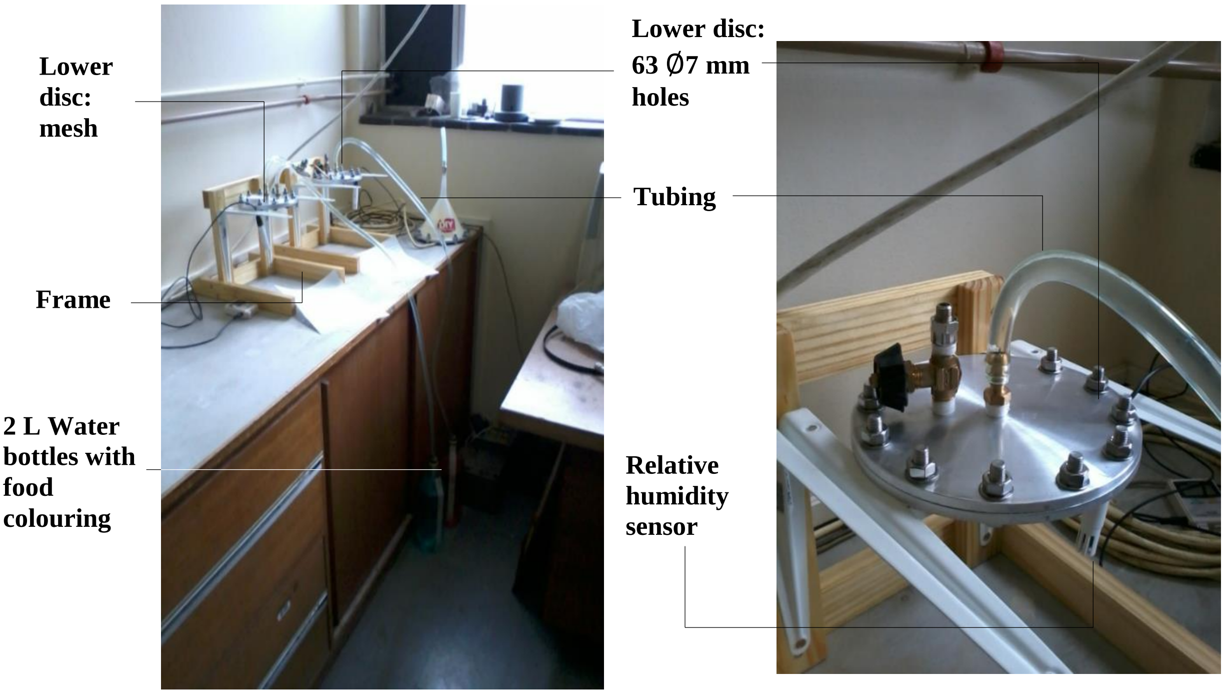

Figure 3.11: Comparative testing between the meshed and laser cut lower disc

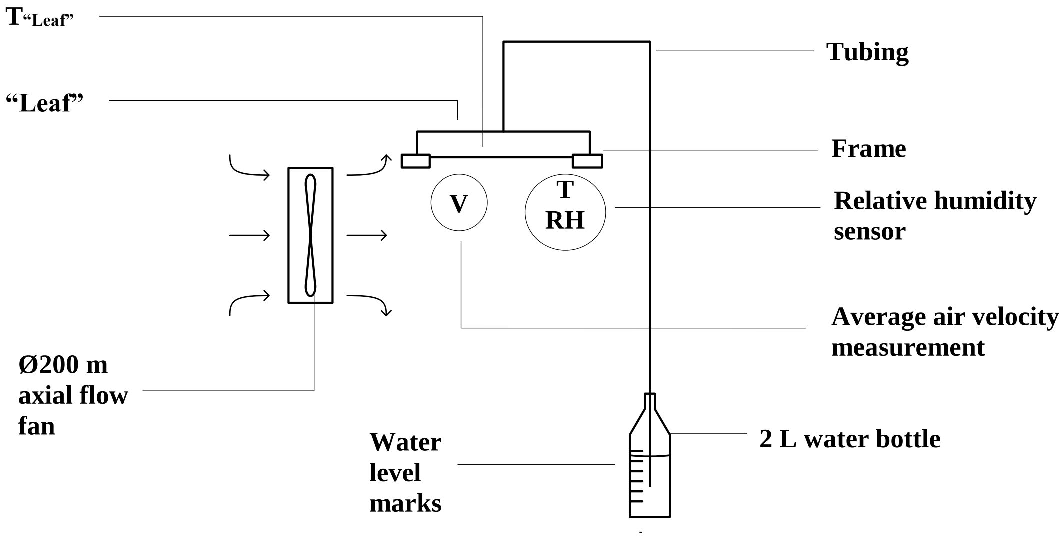

Figure 3.12: Schematic diagram of preliminary and small scale tests

3.4.3. *Large Scale Water Pump Testing*

The large scale water pump tests incorporated nine branches each attached to a separate “leaf”, as discussed in Section 3.2 with the multiple branch “leaf” layout as shown in Figure 3.6. The large scale tests were conducted to establish the behaviour and predictability of grouped “leaves”. The use of a manifold system which connects the various branches of the surface tension driven water pump was also considered. Additionally, the volumetric flow rates were monitored and compared to volumetric flow rates determined theoretically.

Two multiple branch system configurations were ultimately tested, as discussed in Section 3.2. First was the multiple branch system which is connected via a distribution manifold to a single primary water source, as schematically shown in Figure 3.5. Figure 3.13 shows an image taken of the manifold used to connect the multiple branch system. Thereafter, the multiple primary water source configuration was tested which did not incorporate the manifold. Installation of the internal “leaf” material during both tests was done precisely as in the small scale water pump testing. The initial filling of the multiple branches, however, did differ slightly from the single branch filling. Normal tap water was once again used to fill the entire system. A filled secondary water source (10 L water canister) was placed higher than the “leaves” while the primary water source(s) (2 L water bottle/250 mL water bottles) was below the leaves. The secondary water source was used to fill the branches whereas the primary water source(s) was used as feed water during system operation.

Figure 3.13: Manifold connection used in multiple branch system

The first step in the filling procedure for the multiple branch configuration connected by the distribution manifold was the initial closure of all valves except the valves between the primary and secondary source. The head difference between the secondary source and primary source was used to fill the tubes connecting the two sources. Thereafter the valve to the primary source was closed and the branch filling commenced. Each branch was filled independently by shutting off flow to the other branches. Further, all valves of the particular branch being filled were opened fully. The head difference between the secondary source and a particular "leaf" allowed water to gently fill the branch. The branch tubes were monitored and the in-line needle valve closed once the branch was completely voided of all observable bubbles. Care was taken to ensure no further bubbles or trapped air remained in each "leaf" by closing the secondary "leaf" needle valve only when all visible bubbles ceased to flow out of the "leaf". The falling water head used to fill the entire system was used as it placed minimal strain on the sensitive membrane filters. After filling the entire system, the feed water was switched from the secondary to the primary source. The multiple source system was filled similarly to the process discussed for the manifold connection. The exceptions were that each branch was independently filled by manually connecting it to the secondary source and thereafter reconnecting to a particular primary water source. The single and multiple water source(s) are shown in Figure 3.14 connected to their respective systems.

After the filling of each branch, the various "leaves" were fixed onto an 8 mm thick Perspex plate and placed roughly 1.5 m above the ground on a suspended wooden frame. Three Huato data loggers were used to log the ambient temperature and relative humidity in 5 minute intervals at three locations on the Perspex plate during the tests. Additionally, the Agilent data acquisition unit was used to log thermocouple measurements of internal "leaf" temperatures for certain "leaves". The thermocouples used were thin wire T-type thermocouples placed into Ø1.5 mm holes drilled into the lower “leaf” disc, such that the thermocouple is just in contact with the membrane filter layer, as shown in Figure 3.15.

(a) **(b)**

Figure 3.14: (a) Single water bottle (b) multiple water bottles in wooden holder

Figure 3.15: Placement of relative humidity sensors and thin wire thermocouples

Two Ø200 mm axial flow fans were mounted on the frame to increase evaporative rates for the large scale testing. A schematic for the overall test layout showing the various data collection locations, and thermocouple reference numbers is shown in Figure 3.16.

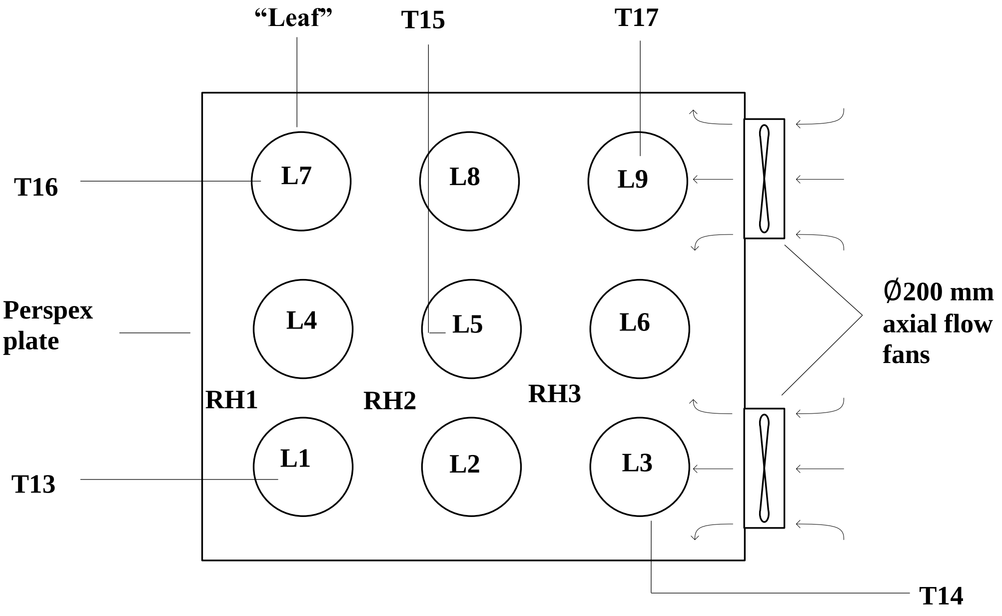

Figure 3.16: Schematic of large scale test layout with temperature and humidity measurement locations as well as fan placement

The "leaf" assembly is shown in Figure 3.17 mounted on the suspended wooden frame with all humidity sensors and fans attached.

Figure 3.17: "Leaf" assembly mounted on suspended wooden frame

The average velocity of the air flowing over each of the various "leaves" were measured using the air velocity reading of the psychrometer. A single drop of food colouring was added to the primary water source(s) to observe the water flow up each channel. The water level was marked on the primary water source(s) as well as after the water level had dropped a sufficient amount in order to estimate the average volumetric flow for the specific period. Utilising the logged “leaf” temperatures, ambient conditions and air velocity over each leaf, the theoretical volumetric flow rate for each period was determined and compared to the measured average volumetric flow rate for the respective time period.

Finally, 9 W heating pads were added to the top of each “leaf” and insulated on the top using insulation wool, as shown in Figure 3.18. The heat pads allowed the “leaves” to be gently heated above the ambient air temperature to speed up evaporative rates even further. The effect of warmer water in the “leaf” could then also be observed.

Figure 3.18: “Leaf” assembly with heat pads covered with insulation wool

3.4.4. *Capable Water Pumping Head Testing*

To determine the capable pumping head of the developed surface tension driven water pump, the water pump was tested at various heights. The tests were relatively simple and the system setup was as described for the small and large scale water pump testing. The bulk of the testing was done between 1 and 1.8 m of head height, however tests at heights between 5 and 10 m were also conducted to monitor the system response to varying high head pumping heights. Both small scale as well as large scale water pump tests were performed at 5 to 6 m of pumping head height while only small scale water pump testing, utilising a single branch, was done for heights greater than 6 m. The filling of branches and “leaf” installations was done precisely as described for the small scale and large scale water pumping tests.

As pumping heads near 10 m will cause the water in the tubes of the surface tension driven water pump to enter a metastable state, residual air and water vapour in the water filled tubes become an increasing problem. At lower head heights it was desired to establish the need for de-aerated water as this will greatly affect the potential use of the surface tension driven water pump. The rate at which the residual air content was released from the water and the ultimate failure times were recorded. De-aerated water was also used at lower head heights as a control. However, the use of deaerated and boiled distilled water was found to be necessary for all head heights of 5 m and up. A simple de-aerator was designed, consisting of a pressure cooker fitted with a needle valve and small laboratory water ejector vacuum pump connected by a thick walled Ø8 mm transparent tube. The distilled water was initially boiled and carefully poured into the vacuum chamber. The lid was secured firmly and the vacuum pump was then used to suck out excess air. Subsequently, the needle valve was shut after which the deaerated water was left to cool slightly. Thereafter, the deaerated water was used to fill the system. Figure 3.19 shows an image of the de-aeration system. The use of the de-aeration system allowed water to be deaerated. However, the system was not able to hold a vacuum for prolonged periods of time. It was observed that the combination of boiling and vacuuming the water decreased bubble formation in the tubes. This was especially evident at head heights of 5 m and up where bubble accumulation in the pipes would cause immediate failure when untreated water was used.

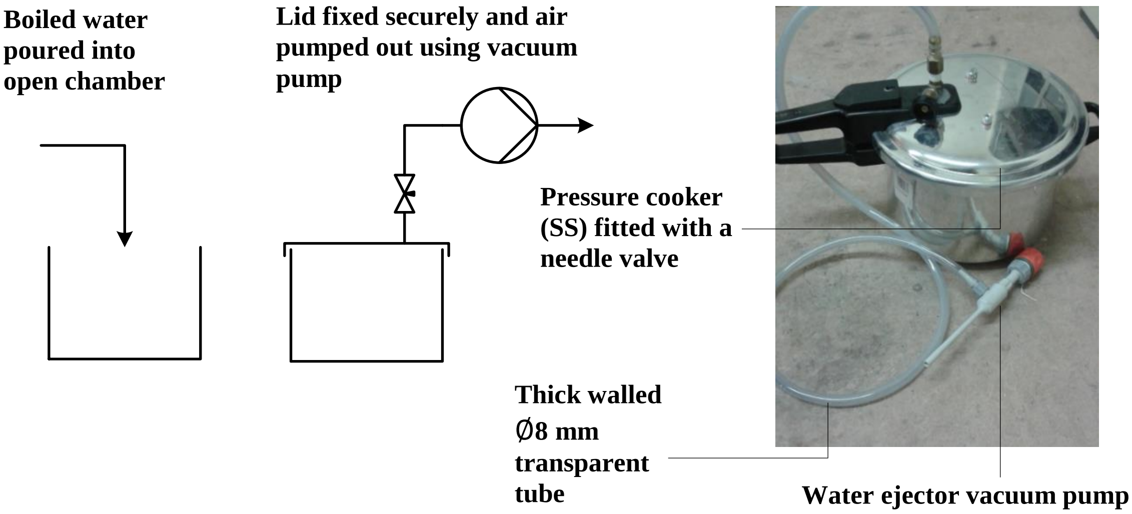

Figure 3.19: De-aerator system

The highest pumping head tests were performed at three locations at the University of Stellenbosch Mechanical and Mechatronic Engineering building, as shown in Figure 3.20. At each window the water source was slowly lowered to the ground. The system was monitored and a successful head height was defined as any height at which the system remained stable for at least 5 minutes. Thereafter the source was lifted back up and any released residual air bubbles removed from the system before attempting the same procedure from the next level. The tests were continued until system failure occurred due to an embolism forming. Only the ambient air temperature and relative humidity was monitored during the test using the Huato data loggers.

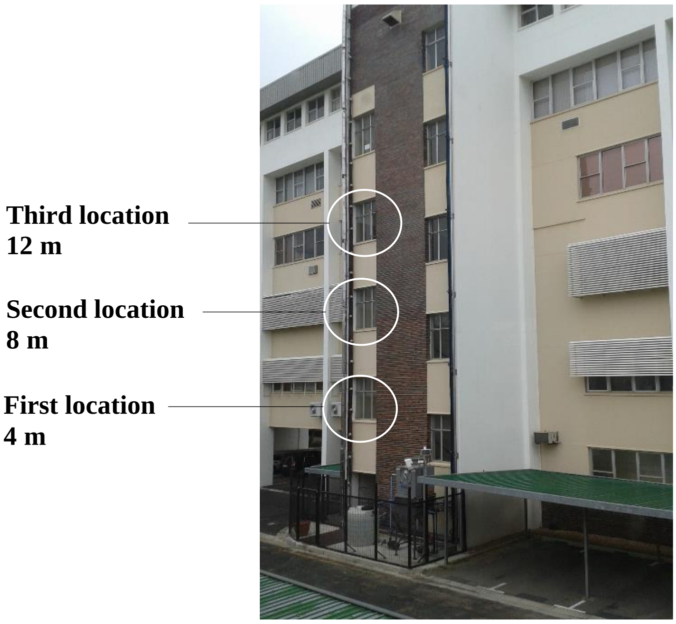

Figure 3.20: Highest pumping head test locations

3.4.5. *Water Collection Testing*

The final tests conducted were the collection of actual evaporated water from the "leaf". For this purpose, an environmentally closed control chamber was constructed to regulate the conditions at which the "leaf" would operate. Additionally, the chamber provided a means to collect the evaporated water and ultimately used to establish a mass balance between the water leaving the primary water source and the collected condensed water. An estimate for the extractable water content from such a system after a certain period was then determined. A schematic of the water collection test can be seen in Figure 3.21.

The filling as well as internal "leaf" material installation procedure for the test was done in a manner identical to the small scale water pump testing, however, deaerated tap water was used. The pumping head for the system during the tests was 1.8 m. For a single branch system the "leaf" was placed in a sealed enclosure to ensure that the water collected is a true reflection of the actual evaporated water from the "leaf". Three-eighths inch copper cooling coils were installed to remove excess moisture from the air with the Hailea water chiller and BISCA water pump together providing cooling water with a temperature ranging between 8 and 10 ºC. The condensate film formed on the cooling coils, coalesced, dripped off and channelled to a small water condensate collection container. To speed-up the evaporative process, a 9 W heat pad was placed on top of the "leaf" together with insulation wool. Additionally, the Ø120 mm axial flow fan was placed in the sealed chamber to induce forced flow over the "leaf" and promote air mixing within the chamber. An image of the actual water collection test setup is shown in Figure 3.22 with an additional heat pad and insulation wool covering the "leaf".

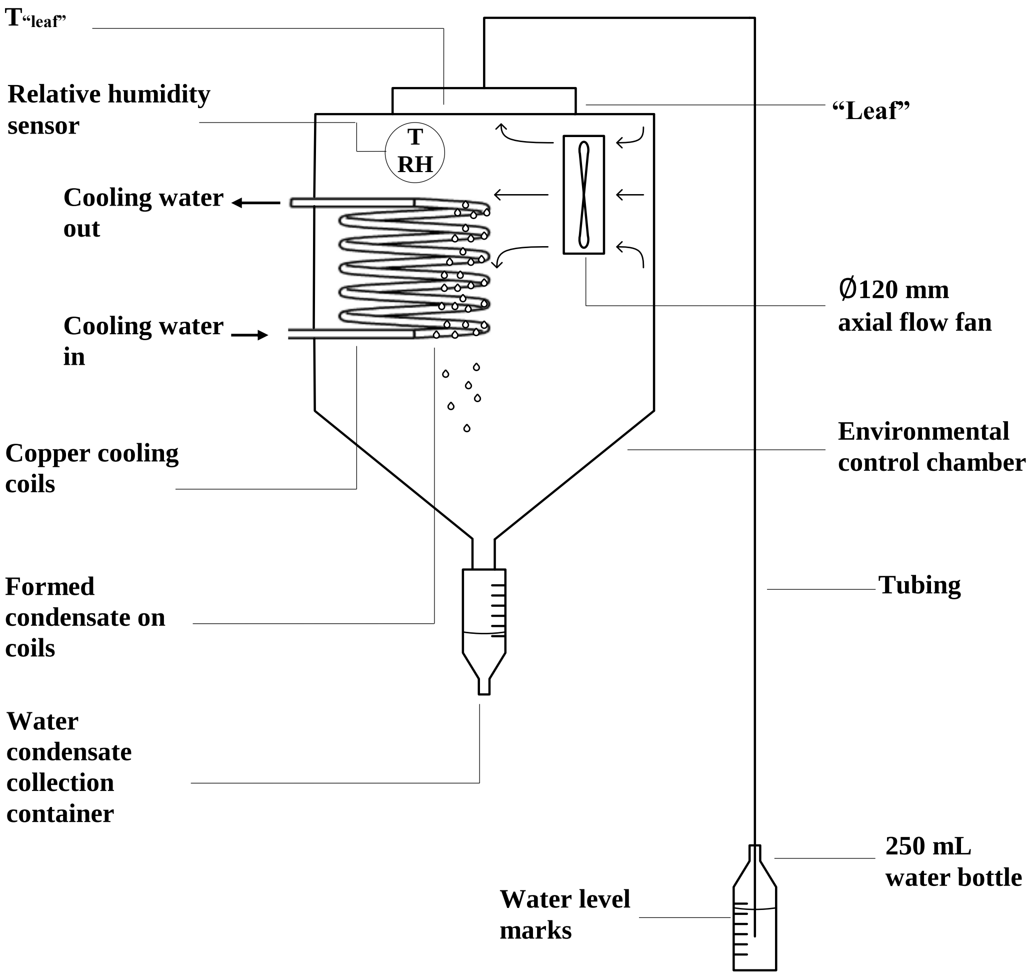

Figure 3.21: Schematic of water collection system for a single branch

After commencement of the test, the water level on both the water source (250 mL water bottle) and water condensate collection container (60 mL syringe) was marked. The total volume of water collected and pumped were compared afterwards to determine a water collection efficiency. For the tests conducted, the “leaf” temperatures were monitored with thin-wired thermocouples together with the Agilent data acquisition unit, while the ambient conditions (relative humidity and ambient air temperature) were monitored with the Huato data loggers.

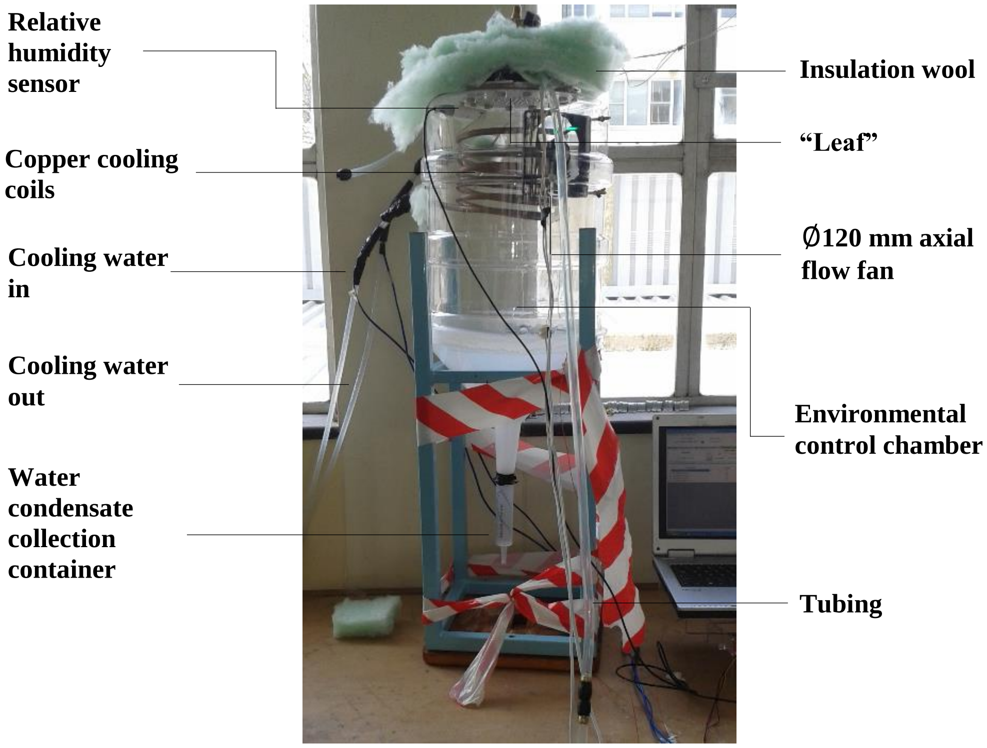

Figure 3.22: Water collection test for a single branch system

4. RESULTS

The experimental data captured was manipulated to report on the various aspects mentioned in Section 3.4. The performance of the single "leaf" configuration was analysed at various heights. The experimental measurements were then used to perform a multi-linear statistical regression to yield statistical predictions for the evaporative flux of water vapour from the "leaf, given the environmental conditions (v_{air}, T_{leaf}, T_{amb} and RH_{amb}). The experimental measurements were ultimately compared to theoretical mass transfer relations, given in Section 3.3, as well as the statistical predictions to determine whether such a "leaf" does exhibit predictable behaviour. Thereafter, the mechanical "leaf" performance was compared with actual tree transpiration rates, given in Appendix C. The experimental measurements for the multiple "leaf" configuration was also compared to theoretical mass transfer relations to determine whether the larger system displays somewhat predictable behaviour. A relation between the effective pumping head and pump failure time was also considered. Thereafter, the pumping head limits for the surface tension driven pump are explored. Finally, a summary of the water collection tests show the collection efficiency for the closed environmental control chamber designed

4.1. General Remarks

Some general remarks on the data analysis to follow. Firstly, for each measurement period the "leaf" and ambient conditions were fully logged in sufficient time steps. However, to estimate the predictability of a "leaf" for a set of design conditions and to yield a rough estimate of its performance and agreement with theory, the "leaf" and ambient conditions were then averaged over each measurement period. These averaged conditions were then used in the analysis. Secondly, the daily ambient pressure was monitored, but it was found not to vary significantly. With theoretical comparisons these minor adjustments in pressure did not yield significant evaporative flux differences and was therefore assumed to remain fairly constant. Thirdly, for the multi-linear regression analysis both linear and exponential fits were considered for both a natural and forced convection case. Only the best fit for the data acquired is shown in the following section. Finally, the evaporative area is generally required for the theoretical analysis of evaporative mass transfer, be it forced or natural convection. The Sherwood, Grashof, and Reynolds -numbers all require some geometric input. Here however, the data was manipulated such that the evaporative flux is given and a statistical relation for the evaporative flux developed. This is primarily due to the lack in variation of the evaporative area tested and would thus not contribute to the statistical analysis and understanding of the phenomena.

4.2. Comparison of Multi-linear Statistical Regression of Single "Leaf" Data and Theoretical Modelling

For the multi-linear statistical regression the experimental data was divided such that the forced convection and natural convection cases could be considered separately. A power series, Equation 4.1, was found to best fit the forced convection case whereas a linear series, Equation 4.2, was found to best fit the natural convection case.

$$\dot{V}''_{pred} = a_1 (v_{air})^{b_1} \left(T_{leaf}\right)^{c_1} (T_{amb})^{d_1} (RH_{amb})^{e_1} \tag{4.1}$$

$$\dot{V}''_{pred} = A_1 + B_1\left(T_{leaf}\right) + C_1(T_{amb}) + D_1(RH_{amb}) \tag{4.2}$$

Table 4.1 shows the statistical regression data for both the forced and natural convection cases. The table also contains a comparison of the theoretical predictions for both cases. Important factors such as the coefficient of determination, R^2, overall significance, standard deviation as well as residual error are included. A R^2 value close to 1.0 typically implies a good correlation between the measured data and assumed fit where a lower significance value usually implies a good correlation between the data and the regression variables. Without any further information whether the specified curve does fit the data, even a very low significant F-test value can merely indicate that the data gives evidence that for the best fitting curve generated, at least one of the multiple variables seem to correlate with the data. Further, to judge whether a curve does fit the data the residual error must be considered and should be independent of the predicted fit. At best a statistical regression is able to verify a manner of correlation between the regression variables and predicted fit to the data, but no serious claims of causation can be made.

Table 4.1: Statistical and theoretical comparison to measured evaporative flux data for both forced and natural convection cases

	Forced Convection		**Natural Convection**	
	Statistical	Theory	Statistical	Theory
R^2	0.9240	n/a	0.9916	n/a
Significance (F-test)	$4.6932(10)^{-16}$	n/a	$4.3228(10)^{-5}$	n/a
Standard deviation [mL/hr.m^2]	28.2519	29.8859	0.5782	2.7441
Average residual error [%]	8.4087	7.4073	2.9231	13.8446
Max residual error [%]	27.4963	30.2561	7.1024	25.4053
Min residual error [%]	0.5982	4.7879	0.8883	5.2023

A summary of the coefficients for the forced convection statistical evaporative flux predictions together with the upper and lower bounds (at a 95% confidence level) is shown in Table 4.2.

Table 4.2: Forced convection statistical fit coefficients and confidence bounds

Forced Convection		
Coefficients for Equation 4.1	a_1	2964328.76
	b_1	0.466865397
	c_1	4.099442737
	d_1	-2.858230010
	e_1	-3.098602429
95% Confidence upper bound constant	C_{upper}	1.261564150
95% Confidence lower bound constant	C_{lower}	0.792666787
95% Confidence upper bound		$C_{upper}\dot{V}"_{pred}$
95% Confidence lower bound		$C_{lower}\dot{V}"_{pred}$

Figure 4.1 (a) shows a comparative plot of the forced convection theoretically predicted evaporative flux against the actual measured evaporative flux for various pumping heights. Similarly, Figure 4.1 (b) shows the statically predicted evaporative flux against the same measured evaporative fluxes. These graphs also give an indication whether a statistical fit or theoretical prediction does indeed show a good correlation or fit. Table 4.3 contains the applicable range of values (applicability limits) for the input variables used in the statistical multiple regression analysis. The upper and lower limits as well as the average input variable

values are given. If input values close to the maximum or minimum applicability limits are chosen greater error might be expected for the evaporative flux predictions. If values exceeding the applicability limits are chosen, data will effectively be extrapolated and the degree of error for the evaporative flux predictions can be significant.

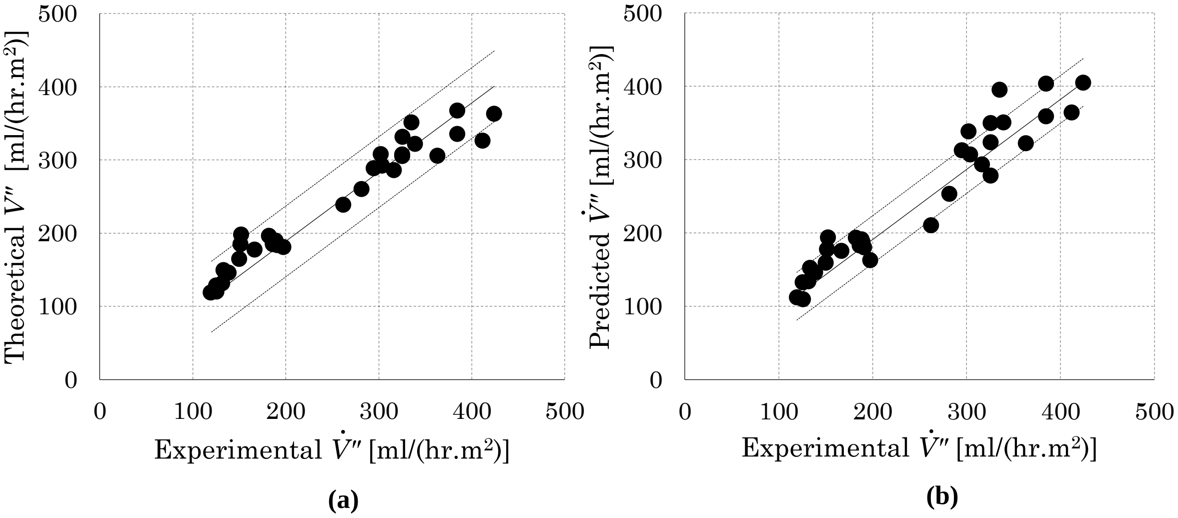

Figure 4.1: Forced convection evaporative flux (a) theoretically and (b) statistically predicted vs. experimental evaporative flux

Table 4.3: Applicable variable ranges for forced convection statistical evaporative flux prediction

	v_{air} [m/s]	T_{leaf}[°C]	T_{amb}[°C]	RH_{amb} [%]	$T_{leaf} - T_{amb}$ [°C]
Max	3.00	17.85	18.30	77.80	2.40
Average	2.22	15.21	14.64	73.59	0.57
Min	1.00	12.22	11.84	59.01	-0.65

A sensitivity analysis was done to determine which variables seem to yield the greatest effect on the predicted evaporative flux. The sensitivity analysis was done for both the statistical and theoretical formulations to give a measure of how well the statistical analysis compares to the theoretical predictions. This also indicates how well the statically predicted evaporative flux performs when data is extrapolated. For the sensitivity analysis, a base case at 0% is defined where the evaporative flux is predicted. Each variable is slightly increased/decreased up to ±30% of its base value. The predicted evaporative flux is then determined by adjusting a single variable at a time from the base case. Table 4.4 contain the values for the sensitivity variables used for the forced convection evaporative flux predictions.

Table 4.4: Percent increase of variables for forced convection statistical evaporative flux prediction sensitivity analysis

Percent increase from base condition	v_{air} [m/s]	T_{leaf} [°C]	T_{amb} [°C]	RH_{amb} [%]
30%	2.86	19.76	18.98	95.68
20%	2.64	18.24	17.52	88.32
10%	2.42	16.72	16.06	80.96
0%	2.20	15.20	14.60	73.60
-10%	1.98	13.68	13.14	66.24
-20%	1.76	12.16	11.68	58.88
-30%	1.54	10.64	10.22	51.52

Table 4.5 and Table 4.6 show the theoretically and statistically predicted forced convection evaporative fluxes, respectively, using the sensitivity variables listed in Table 4.4.

Table 4.5: Forced convection theoretical evaporative flux prediction for the given sensitivity variables

Percent increase from base condition	$\dot{V}''$ [mL/hr.m^2]			
	v_{air}	T_{leaf}	T_{amb}	RH_{amb}
30%	264.41	500.71	51.99	63.19
20%	254.04	403.27	117.35	119.49
10%	243.22	313.83	177.21	175.75
0%	231.90	231.90	231.90	231.90
-10%	220.00	157.01	281.73	287.86
-20%	207.42	88.70	327.00	343.48
-30%	194.02	26.57	367.96	398.53

Table 4.6: Forced convection statistical evaporative flux prediction for the given sensitivity variables

Percent increase from base condition	$\dot{V}''$ [mL/hr.m^2]			
	v_{air}	T_{leaf}	T_{amb}	RH_{amb}
30%	261.33	677.79	109.22	102.55
20%	251.74	488.19	137.30	131.41
10%	241.72	341.73	176.07	172.08
0%	231.20	231.20	231.20	231.20
-10%	220.10	150.11	312.45	320.46
-20%	208.33	92.62	437.50	461.61
-30%	195.74	53.58	640.82	698.19

The sensitivity analysis is graphically summarised in Figure 4.2 and Figure 4.3 from the forced convection evaporative fluxes calculated in Table 4.5 and Table 4.6. It includes a statistical upper- and lower bound. These figures effectively show a comparison between the statistical trend and the theoretical trend when a single sensitivity variable is systematically increased or decreased.

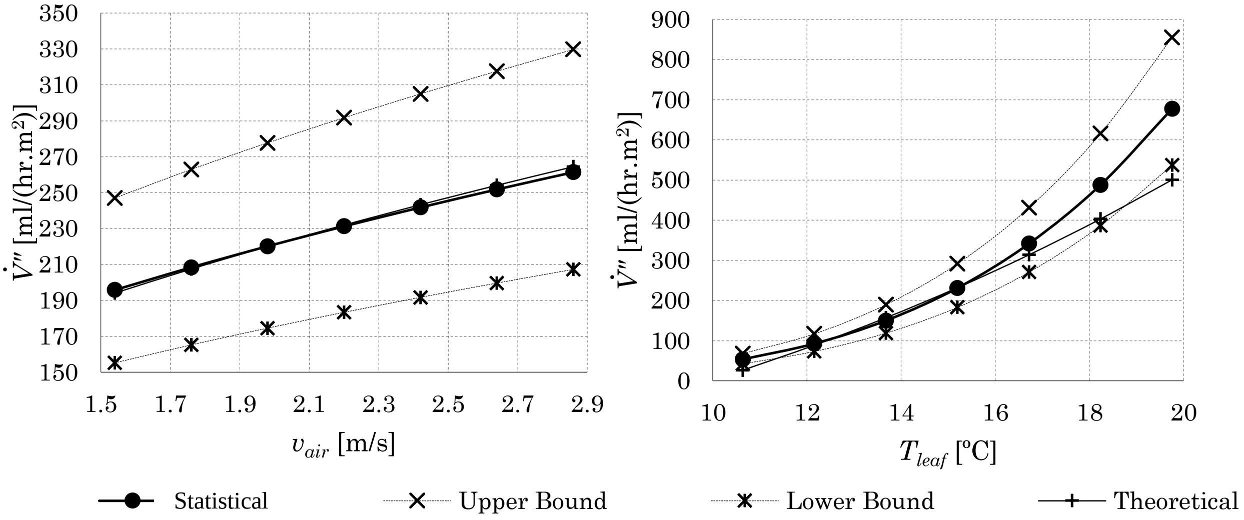

Figure 4.2: Graphical comparison of forced convection theoretical and statistical evaporative flux prediction for the given sensitivity variables ($\boldsymbol{v_{air}}$ and $\boldsymbol{T_{leaf}}$)

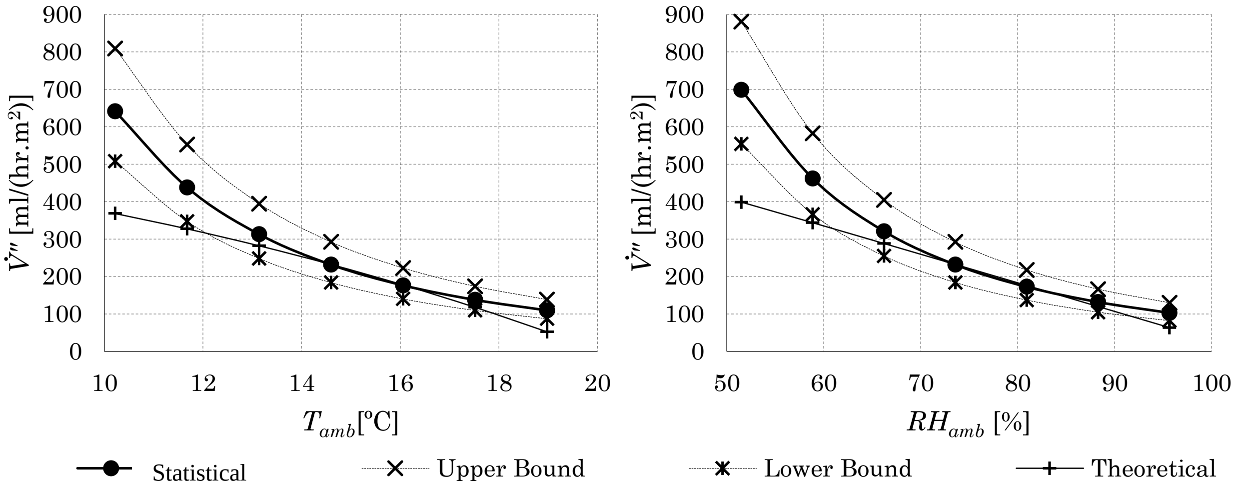

Figure 4.3: Graphical comparison of forced convection theoretical and statistical evaporative flux prediction for the given sensitivity variables ($\boldsymbol{T_{amb}}$ and $\boldsymbol{RH_{amb}}$)

The natural convection case was considered similarly to the forced convection case. The coefficients for the natural convection statistical evaporative flux predictions (Equation 4.2) are summarised in Table 4.7 with an error margin and upper- and lower bounds at a 95% confidence level.

Table 4.7: Natural convection statistical fit coefficients and confidence bounds

Natural Convection		
Coefficients for Equation 4.2	A_1	-52.65246903
	B_1	24.40855981
	C_1	-19.83196862
	D_1	0.070067307
95% Confidence error margin	EM	1.605329
95% Confidence upper and lower bound		$\dot{V}''_{pred} \pm EM$

Further Figure 4.4 (a) and (b) shows comparative plots of the natural convection theoretical- and statistical evaporative flux predictions, respectively, against the actual measured evaporative flux.

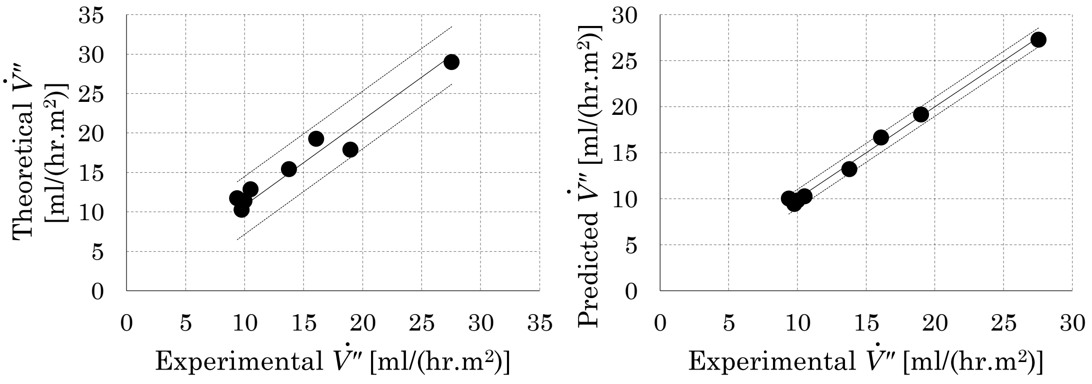

(a) **(b)**

Figure 4.4: Natural convection evaporative flux (a) theoretically and (b) statistically predicted vs. experimental evaporative flux

Table 4.8 contains the applicability ranges of the input variables for the natural convection statistical multiple regression analysis.

Table 4.8: Applicable variable ranges for statistical natural convection evaporative flux prediction

	T_{leaf} [°C]	T_{amb} [°C]	RH_{amb} [%]	$T_{leaf} - T_{amb}$ [°C]
Max	18.05	18.40	72.59	-0.62
Average	15.73	16.22	66.78	-0.48
Min	14.13	14.52	61.31	-0.35

The sensitivity analysis for the natural convection case is summarised in Table 4.9 with the sensitivity variables and their respective values.

Table 4.9: Percent increase of variables for natural convection statistical evaporative flux prediction sensitivity analysis

Percent increase from base condition	T_{leaf}	T_{amb}	RH_{amb}
30%	20.41	21.06	86.84
20%	18.84	19.44	80.16
10%	17.27	17.82	73.48
0%	15.70	16.20	66.80
-10%	14.13	14.58	60.12
-20%	12.56	12.96	53.44
-30%	10.99	11.34	46.76

All natural convection theoretical and statistical evaporative flux predictions for the corresponding sensitivity variables are found in Table 4.10 and Table 4.11, respectively.

Table 4.10: Natural convection theoretical evaporative flux prediction for the given sensitivity variables

Percent increase from base condition	$\dot{V}''$ [mL/hr.m^2]		
	T_{leaf}	T_{amb}	RH_{amb}
30%	76.73	-14.98	-11.30
20%	56.18	-31.84	-15.40
10%	37.34	-40.24	7.56
0%	15.30	15.30	15.30
-10%	-36.33	33.71	21.76
-20%	-25.69	45.90	28.23
-30%	-10.30	56.80	34.82

Table 4.11: Natural convection statistical evaporative flux prediction for the given sensitivity variables

Percent increase from base condition	$\dot{V}''$ [mL/hr.m^2]		
	T_{leaf}	T_{amb}	RH_{amb}
30%	128.93	-82.42	15.37
20%	90.61	-50.29	14.90
10%	52.29	-18.16	14.43
0%	13.96	13.96	13.96
-10%	-24.36	46.09	13.50
-20%	-62.68	78.22	13.03
-30%	-101.00	110.35	12.56

The predicted natural convection evaporative fluxes in Table 4.10 and Table 4.11 are summarised in Figure 4.5. General statistical upper- as well as lower bounds are included.

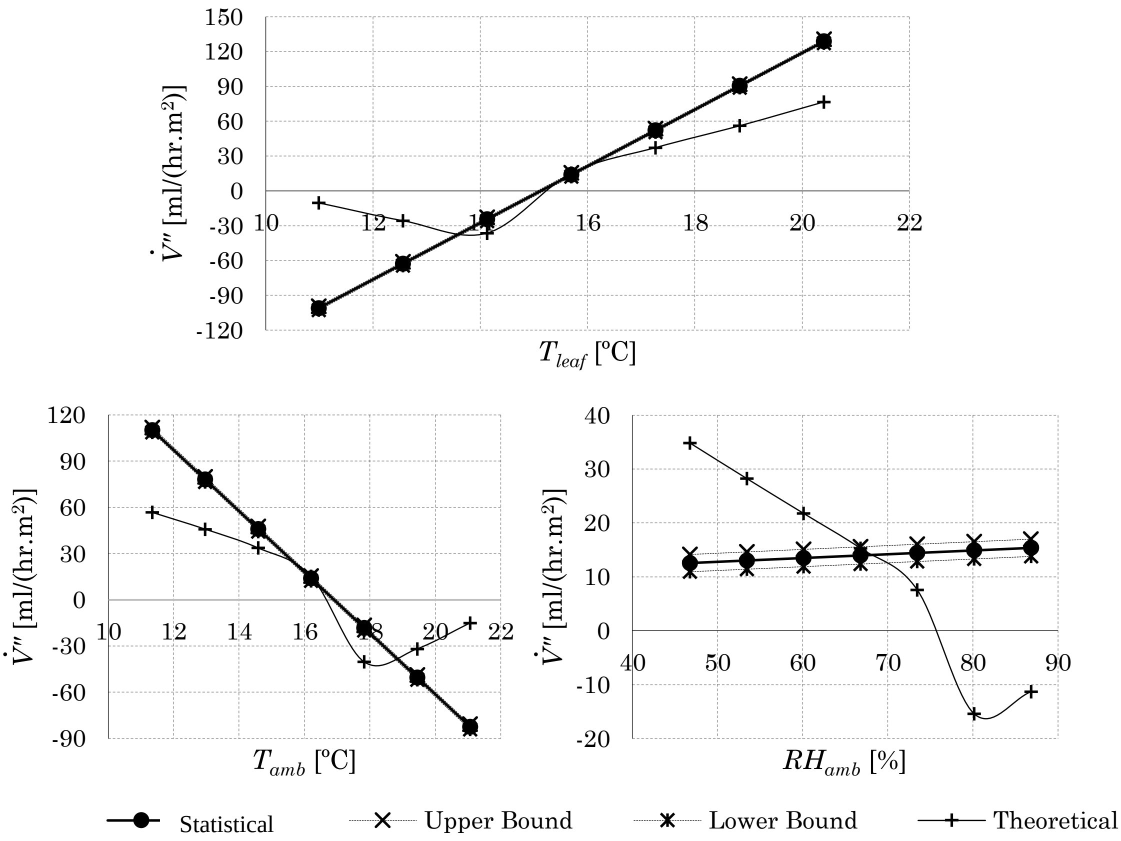

Figure 4.5: Graphical comparison of theoretical and statistical natural convection evaporative flux prediction for the given sensitivity variables (T_{leaf}, T_{amb} and RH_{amb})

4.3. Multiple "Leaf" Behaviour

The large scale pump tests revealed that a distribution manifold used to connect the various branches is rather risky. If a particular branch would fail the entire system was corrupted and ultimately ruined the measurement. Also, the performance and predictability of a particular "leaf" could not be determined. Therefore the only useful data for the large scale water pump testing was obtained when the distribution manifold was abandoned and each "leaf" operated using its own water source. The maximum, minimum and average error of the theoretical evaporative flux predictions for the large scale water pump tests are given in Table 4.12. Row 1 is the row of "leaves" closest to the axial flow fans (as shown in Figure 3.16) and include "leaves" numbered 3, 6 and 9. Row 2 is the next row, consisting of "leaves" numbered 2, 5 and 8 and the final row is row 3, which consists of "leaves" 1, 4 and 7.

Table 4.12: Summary of theoretical prediction error for each row of "leaves" during large scale tests

	Max error %	Average error %	Min error %
Row 1	16.12	7.09	3.96
Row 2	39.47	23.95	14.54
Row 3	63.65	43.00	15.57

4.4. Capable Water Pumping Head

During the various testing phases at different pumping heights, the ultimate time to failure for the single "leaf" was monitored. A distinction was made between a "leaf" failure and a bubble growth failure. Failure due to bubble growth in a pipe over time was found to be gradual. It was also characterised by a partially evacuated tube with the existence of a large bubble, balanced on both sides by contact angle hysteresis, in the pipe. A complete "leaf" failure usually occurred suddenly, even in the absence of pre-existing bubbles in the pipe. The tubes would be completely void of water and the water source overflowed. Figure 4.6 shows the complete "leaf" failure times for various tests at different pumping head heights.

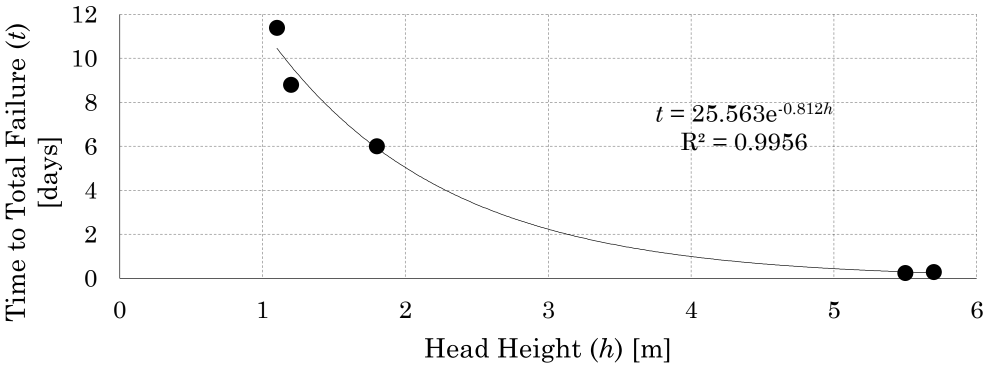

Figure 4.6: Time to total failure of "leaf" vs. pumping head height

The capable pumping head tests were conducted at various heights at the Mechanical Engineering faculty by lowering a water source out of a window at each floor, as explained in Section 3 (Figure 3.20). Table 4.13 contains the results for the capable water pumping head tests at various heights with some observations at each height. The theoretical head limit was determined to be 9.847 m above ground level for the test.

Table 4.13: Capable water pumping head test results

Location	Hold time [min]	Head height reached [m]	Observations
First	5	4.5	No bubbles
Second	5	8.4	Small bubble formation in tubing
Third	1	9.8	Large bubble formation with erratic pulsing bubbles in tubing
Third	Few seconds	10.1	Spontaneous rapid and random bubble formation in tubing. Complete failure

4.5. Water Collection

The average water collection rate of evaporated water from the “leaf” is shown in Table 4.14. Also included in the table is the percentage of water collected with respect to the volume of water pumped from the water source, in other words the water collection efficiency.

Table 4.14: Summary of water collection testing

	% Collected	$\dot{V}_{collected}$ [mL/hr]
Max	98.750	1.573
Average	98.339	1.571
Min	97.886	1.568

5. DISCUSSION OF RESULTS

The following section includes a detailed discussion of the results as well as observations made during the experimentation. Some recommendations for further testing and development are also discussed.

5.1. Validity and Possible Errors of Experimental Results

The statistical regression analysis and theoretical comparisons for the single “leaf” tests, shown in Table 4.1, indicate a rather good correlation between the various statistical fits and the actual measured data. The coefficient of determination, R^2, in both, forced- and natural convection cases are above 0.9 and the significance value (F-test) is well below 5%. This suggests that the regression, as given by Equations 4.1 and 4.2, does indeed describe the data range and that the regression variables are closely related to the data. The residual error for both the statistical and theoretical analysis is relatively low and an average error of approximately 10% is observed. Figure 4.1 and Figure 4.4 reaffirms the observation that the statistical and theoretical predictions for both forced- and natural convection over the single "leaf" correlate very well to the measured data.

During the experiments, the following aspects were identified to contribute to measurement error: Firstly, all environmental conditions and "leaf" temperatures logged were averaged over a certain period. Resultantly, a whole period that may contain many temperature and relative humidity variations could lose much critical information. This was especially evident on rainy days where intermittent light showers persisted, yet warmer weather emerged in between. Therefore, unpredictable weather patterns seemed to influence the averaging process. Smaller time intervals between measurements seemed to capture the data more accurately, with larger variations of the measured flow rate as opposed to larger time interval measurements. Secondly, the water level marks on the water source were used later to determine the volumetric change over a specific period. It was found that the thickness of the marker used together with the water meniscus in the container made it difficult to precisely judge the volumetric change. Water was removed from an initially refilled water source from one water level mark to the next using a fine syringe. The volume of water removed was recorded and also injected into a measuring flask to confirm the measurement. Thirdly, instrumental error played a small role as the thermocouples were found to be accurate and the fan speeds relatively constant. It was, however, found that the natural convection case was more sensitive to small errors. Finally, it was observed that large bubble formation in the branch tubing, as seen in Figure 5.1, displaced water back down to the water source and distorted measurements.

(a) **(b)**

Figure 5.1: (a) Primary and (b) final stages of large bubble formation

5.2. Sensitivity Analysis

The sensitivity analysis for the forced convection case, summarised in Figure 4.2 and Figure 4.3, showed that the much simpler statistical evaporative flux prediction is in good agreement with the theoretical predictions, when the input variables are within the applicable ranges for the statistical fit (shown in Table 4.3) and can be extrapolated with reasonable confidence. However, as soon as the input variables exceed the applicable range (given in Table 4.3) too much (especially $T_{leaf} - T_{amb}$) the error becomes significant. The forced evaporative flux is shown to be most sensitive to the variables T_{leaf}, T_{amb}, RH_{amb} and v_{air}, and in that order. This is expected as T_{leaf} and T_{amb} are major contributors to the ultimate water vapour density difference (see Equation 3.1) between the wetted surface and the ambient air. Furthermore, the relative humidity describes the water vapour content in the air, but is dependent on the ambient air temperature. Lastly, the air velocity is a significant factor which greatly accelerates the evaporation process. However, its effects are limited when the air becomes saturated with water vapour.

Figure 4.5 summarises the sensitivity analysis for the natural convection case. Here it is evident that the natural convection phenomena is more difficult to describe accurately. Within the variable applicability ranges for the statistical fit, shown in Table 4.8, there is a general agreement between the theoretical and simpler statistical evaporative flux predictions. However, once a slight extrapolation is made, the degree of error becomes significant. The small measurement population and lack of variation in relative humidity during experimentation allowed for a poor estimation on the effects of relative humidity. Furthermore, all the natural convection tests were conducted such that the “leaf” surface was in thermal equilibrium with its surroundings. Therefore, the heat loss due to natural mass convection was regained by natural heat convection as no heat was externally added or removed. T_{leaf} was found to be approximately 0.5 ºC cooler than T_{amb}, on average. In the sensitivity analysis $T_{leaf} - T_{amb}$ is much lower or even higher than captured in the experimental data. Hence the statistical regression poorly predicts cases of heat addition or removal. Additionally, the sensitivity analysis shows that T_{leaf} and T_{amb} are major factors which govern the evaporative flux during natural convection. Cases where T_{leaf} is low enough below T_{amb} the water vapour will return to the evaporative surface. Similarly, if the air is too humid, T_{leaf} need not be much lower than T_{amb} for the water vapour to return to the evaporative surface.

In general, the single “leaf” was able to pump water to various heights and its pumping ability found to be quite predictable. The simpler statistical formulations were found to be useful as a rough estimate for the expected evaporative flux from the single “leaf”. However, once the design specifications are outside the scope of the statistical analysis, theoretical predictions should rather be considered. The theoretical formulations present a more complicated alternative which should estimate the “leaf” performance with minimal error for a larger range of design specifications.

5.3. Comparison of Experimental Results with Actual Tree Transpiration Rates

The designed surface tension driven pump was compared to real tree transpiration rates captured in Appendix C. The data in Appendix C lacks any specific conditions under which the tree evaporative fluxes were measured and therefore it is difficult to compare the experimentally measured data with a particular tree. Consequently, the design performance was considered to be in reasonable agreement with various actual transpiring tree performances. Ultimately, the measured and predicted evaporative fluxes seem to be in reasonable agreement with actual tree evaporative fluxes. Evaporative flux rates, for forced flow over the "leaf" surface, ranging between 100 to 400 mL/hr.m^2 were measured and seem to correlate with data captured in Table C.2. Additionally, much lower evaporative flux rates for natural convection, ranging between 10 to 29 mL/hr.m^2, were measured and are seen to be comparable with tree evaporative fluxes in Table C.2 to C.4.

5.4. Multiple "Leaf Behaviour"

The behaviour of the multiple "leaf" design's pumping performance for various conditions was found to be less predictable than the single "leaf" pumping performance. As shown in Table 4.12, the "leaves" closest to the axial flow fans were rather predictable and displayed behaviour similar to the single "leaf" design. However, "leaves" further away from the axial flow fans exhibited a sharp increase in error with respect to the theoretical predictions. Reasons for this were mainly ascribed to unpredictable flow behaviour across the "leaf" surfaces. Inconsistent cross flows together with turbulent flows and localised near-stagnant regions with unaccounted specific humidity increases differs significantly from the assumed steady flow conditions. This implies that the multiple "leaf" design's pumping performance will not be accurately scaled from single "leaf" pumping estimations. Even for a single larger "leaf" area, care must be taken with interpretation of the predicted evaporative flux. This is found in real tree transpiration observations where the scaling from single leaf observations to canopy observations show disagreement (Meinzer, 1993). Meinzer (1993) attributes this phenomenon primarily to the formation of humid boundary layers and "unstirred" air layers.

The use of a distribution manifold for the multiple "leaf" design was found to present many complications in the operation of the surface tension driven water pump. It was observed that the removal of trapped air from the manifold presented much difficulty and that a single branch failure would result in entire system corruption.

5.5. Effect Water Pumping Head on Performance and Failure

Throughout the data analysis and testing it was observed that the theoretical evaporative flux predictions were consistently found to be independent of the pumping head. It is believed that for the same environmental conditions the mass transfer of water vapour from the "leaf" surface would be approximately the same for all the heights tested. For the consideration of further study of such a system at higher pumping heads it can however be argued that at much higher pumping heads than those tested here, that a slight reduction in the evaporative rate from the "leaf" surface may be observed. As the pumping head is increased the interfacial pressure for each pore in the evaporative material will increase. This will be accompanied by a receded meniscus with a sharp increase in the interfacial curvature. A receded meniscus will intuitively result in a slower evaporative rate as the evaporative surface is further removed from the environment. Additionally, the Kelvin equation (Equation 2.7) will predict a lowered vapour pressure due to the greater interfacial curvature, which will also result in a lowered evaporation rate (as discussed in Section 2.2.3). The extent of the reduction in evaporation rate from the "leaf" surface will greatly depend on the pumping head, the actual interface pore geometry, the effective number of pores and the material properties. However, considering Figure 3.3, the highly irregular surface presented by the membrane filter as well as the inconsistent pore paths through the membrane filter (number of closed/open cells), it is difficult to estimate the degree of reduction in evaporation from the "leaf" surface. For testing purposes it was therefore assumed that the entire membrane filter surface is fully wetted at all times.

The highest water pumping heads obtained for the developed surface tension driven water pump is summarised in Table 4.13. Here the longevity at a certain height was not tested, but simply the maximum pumping head. It was found that the de-aeration of water drastically reduced the residual air content in the water which hindered the formation of bubbles. However, at higher pumping heads (8 m and higher) it was evident that the water was not completely void of all residual air as the air bubbles yet again formed in the branch. At the theoretical maximum head (boiling point) it was observed that a single smaller bubble, near the highest point in the branch, gradually stretched into a single large bubble. Erratic bubble pulsing was observed near the maximum head as the bubble size rapidly decreased and increased. Just higher than the maximum head spontaneous bubble formation occurred at the highest branch locations. The branch was quickly evacuated and the water level dropped to roughly the theoretical maximum head height. When the pumping head was decreased below this height, the liquid once again filled the entire branch (with some residual bubbles remaining).

Although the membrane filter has a bubble pressure rating near 3.5 bar (as listed in Appendix D.1.4.) equivalent pumping heads of nearly 30 m were never reached. However, the reason for the premature failure is not regarded as a membrane failure due to the following evidence: The water column did not break immediately when heights just above 10 m were reached and therefore the water was in a metastable state as well as under slight tension. Furthermore, the water column did not recede all the way back to ground level which indicates that a vacuum is still present on the "leaf" side. If the membrane filter did fail it would no longer be able to generate a vacuum with a constant stream of tiny bubbles filling the branch until an embolism forms. It is, however, believed that the plastic tubing (which is hydrophobic) used for the branch material did not provide sufficient adhesion for the water to sustain any tension. Also, the residual air in the water as well as any surface cavities would provide nucleation sites for the onset of spontaneous phase change, as mentioned by Carey (2008).

5.6. Effect of Additional Heat on Performance and Failure

During the large scale water pump testing (see Section 3.4.3) heat pads were added to each “leaf”. With heat addition to the “leaf”, measured water temperatures were near 35 ºC. It was found that certain branches failed more rapidly than previously observed. The lowered surface tension attributed to higher operating temperatures is not believed to be the major contributor to the observed premature failure, as the surface tension is not reduced significantly (from 72.3 mN/m to approximately 70.6 mN/m). Also, the premature failure was is not attributed to membrane filter failure as the maximum operating conditions are listed (in Appendix D.1.4.) to be 75 ºC. It was, however, established that the de-aeration of water is crucial at higher operating temperatures as the residual air content in water is released more easily when heated, which ultimately results in an embolism and premature failure. The second possible cause of failure observed was the tiny crevices or imperfections in the lower disc due to mechanical machining (shown in Figure 3.1) where air could slip past the membrane filter and into the system. This became evident during initial testing at higher operating temperatures when air streamed in from the ‘leaf’ and accumulated such that a system failure would occur. However, the addition of a silicone gasket prevented the air leakage from occurring to allow operation and further experimentation at higher ‘leaf’ temperatures, as well as higher pumping heads.

5.7. Possible Causes and Mechanisms of “Leaf” Failure

It was found that the “leaf” failure, as described in Section 4.4, times varied with the pumping head, as shown in Figure 4.6. Generally, at head heights of 1 to 1.8 m the single “leaf” system was able to last between 6 and up to a maximum of 13 days. For higher pumping heads (such as 5 to 8 m) the single “leaf” system only lasted a few hours. For lower pumping heads, gradual bubble collection in the branch tubing was at first identified to be a major contributing factor to the ultimate failure of the surface tension driven water pump. However, after the system was de-aerated it was observed that even if there was no bubble growth or collection in the branch the “leaf” would still fail in roughly the same amount of time. The cause of “leaf” failure was then narrowed down to a possible membrane filter failure over time.

The membrane filter bubble pressure specification is listed in Appendix D.1.4. as 3.5 bar, which results in a capillary pull or pumping head height limitation of nearly 30 m. The limiting pumping head height is far greater than the regular head heights of 1 to 8 m tested experimentally and therefore the recorded “leaf” failure cannot be due to the capillary limit being exceeded. It is believed that the membrane filter is not subjected to an air-water interface with such large surface tension induced pressure gradients for such prolonged periods of time under normal usage. Therefore, it is believed that the membrane filter is damaged in or around the interfacial pores due to surface tension forces. The bubble pressure test is a short test designed to estimate the largest effective capillary radius for a specific membrane filter. This test, however, does not indicate how long a membrane filter can survive during such conditions. Surface tension at the air-water interface produces a pressure drop over the membrane filter which is large enough to sustain the pumping head. At various pumping heads the meniscus at the interface will adjust such that the pressure drop required for the flow and pumping head to be sustained is generated. Figure 5.2 shows a simple force diagram of a capillary tube which clearly indicates the applicable capillary forces. Here it is evident that the vertical component of F_σ is holding the liquid up while the horizontal component of F_σ is actually pulling in on the capillary tube walls. These forces acting on the capillary tube will ultimately affect the pore integrity over time if the material is not sufficiently strong. If this is compared to a case where there is no two phase interface and the same pressure gradient is applied, only a vertical shear force will be experienced on the capillary tube walls, but nothing that can potentially damage or affect the pore integrity. Susman et al. (2009) and Martinez Vilalta et al. (2003) both obtained similar tree lifespans and indicated that the failure resulted from membrane damage due to the pressure difference over the membrane material.

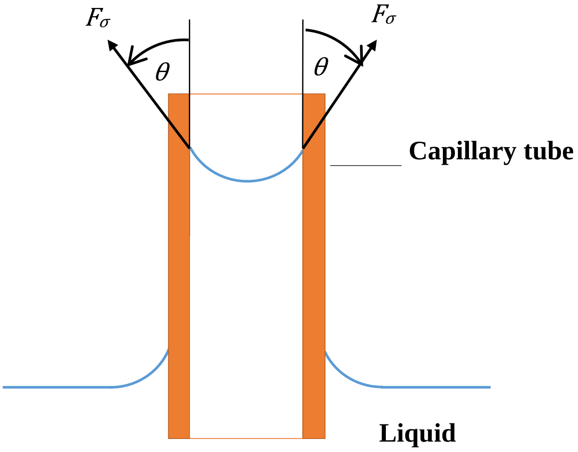

Figure 5.2: Force diagram of a simple capillary tube

Another possible membrane failure mechanism was the uneven wetting of the evaporative surface over time. An example of uneven spreading of the incoming water onto the membrane filter is shown in Figure 5.3 where a used PVA sponge sample is stained by the red die placed in the feed water. It was found that once the membrane filters were wetted and left to dry it had a tendency to become brittle. Therefore, the membrane filter might sustain damage if localised regions are allowed to dry. At times of high evaporative flow rates, the incoming liquid near the centre of the “leaf” might not spread equally to the outer edges of the evaporative surface.

Figure 5.3: PVA Sponge sample with red die stains

5.8. Water Collection Capability

Table 4.14 summarises the water collection data. The tests show that the water leaving the primary water source matches the condensed water vapour collected. The mass balance showed that approximately 98% of the water could be collected after each test on average. The residual water on the cooling coils and walls of the environmental control chamber is believed to be the reason for the slight discrepancy. The average collection rate was also found to be fairly constant for various tests. Furthermore, the cooling coils cooled the air in the environmental control chamber to approximately 13 ºC which increased the relative humidity to approximately 75 to 80%. The addition of heat to the “leaf” allowed evaporative surface temperatures of roughly 15 ºC to be recorded, which increased the evaporative rates substantially.

5.9. Recommendations

The surface tension driven water pump would appear to provide a method for passive water transport for the use in an artificial photosynthesis project, if the functional system lifespan can be increased significantly. It was able to pump water to heights of 1.8 m at a rate of 400 mL/hr.m^2 and functioned up to 13 days. The regular system refilling and replacement of membrane filters would be a costly and tedious process. Also, the system would require constant monitoring for possible embolisms. The plant study conducted in Section 2.4 and Appendix F.2. revealed mechanisms for which water transport in plants are made possible. In the development of a surface tension driven water pump simplicity and functionality was key. However, it is evident that the addition of certain plant features would indeed improve the device significantly.

An alternative more rigid material for the current evaporative layer (membrane filter) must be investigated since the material must be strong enough to withstand the surface tension induced forces to prevent a premature “leaf” failure. It is recommended that a high surface energy or highly hydrophilic material be considered. Possible micro-machining techniques should be investigated to construct an ideal metallic surface with Nano to micro-holes. The use of membrane materials that are more rigid may also be considered. It is further recommended that multiple entry points into each "leaf" be added as this will promote even spreading of incoming water into the "leaf" and reduce the risk of membrane damage.

To reach higher pumping heads it is recommended that the addition of multiple finer tubes of a hydrophilic material (such as cellulose) or high surface energy material be considered to closer replicate the plant vascular bundle, as this will allow water to better adhere to the tube walls and impede water column breakage. Hollow fibre technology (Figure 5.4 and Appendix A.7.) used in bioreactors employ fine tube like filters (approximately Ø200 µm) sealed into a cartridge (FiberCellSystems, 2014) which slightly resembles plant vascular system might be a possible solution. Further, microscopic gas filled cavities in the branches must be deactivated. Heating of the water filled branch tubes is a possible technique.

Figure 5.4: Hollow Fibre cell technology (FiberCellSystems, 2014)

The use of rapid prototyping or 3D printing for the construction of complex "leaf" or tube structures is not recommended. Pore structures required in the "leaf" are on a microscopic level, as low as 0.2 µm, where very respectable 3D printers have an accuracy of approximately 85 µm and print in layer thicknesses as low as 16 µm. Typical layer thicknesses and accuracies are on average 100 µm (Stratasys, 2014). Both structures should ideally be constructed of a highly hydrophilic material and it must be ensured that the particular rapid prototyping procedure is able to produce hydrophilic surfaces. Therefore, "leaf" pore structures would not be accurately reproducible and better alternatives for water transport channels are available.

The use of a distribution manifold is not advised as it produces many complications. However, if a distribution manifold is desired the addition of pit like structures are required between branch connections to prevent embolism from spreading. The use of hydrophilic membranes between branch connections, similar to the membrane filters used in the "leaf", will allow water to flow between branches with the added benefit of preventing air spreading to other branches. A sudden and unpredicted failure can then be restored in time without fear of a total system failure. In general this idea can be carried even further and each branch shortened into smaller sections that are connected by fine pored hydrophilic membranes. The use of a membrane filter will closely resemble pit membranes (as discussed in Appendix F.2.2.) but will be accompanied by greater flow resistance. Therefore, the amount of "artificial" pits must be limited to prevent excessively high capillary limit requirements. Syringe filter discs (as seen in Appendix A.7.) may be considered as a possible connection between various branches.

Finally, the addition of water evaporation rate control from the "leaf" or stomatal control would support the system by lowering the evaporative rate at critical conditions to prevent a catastrophic "leaf" failure. Wessels (2013), as part of his final year mechatronic engineering project at the University of Stellenbosch, attempted to construct a biomimetic surface area control mechanism for the surface tension driven water pump. It was found that controlling pore size is difficult and not an effective means to regulate the evaporative rate. A simpler control mechanism is recommended such as the addition of a secondary hydrophobic layer, for example Hartman Hydrofilm, just after the evaporative surface as it is able to slow the rate of water vapour passing through it. This was experimentally tested and is discussed in Appendix A.6. Alternatively, a mechanism which slides over the evaporative area can be used to directly decrease the exposed evaporative area. An evaporative rate controller would also allow for more constant pumping flow rates rather than high fluctuations.

Regarding the experimental work, it is recommended that a fine scale, as proposed by Susman et al. (2009) and Martinez Vilalta et al. (2003), rather than a simple water level measurements be used as real time changes in mass from the water source can be logged instead of averaged volumetric changes for a time period. This will allow real time comparisons with the actual logged environmental conditions and measured mass flows. Finally, it is recommended that deaerated water be used as the bubble formation in the branch tubing is drastically reduced.

6. CONCLUSIONS AND RECOMMENDATIONS FOR FUTURE WORK

Water pumping is a necessity for daily life and the drive for alternative energies has inspired the development of a tree inspired passive pump. For the development of the surface tension driven pump a vast literature survey was done pertaining to aspects such as surface tension (basic principles, capillary forces, temperature and contaminant effects, wettability), nucleation theory and water tensile strengths, water properties and finally water and mineral transport in trees (plant structures and mechanisms, limiting factors, misconceptions, organic substance transport).

Further, artificial tree designs as approached by botanists were considered to further aid in the development stages. Ultimately, a working prototype with a single "leaf" was developed and functioned up to a maximum of 13 days at pumping head heights up to 1.8 m and was able to pump water at rate of up to 400 mL/hr.m^2. A larger model consisting of multiple grouped "leaves" was also developed.

The experimentation was conducted successfully and focused on design improvement, monitoring pumping performance, system behaviour, capable pumping heads and water collection efficiency. The experimental data was used to develop a simpler statistical prediction for the evaporative flux, by multiple regression analysis. The statistical fits seem show a good correlation with the measured data. A simple theoretical thermal-hydraulic model was developed and compared to the measured data. The simple thermal-hydraulic model also displayed a good correlation with the measured data. A sensitivity analysis was done using the theoretical and statistical formulations. It was shown that the statistical predictions do not lend themselves well to extrapolation.

It was found that the effect of pumping head on the surface tension driven pump flow rate was negligible for the heights tested. It is expected that at much higher pumping heads the flow rate might be decreased slightly due to the increased air-water interface curvature and receded meniscus in the pores of the evaporative layer.

The pumping head height was, however, established to be directly linked to premature "leaf" failure. This is expected to be primarily due to the excessive pressure differences generated across the membrane filter due to surface tension which will ultimately damage the membrane. The use of de-aerated water was established to be crucial at high pumping heads as residual air content is more easily released and large bubble formation will ultimately induce failure. At lower pumping heads the use of de-aerated water was found to prevent excessive bubble formation over time, but did not increase the longevity of the surface tension driven water pump.

Further, the highest pumping head reached was approximately 10 m which is far below the capillary limit for the membrane filters used. The cause of failure here was, however, not deemed to be related to membrane failure, as the boiling of water was observed to occur in the branch tubing. The bulk bubble formation in turn resulted in failure long before possible membrane failure could be observed. Thus spontaneous phase change of metastable water due to weak molecular interactions at the tube walls resulted in premature failure in this case. Therefore heterogeneous nucleation occurred at the water-plastic tube interface and the lack of adhesion encouraged the phase transformation.

The large scale water pump tests indicated that grouped "leaf" behaviour is not so easily predicted or scaled from single "leaf" estimates due to varying flow effects. Furthermore, the use of a distribution manifold to connect the various branches of the surface tension driven water pump can not only complicate the initial filling procedure, but also allow multiple branches to be corrupted due to a single failure in the system. Finally, the water collection tests indicate through a mass balance of the collected evaporated water and water from the water source, that approximately 98% of the water pumped could be collected after each test on average.

In conclusion, the surface tension driven water pump would seem to be a possible passive water transport system for the use in an artificial photosynthesis project if the system longevity can be increased significantly. It is recommended for future work that instead of transparent plastic tubing a different transport material be used. The use of preferably clusters of smaller diameter tubes and various hydrophilic materials, such as hollow fibre capillary technologies, must be investigated. Additionally, alternative more rigid hydrophilic materials for the evaporative layer must be developed or procured. The desired material must be much more rigid than the membrane filters used in the current “leaf”. Other considerations would include the addition of structures with pit-like functions between branches if a manifold design be preferred. This may also prove useful in-between smaller branch sections which together form a single longer continuous branch. Furthermore, the development of evaporative control (stomatal functions) will aid the prevention of capillary failure as well as promote a more constant flow rate. It is recommended that the exposed evaporative area be controlled to regulate the amount of evaporation. Finally, multiple feed water tubes into the “leaf” is suggested as this will encourage more equal spreading of water onto the evaporative layer.

REFERENCES

Amiri, M. C. and Dadkhah, A. A. 2006. On reduction in the surface tension of water due to magnetic treatment. *Colloids and Surfaces A: Physicochemical and Engineering Aspects,* 278(1–3)**,** 252-255.

Angelini, T. E., Roper, M., et al. 2009. Bacillus subtilis spreads by surfing on waves of surfactant. *Proceedings of the National Academy of Sciences,* 106(43)**,** 18109-18113.

Attension. 2012. *Surface tension* [Online]. Available: http://www.attension.com/surface-tension.aspx [Accessed 17 July 2013].

Banks, M. 2009. Engineers call for 'artificial trees' to reduce CO2. Available: http://physicsworld.com/cws/article/news/2009/aug/27/engineers-call-for-artificial-trees-to-reduce-carbon-dioxide [Accessed 06 June 2014].

BBC. 2013. *Photosynthesis* [Online]. Available: http://www.bbc.co.uk/schools/gcsebitesize/science/add_edexcel/organism_energy/photosynthesisrev1.shtml [Accessed 18 February 2014].

Berry, S. and Kedzierski, J. 2008. New Methods to Transport Fluids in Micro-Sized Devices. *Lincoln Laboratory Journal,* 17(2).

Biello, D. 2013. 400 PPM: Can Artificial Trees Help Pull CO2 from the Air? . Available: http://www.scientificamerican.com/article/prospects-for-direct-air-capture-of-carbon-dioxide/ [Accessed 06 June 2014].

Borno, R. T., Steinmeyer, J. D., et al. 2009. Charge-pumping in a synthetic leaf for harvesting energy from evaporation-driven flows. *Applied Physics Letters,* 95(1).

Brower, B. 2013. *Biology 1308 Bonus Credit Chapters--from OPENStax "BIOLOGY"* [Online]. Connexions. Available: http://cnx.org/content/m44708/latest/?collection=col11516/1.2 [Accessed 26 July 2013].

Bull, J. and Grotberg, J. 2003. Surfactant spreading on thin viscous films: film thickness evolution and periodic wall stretch. *Experiments in Fluids,* 34(1)**,** 1-15.

Butt, H. J., Graf, K., et al. 2006. *Physics and Chemistry of Interfaces*. Weinheim: Wiley.

Butt, H. J. and Kappl, M. 2009. *Surface and Interfacial Forces*. Weinheim: Wiley.

Camargo, M. A. B. and Marenco, R. A. 2011. Density, size and distribution of stomata in 35 rainforest tree species in Central Amazonia. *Acta Amazonica,* 41(2)**,** 205-212.

Campbell, N. A. and Reece, J. B. 2008. *Biology*. 8 th ed. Boston: Benjamin Cummings : Pearson.

Carey, V. P. 1992. *Liquid-vapor Phase-change Phenomena: An Introduction to the Thermophysics of Vaporization and Condensation Processes in Heat Transfer Equipment*. 1 ed.: Hemisphere Publishing Corporation.

Carey, V. P. 2008. *Liquid-vapor Phase-change Phenomena: An Introduction to the Thermophysics of Vaporization and Condensation Processes in Heat Transfer Equipment*. 2 ed.: Taylor & Francis Group, LLC.

Caupin, F., Arvengas, A., et al. 2012. Exploring water and other liquids at negative pressure. *Journal of Physics: Condensed Matter,* 24(28)**,** 284110.

Çengel, Y. A. and Cimbala, J. M. 2010. *Fluid Mechanics: Fundamentals and Applications*. 2 ed. New York: McGraw-Hill Higher Education.

Çengel, Y. A., Ghajar, A. J., et al. 2011. *Heat and Mass Transfer: Fundamentals and Applications*. 4 ed. New York: McGraw Hill Higher Education.

Choat, B., Cobb, A. R., et al. 2008. Structure and function of bordered pits: new discoveries and impacts on whole-plant hydraulic function. *New Phytologist,* 177(3)**,** 608-626.

Coder, K. D. 1999. *Basic Water Properties: Attributes and Reactions Essential for Tree Life.* The University of Georgia.

Comstock, J. P. 1999. Why Canny's theory doesn't hold water. *American Journal of Botany,* 86(8)**,** 1077-1081.

Davitt, K., Rolley, E., et al. 2010. Equation of state of water under negative pressure. *The Journal of Chemical Physics,* 133(17).

Denny, M. 2012. Tree hydraulics: how sap rises. *European Journal of Physics,* 33(1)**,** 43.

Dobson, R. T. 2012. *Surface Tension Driven Water Pumping*. Course Notes. University of Stellenbosch, Stellenbosch: Department of Mechanical and Mechatronic Engineering.

FiberCellSystems. 2014. *Advantages of Hollow Fiber Cell Culture* [Online]. Available: http://www.fibercellsystems.com/advantage.htm [Accessed 17 October 2014].

Franks, P. J. L., Ilia J. ; Ruszala, Elizabeth M. 2012. Physiological framework for adaptation of stomata to CO2 from glacial to future concentrations. *Philosophical Transactions Of The Royal Society B-Biological Sciences,* 367(1588)**,** 537-546.

Gaddum, J. H. 1931. A Simple Method of Measuring Surface Tension. *Proceedings of the Royal Society of London. Series B, Containing Papers of a Biological Character,* 109(761)**,** 114-125.

Hacke, U. G. and Sperry, J. S. 2001. Functional and ecological xylem anatomy. *Perspectives in Plant Ecology, Evolution and Systematics,* 4(2)**,** 97-115.

House, K. 2010. *Plant Transport Mechanisms* [Online]. Available: http://home.earthlink.net/~dayvdanls/plant_transport.html [Accessed 15 July 2013].

IBTimes. 2012. *Biomimicry: Designing the Future with Mother Nature's Help* [Online]. Available: http://au.ibtimes.com/articles/252878/20111121/biomimicry-designing-future-mother-nature-s-help__4.htm [Accessed 24 July 2013].

Israelachvili, J. N. 2011. *Intermolecular and Surface Forces: Revised Third Edition,* Elsevier Science.

Koch, K. and Barthlott, W. 2009. Superhydrophobic and superhydrophilic plant surfaces: an inspiration for biomimetic materials. *Philosophical Transactions of the Royal Society A: Mathematical, Physical and Engineering Sciences,* 367(1893)**,** 1487-1509.

Kouwenberg, L. M., JC ; Kurschner, WM ; et al. 2003. Stomatal frequency adjustment of four conifer species to historical changes in atmospheric CO2. *American Journal of Botany,* 90(4)**,** 610-619.

Kramer, P. J. and Boyer, J. S. 1995. *Water Relations of Plants and Soils*. Academic Press.

Leybovich, I. 2012. *Mother Nature as Muse: The Future of Design* [Online]. Industry Market Trends. Available: http://news.thomasnet.com/IMT/2012/04/10/mother-nature-as-muse-the-future-of-design/ [Accessed 29 July 2013].

Martinez Vilalta, J., Sauret, M., et al. 2003. Make your own transpiring tree. *Journal of Biological Education,* 38(1)**,** 32-35.

Meinzer, F. C. 1993. Stomatal control of transpiration. *Trends in Ecology & Evolution,* 8(8)**,** 289-294.

Mercury, L., Jamme, F., et al. 2012. Infra-red imaging of bulk water and water-solid interfaces under stable and metastable conditions. *Physical Chemistry Chemical Physics,* 14(8)**,** 2864-2874.

Namasivayam, V., Larson, R. G., et al. 2003. Transpiration-based micropump for delivering continuous ultra-low flow rates. *Journal of Micromechanics and Microengineering,* 13(2)**,** 261-271.

Nichols, M. 2014. *Redwoods: The Super Trees* [Online]. Available: http://ngm.nationalgeographic.com/2009/10/redwoods/nichols-photography#/04-lone-tree-714.jpg [Accessed 15 March 2014].

Okawa, D., Pastine, S. J., et al. 2009. Surface Tension Mediated Conversion of Light to Work. *Journal of the American Chemical Society,* 131(15)**,** 5396-5398.

Peramaki, M. 2005. *A physical analysis of sap flow dynamics in trees.* Department of Forest Ecology, University of Helsinki.

PHYWE. 1998. *Surface Tension by the Ring Method (Du Nouy Method)* [Online]. Available: http://www.nikhef.nl/~h73/kn1c/praktikum/phywe/LEP/Experim/1_4_05.pdf [Accessed 17 July 2013].

Quere, D. 2002. Rough Ideas on Wetting. *Physica A,* 313(1-2)**,** 32-46.

Reece, S. Y., Hamel, J. A., et al. 2011. Wireless Solar Water Splitting Using Silicon-Based Semiconductors and Earth-Abundant Catalysts. *Science,* 334(6056)**,** 645-648.

Roman, F. L., Faro, J., et al. 2000. A simple experiment for measuring the surface tension of soap solutions. *American Journal of Physics,* 69(8)**,** 920-921.

Sang Kug, C., Kyungjoo, R., et al. A Surface-Tension-Driven Propulsion and Rotation Principle for Water-Floating Mini/Micro Robots. Micro Electro Mechanical Systems, 2009. MEMS 2009. IEEE 22nd International Conference on, 25-29 Jan. 2009 2009. 1083-1086.

Saupe, S. G. 2009. *Water Transport* [Online]. Collegeville, MN: St. John's University: Biology Department. Available: http://employees.csbsju.edu/ssaupe/biol327/Lecture/water-trans.htm [Accessed 3 March 2014].

Schönherr, J. and Bukovac, M. J. 1972. Penetration of Stomata by Liquids: Dependence on Surface Tension, Wettability, and Stomatal Morphology. *Plant Physiology,* 49(5)**,** 813-819.

Schymanski, S. J., Or, D., et al. 2013. Stomatal Control and Leaf Thermal and Hydraulic Capacitances under Rapid Environmental Fluctuations. *PLoS ONE,* 8(1)**,** e54231.

Sedgewick, S. A. and Trevena, D. H. 1976. Limiting negative pressure of water under dynamic stressing. *Journal of Physics D: Applied Physics,* 9(14)**,** 1983.

Speer, B. 1995. *Monocots versus Dicots: The Two Classes of Flowering Plants* [Online]. Available: http://www.ucmp.berkeley.edu/glossary/gloss8/monocotdicot.html [Accessed 15 February 2014].

Sperry, J. S. 2003. Evolution of water transport and xylem structure *International Journal of Plant Science,* 164(3).

Sperry, J. S. 2011. *Hydraulics of vasular water transport. Signalling and Communication in Plants: Mechanical Integration of Plant Cells and Plants.* Berlin: Springer.

Starr, C., Taggart, R., et al. 1978. *Biology: The Unity and Diversity of Life*. 4 ed. Belmont: Wadsworth.

Stiller, V. and Sperry, J. S. 1999. Canny's compensating pressure theory fails a test. *American Journal of Botany,* 86(8)**,** 1082-1086.

Stratasys. 2014. *3D Printers* [Online]. Available: http://www.stratasys.com/3d-printers [Accessed 2 October 2014].

Susman, K., Razpet, N., et al. 2009. Modeling The Water Transport In Tall Trees. Faculty of Education, University of Ljubljana, Slovenia.

Tyree, M. T. 1997. The Cohesion-Tension theory of sap ascent: current controversies. *Journal of Experimental Botany,* 48(10)**,** 1753-1765.

Tyree, M. T. and Sperry, J. S. 1988. Do Woody Plants Operate Near the Point of Catastrophic Xylem Dysfunction Caused by Dynamic Water Stress? *Plant Physiology American Society of Plant Biologists,* 88(3)**,** 574-580.

Wessels, F. J. 2013. *Biomimetic Surface Area Control Mechanism*. University of Stellenbosch: Department of Mechanical and Mechatronic Engineering.

Wheeler, T. D. and Stroock, A. D. 2008. The transpiration of water at negative pressures in a synthetic tree. *Nature,* 455(7210)**,** 208-212.

Williams, P. R., Williams, P. M., et al. 1999. On the tensile strength of water under pulsed dynamic stressing. *Proceedings of the Royal Society of London.*

Series A: Mathematical, Physical and Engineering Sciences, 455(1989)**,** 3311-3323.

Wullschleger, S. D., Meinzer, F. C., et al. 1998. A review of whole-plant water use studies in trees. *Tree Physiology*, 18(1)**,** 499-512.

Zarinkamar, F. 2007. Stomatal Observations in Dicotyledons. *Pakistan Journal of Biological Sciences*, 10(1)**,** 199-219.

APPENDIX A: PRACTICAL ASSIGNMENTS AND RELATED FUTURE WORK

For the purpose of the course some practical problems where attempted as to better understand plant structures, the surface tension phenomena, certain materials used as well as to apply some of the covered theoretical work. Further materials and techniques for investigation in related future work are also listed.

A.1. Practical 1: Stomata Investigation

For the stomata investigation light microscope images were taken of various tree leaves in order to physically see the plant vein structures and stoma as shown in Figure A.1.

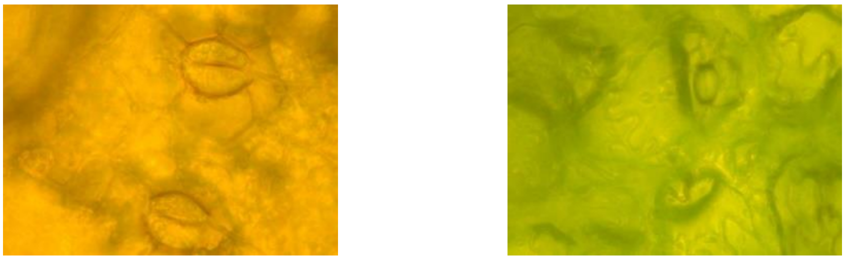

(a) *Nasturtiums* ("Kappertjies") **(b) *Qurcus Robus* (Normal oak)**

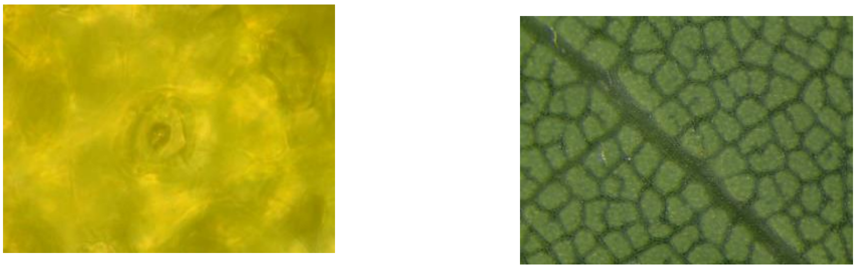

(c) *Camellia Juponica* **(d) Typical leaf vein structure**

Figure A.1: Self taken microscope images of various tree leaves

A.2. Practical 2: Demonstration of the Effect of Surfactant on Surface Tension

The purpose of this practical was to demonstrate the effect that a surfactant has on a liquid-vapour interface. For the investigation a light boat was constructed, placed on a water surface and propelled forward using normal dishwashing liquid. F_σ is the surface tension force and θ the contact angle. In this balanced state the net force interaction on the boat is zero and therefore the boat stays stationary, as shown in Figure A.2.

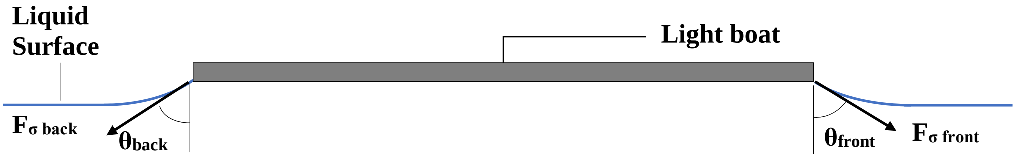

Figure A.2: Side view of Light Boat on liquid surface (Free body diagram)

However, it is quite simple to see that a localised decrease in surface tension either at the front or back of the boat will significantly decrease the surface tension force at the front or back, respectively. This will momentarily induce a net force that will propel the boat forward.

A.3. Practical 3: Determination of the Effective Capillary Radius of a Superabsorbent Sponge Material

For this practical the aim was to successfully determine the effective capillary radius of the superabsorbent PVA sponge. The porosity as well as the capillary radius of sponge material was determined. Three sponge samples were initially marked to indicate the water level in each container. Samples 1 and 3 were initially bone dry before the test, while the second sample was initially wetted and the excess water removed. Red food colouring was added to the water and the containers closed with the sponge material partially submerged. The setup is shown in Figure A.3. With the red food colouring the steady pull of water up through sponges were to be observed more clearly. The samples were then left over night for an approximate time of 16 hours. Thereafter the samples were removed and the height to which the water and food colouring was pulled measured. The capillary formula as indicated in Equation 2.6 was then used to determine the effective capillary radius for the porous sponge material.

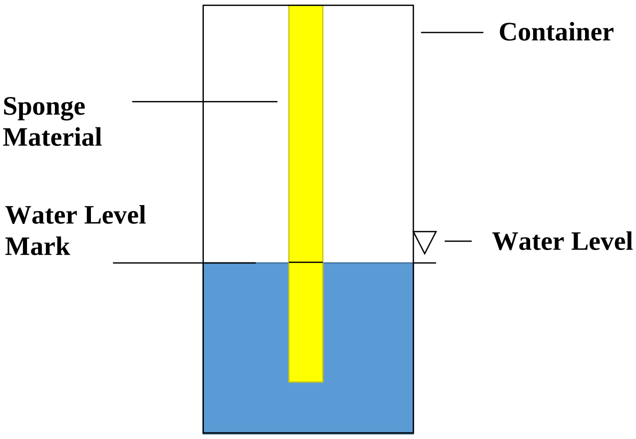

Figure A.3: Container setup

Porosity is generally an attribute of a porous material and is therefore able to hold liquids. It is defined as the volumetric void fraction over the total volume. In the case of sponge material the total volume will increase from a bone dry state to a fully wetted state. Therefore the bone dry and water saturated mass balance were considered, respectively. It was assumed that the volume of sponge material and density of the sponge material would stay constant. In the wetted state it was assumed all air content was removed while in the bone dry state all water content was removed.

$$Porosity = \frac{V_{void}}{V_{total}}$$
$$Porosity = \frac{m_{wet} - m_{dry}}{(\rho_{water} - \rho_{air})V_{total}} \quad \text{(F.2.1)}$$

using the total volume from dimensional measurements of the wetted sponge.

A.4. Practical 4: Comparison of Measured Sessile Drop Shapes to Numerically Simulated Results

The goal of this practical was to apply the sessile drop technique to measured droplets on various surfaces. The assignment allowed the study of contact angles, sessile drops, measurement thereof as well as numerical simulations with measured data. Same volume water droplets were placed on various surfaces and measurements such as maximum diameter, contact angle and droplet height were made. With the contact angle known the maximum diameter and droplet height were compared to numerical solutions as shown in Figure A.4.

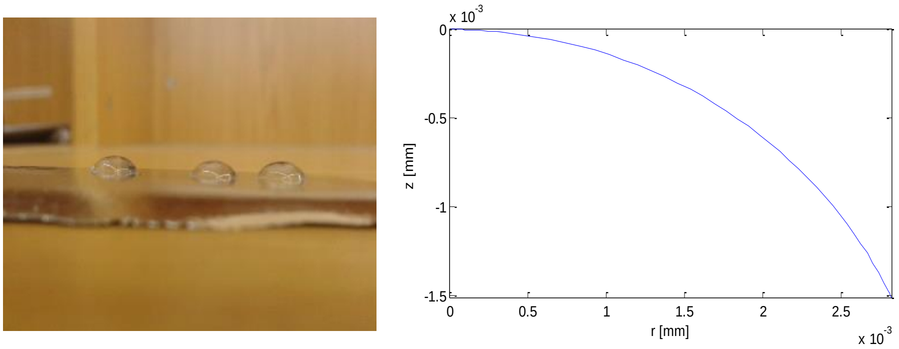

Figure A.4: Sessile drop comparisons

A.5. Practical 5: Permeability of a Superabsorbent Sponge

The purpose of the practical was to gain a better understanding of Darcy flow through porous materials and to determine the intrinsic permeability of a PVA sponge. A *permeameter* utilising the falling head test was constructed and used in the experimentation, as shown in Figure A.5. For this setup it can easily be shown that the intrinsic permeability is:

$$\dot{V}_{out} - \dot{V}_{in} = \frac{dV}{dt}$$

$$\dot{V}_{out} = \frac{dV}{dt} => dV = adz$$

$$\dot{V}_{out} = \frac{\kappa A}{\mu}\left(\frac{\Delta P}{L} - \rho g\right) => \Delta P = -\rho g(z - L)$$

$$\dot{V}_{out} = -\frac{\kappa A \rho g z}{\mu L} = \frac{adz}{dt} \text{ and intergrate to yield}$$

$$\kappa = \frac{\mu}{\rho g}\frac{a}{A}\frac{L}{\Delta t}\ln\left(\frac{z}{H_1}\right) \tag{F.5.1}$$

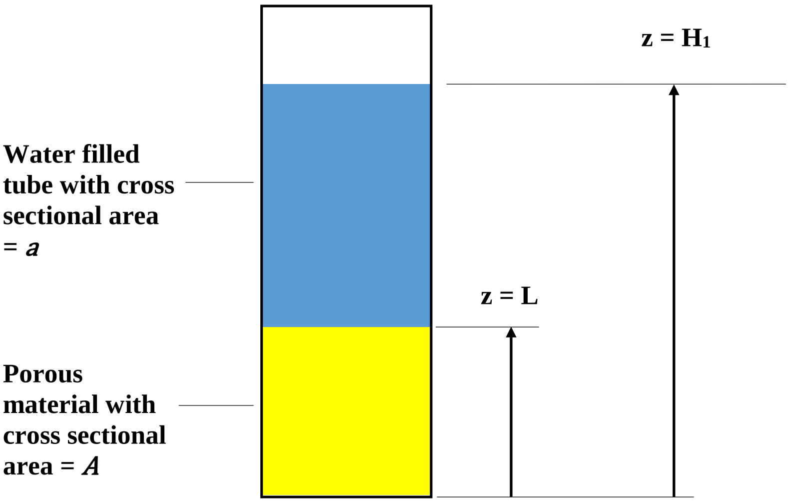

Figure A.5: Falling head test setup

A.6. Practical 6: Evaporation Rates through a Hydrophobic Membrane

The practical was aimed at determining the effect of the addition of a secondary hydrophobic layer after a hydrophilic material on evaporation rates. PVA sponge samples were used as a base hydrophilic material and Hartmann Hydrofilm as hydrophobic material. Two samples were compared simultaneously for the various tests, one with the hydrophobic layer and the other without, as shown in Figure A.6. To prevent vapour escaping from the sample edges, the edges were sealed. The exposed evaporative surface was the same for both samples. A test with zero air velocity as well as a forced velocity test was conducted. After a fixed time period the sponge samples were measured and the drying rate determined.

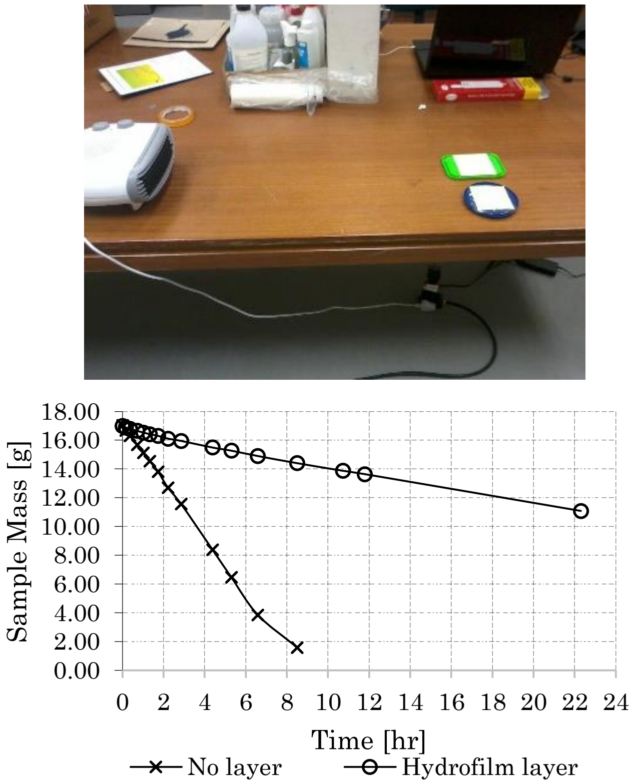

Figure A.6: Evaporation test setup with sample mass reduction over time

A.7. Related Future Work

This includes the investigation and use of hollow fibre cell technology (Figure A.7), membrane filter syringe discs (Figure A.8) and Nano/micro machining (Figure A.9). Figure A.9 is a summary of the various micro manufacturing techniques for consideration in the future construction of a surface tension driven water pump.

Figure A.7: Hollow fibre cartridge
(FiberCellSystems. 2011. *Production of Recombinant Proteins and Monoclonal Antibodies in Hollow-Fiber Bioreactors*. [Online]. Available: http://www.fibercellsystems.com/documents/Article-RecombinantandMonoclonal-Cadwell.pdf. [Accessed 17 November 2014].)

Figure A.8: Syringe filter discs

(Membrane filter syringe discs (Merck Millipore. 2014. *Millex Syringe Filter Unit*. [Online]. Available: https://www.emdmillipore.com/GB/en/product/Millex%C2%AE-Syringe-Filter-Units%2C-Non-Sterile%2C-425mm,MM_NF-C9087. [Accessed 3 November 2014].)

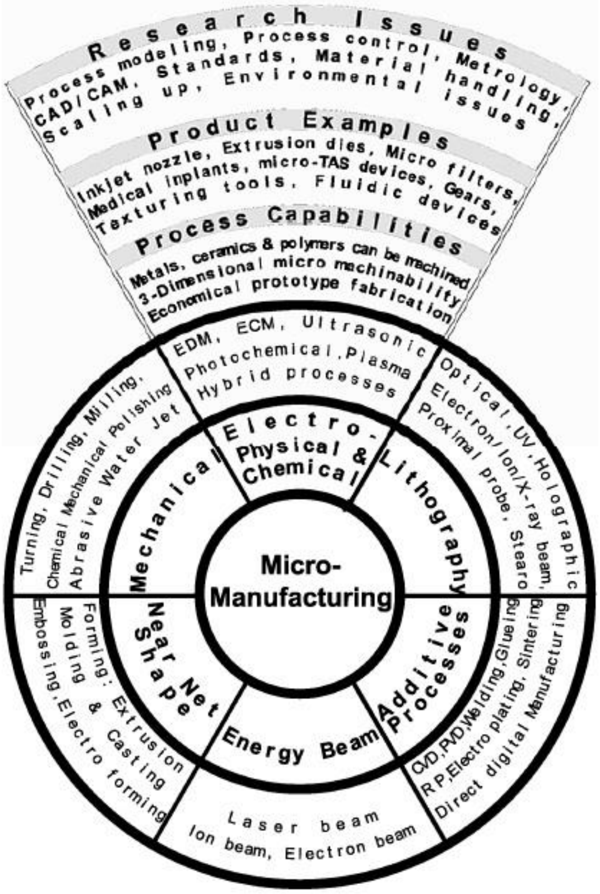

Figure A.9: Summary of current micro machining techniques

(Micro manufacturing techniques (Rajurkar, K. P., Levy, G., et al. 2006. Micro and Nano Machining by Electro-Physical and Chemical Processes. *CIRP Annals - Manufacturing Technology*, 55(2), 643-666)

APPENDIX B: SURFACE TENSION DRIVEN WATER PUMP DETAIL DESIGN DRAWINGS

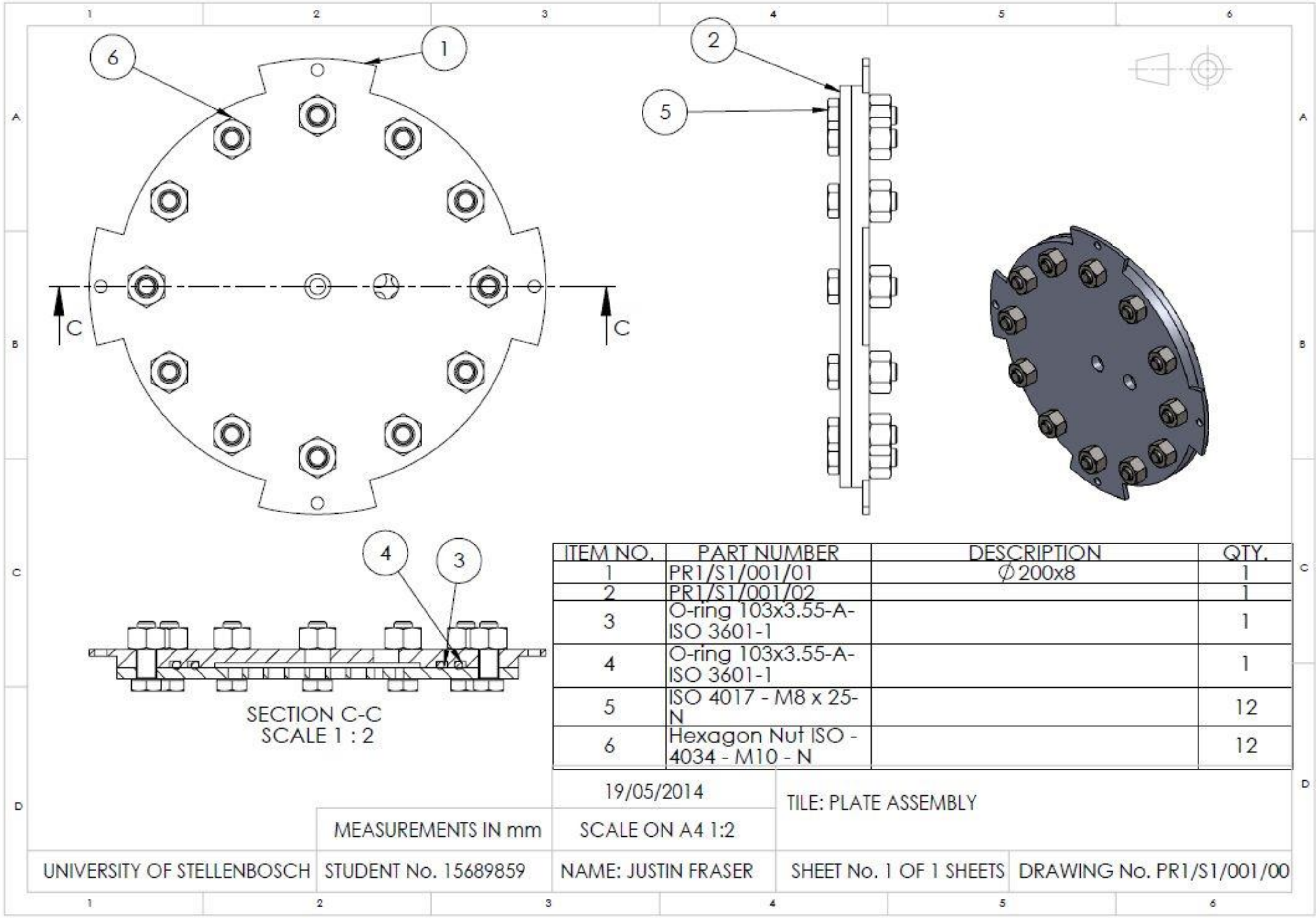

ITEM NO.	PART NUMBER	DESCRIPTION	QTY.
1	PR1/S1/001/01	∅200x8	1
2	PR1/S1/001/02		1
3	O-ring 103x3.55-A-ISO 3601-1		1
4	O-ring 103x3.55-A-ISO 3601-1		1
5	ISO 4017 - M8 x 25-N		12
6	Hexagon Nut ISO - 4034 - M10 - N		12

19/05/2014
TILE: PLATE ASSEMBLY
MEASUREMENTS IN mm
SCALE ON A4 1:2
UNIVERSITY OF STELLENBOSCH
STUDENT No. 15689859
NAME: JUSTIN FRASER
SHEET No. 1 OF 1 SHEETS
DRAWING No. PR1/S1/001/00

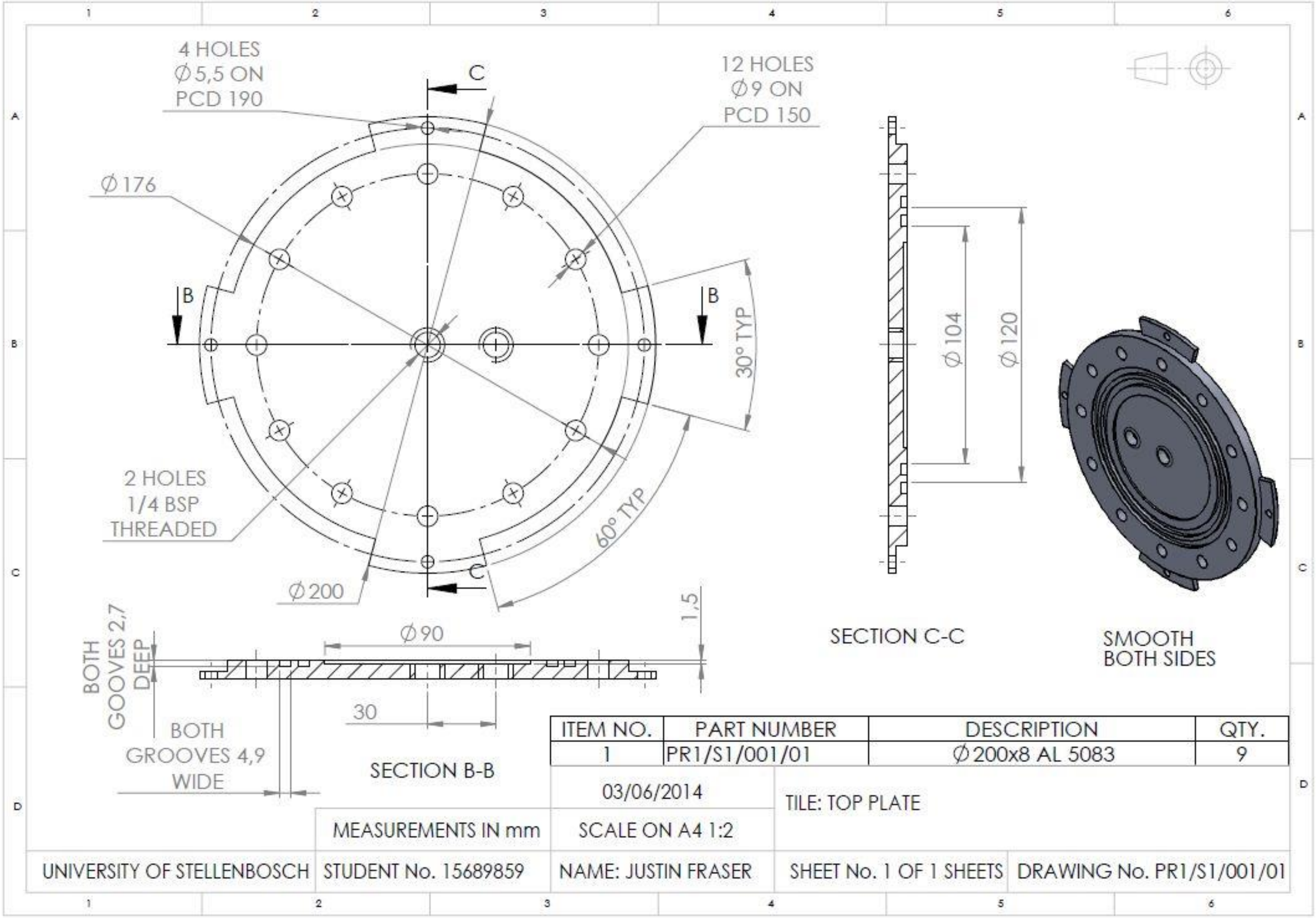

ITEM NO.	PART NUMBER	DESCRIPTION	QTY.
1	PR1/S1/001/01	Ø200x8 AL 5083	9

03/06/2014

TILE: TOP PLATE

MEASUREMENTS IN mm

SCALE ON A4 1:2

UNIVERSITY OF STELLENBOSCH

STUDENT No. 15689859

NAME: JUSTIN FRASER

SHEET No. 1 OF 1 SHEETS

DRAWING No. PR1/S1/001/01

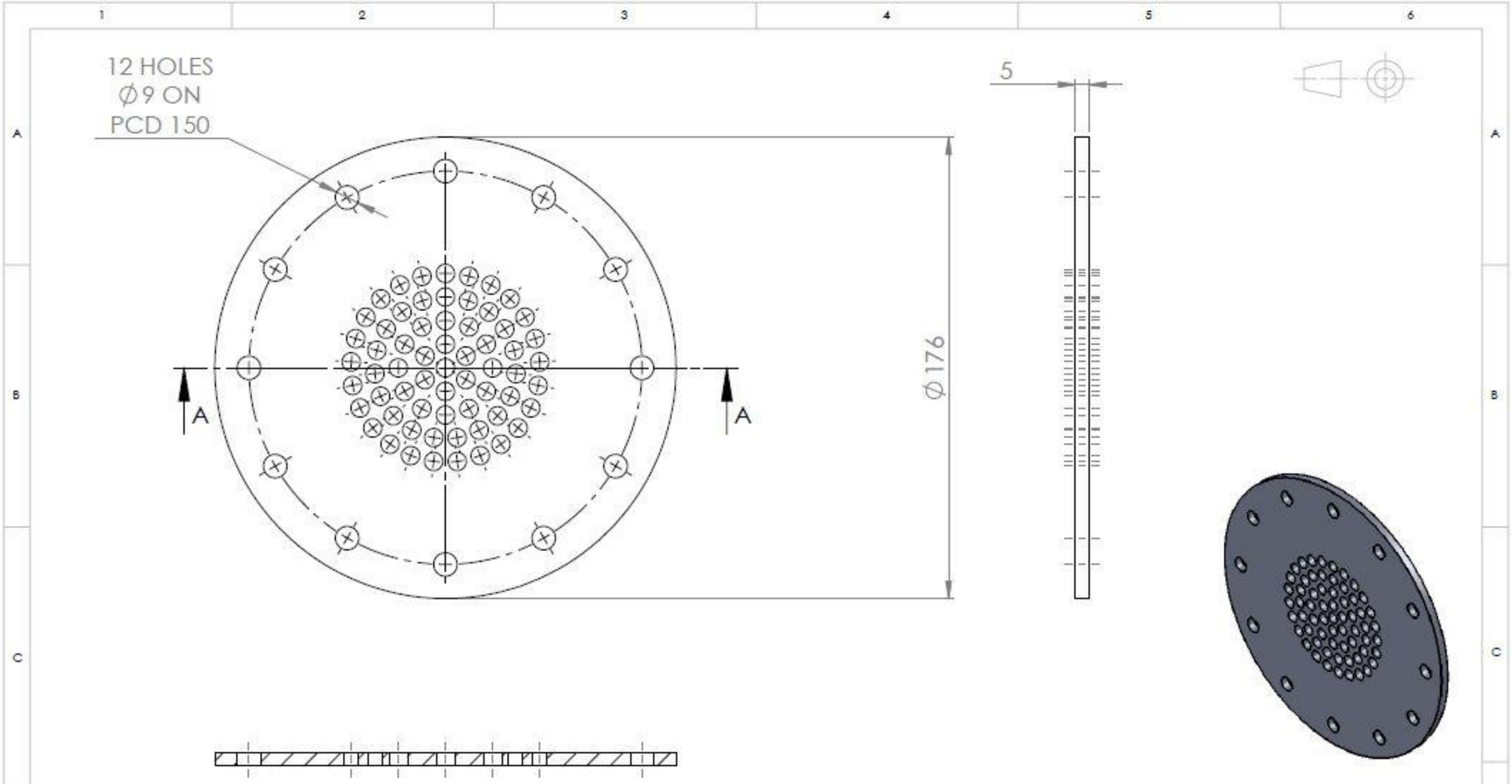

SECTION A-A

ITEM NO.	PART NUMBER	DESCRIPTION	QTY.
1	PR1/S1/001/02	Ø176x5 AL 5083	9

03/06/2014

TILE: BOTTOM PLATE

MEASUREMENTS IN mm

SCALE ON A4 1:2

UNIVERSITY OF STELLENBOSCH

STUDENT No. 15689859

NAME: JUSTIN FRASER

SHEET No. 1 OF 1 SHEETS

DRAWING No. PR1/S1/001/02

APPENDIX C: TYPICAL TREE EVAPORATIVE FLUX RATES

The evaporation rates per unit area for various tree species were obtained by considering various sources. Most data on tree evaporation rates would seem not to have a global standardised presentation. The variations in the units for the evaporation rates required the data to be slightly modified to a standardised unit of measurement. Additionally, some sources did not explicitly provide the evaporative flux, but instead provided the tree daily water usage as well as total leaf area. Therefore the evaporative flux was determined from the data. The tables below present the evaporative flux rates for various tree species as obtained from the various sources.

Table C.1 was taken from Tyree and Sperry (1988) where only the extreme evaporative flux rates of certain tree species were given.

Table C.1: Extreme evaporative flux rates for various tree species [modified from Tyree and Sperry (1988)]

Species	**Evaporative flux rate [mL/hr.m^2]**
Thuja occidentalis	64.93
Acer saccharum	505.01
Cassipourea elliptica	721.44

Table C.2 was taken from Wullschleger et al. (1998) where the maximum daily tree water usage as well as total leaf area per tree was given.

Table C.2 Maximum daily evaporative flux rates for various tree species [modified from Wullschleger et al. (1998)]

Species	**Evaporative flux rate [mL/hr.m^2]**
Picea abies	16.35
Pinus radiata	23.63
Abies amabilis	27.10
Eucalypus grandis	33.17
Eucalyptus regnans	36.06
Eucalyptus regnans	42.89
Pinus radiata	48.57
Eucalypus grandis	53.76
Eucalypus grandis	82.91
Eucalyptus globulus	90.87
Eucalyptus wandoo	101.01

Salix fragilis	102.39
Eucalyptus fastigata	108.98
Carya illinoensis	119.42
Carya illinoensis	145.64
Banksia grandis	150.30
Salix matsudana	158.05
Populus´ euramericana	175.03
Eucalyptus cladocalyx	178.93
Banksia grandis	191.67
Eucalyptus occidentalis	208.75
Eucalyptus saligna	240.06
Eucalyptus camaldulensis	242.15
Eucalyptus robusta	264.42
Eucalyptus wandoo	281.81
Eucalyptus sargentii	292.25
Eucalyptus kondininensis	354.88
Eucalyptus platypus	389.67
Eucalyptus loxophleba	417.50
Eucalyptus leucoxylon	480.13

Table C.3 was taken from Kramer and Boyer (1995) where the study focussed on young seedlings. Only the evaporation rate per tree and the average leaf area per tree was given. The data was collected during the months of August to September.

Table C.3: Various tree seedling evaporative flux rates [modified from Kramer and Boyer (1995)]

Species	**Evaporative flux rate [mL/hr.m^2]**
Loblolly Pine	21.21
Yellow poplar	40.72
Northern Red oak	52.02

Table C.4 was taken from Kramer and Boyer (1995) where the evaporative flux rates for various tree species were given and the evaporation rate measurements made from July to September.

Table C.4: Various tree evaporative flux rates [modified from Kramer and Boyer (1995)]

Species	**Evaporative flux rate [mL/hr.m^2]**
Pinus taeda	19.41
Pinus taeda	21.21
Acer negundo	26.72
Quercus rubra	33.82
Platanus occidentalis	36.74
Clethra alnifolia	40.62
Liriodendron tulipifera	40.75
Liriodendron tulipifera	42.21
Myrica cerifera	45.09
Liriodendron tulipifera	49.18
Quercus rubra	50.18
Acer saccharum	50.94
Quercus rubra	51.98
Quercus alba	59.33
Ilex glabra	67.22
Gordonia lasianthus	74.19

APPENDIX D: MATERIAL SPECIFICATIONS

The following section contain detailed specifications for most of the materials used during the entire breadth of the project

D.1. Internal Leaf Materials

D.1.1. Hartmann Hydrofilm

Hartmann Hydrofilm is a fully-transparent adhesive dressing made of a waterproof polyurethane film and a hypoallergenic adhesive. It is used to protect wounds against secondary infections, for the sterile treatment of superficial injuries. The material is a hydrophobic material and on average lets 1300 g/m^2 of water vapour pass through it in 24 hr. This was confirmed by experimentation as discussed in Appendix A.6. These results were verified personally by measuring the mass of a Hydrofilm covered sponge over time. The results were also compared with a sponge with no Hydrofilm covering to ensure that the Hydrofilm indeed does trap water vapour.

Figure D.1: Hartmann Hydrofilm

Hartmann. 2014. *Hydrofilm.* [Online]. Available: http://za.hartmann.info/158773.php. [Accessed 25 September 2014].

D.1.2. Munktell Filter Paper

The Munktell lab filtration filter paper used is an ashless filter paper which is recommended for high purity quantative analysis. Each filter paper is acid washed to remove impurities. Additionally, the cellulose content is nearly 100% with an ash content less than 0.01%. The particular grade, 393, is typically used in slow filtration and due to its very tight fiber matrix is excellent for particularly fine precipatates.

The Munktell grade 393 filter paper (Quant.) specifications are:

Diameter: 90 mm
Basic weight: 100 g/m^2
Filtration speed: 250 s/10 mL
Herzberg: 2500 s/100 mL
Typical Retention: 1-2 µm

Figure D.2: Munktell filter paper

Munktell Ahlstrom. 2014. *Munktell Ahlstrom filtration catalogue EN.* [Online]. Available: http://munktell.com/globalassets/munktell-blocks/catalog/en_munktell_filtrationcatalogue.pdf. [Accessed 26 September 2014].

D.1.3. Super Absorbent (PVA) Sponge

PVA sponges seem to resemble a normal sponge, however on a microscopic level it has numerous interconnected hollow cells, such that it is roughly 90% hollow.

Figure D.3: Super absorbent sponges

Amazon. 2014. *PVA Sponge.* [Online]. Available: http://www.amazon.com/PVA-Sponge-Large-6-25-Sponge/dp/B000ZOWG1C. [Accessed 25 September 2014].

The sponge contains open pores connected three dimensionally to form continuous pores. It has a remarkable physical structure allowing for many functions and applications. The elasticity and tensile properties of PVA sponges allow safe application without harmful side effects during cleaning or wiping uses. It may be used to clean hard disks or silicon wafers. Ordinary daily-life purposing includes cleaning tools and cars, cosmetic puffs as well as typical sponge uses. PVA sponges are extremely hydrophilic and possess an impressive retention capability which surpasses regular urethane based sponges. AION. n.d. *About PVA Sponge*. [Online]. Available: http://www.aion-kk.co.jp/en/products/pva/. [Accessed 25 September 2014]

The super absorbent sponge material does not have any specifications except that it is made from a high density polyvinyl alcohol (PVA). Permeability tests were conducted by the author on the material and an average intrinsic permeability of $3.375(10)^{-11}$ m^2 estimated. Other tests included average porosity tests as well as effective capillary radius determination. It was found that the average porosity is roughly 91 to 96% and that the effective capillary radius is nearly 200 µm.

D.1.4. Millipore Membrane Filters

Durapore® membrane filter
The Durapore® membrane filter used is composed of Hydrophilic Polyvinylidene fluoride (PVDF) membrane. Hydrophilic Durapore® membrane filters allow high flow rates with low extractables and is compatible with a broad spectrum of chemicals. These membrane filters bind far less protein than nylon, nitrocellulose or PTFE membranes.

The Millipore Durapore® membrane filter specifications are:

Trade name: Durapore
Code: GVWP09050
Filter colour: White
Maximum operating temperature: 85 °C
Filter type: Screen filter
Wettability: Hydrophilic
Pore Size: 0.22 µm
Bubble Point at 23 °C: ≥3.45 bar, air with water
Gravimetric Extractables: 0.5%
Porosity: 70%
Air Flow Rate: 2 L/min/cm^2
Water Flow Rate: > 1 mL/min/cm^2
Thickness: 125 µm
Filter Diameter: 90 mm
Chemistry: Hydrophilic PVDF

Merck Millipore. 2014. *Durapore® Membrane Filters*. [Online]. Available: http://www.emdmillipore.com/US/en/product/Durapore%C2%AE-Membrane-Filters,MM_NF-C7631. [Accessed 26 September 2014].

MF- membrane filter

The MF-Millipore™ membrane filter used is composed of mixed cellulose membrane. MF-Millipore™ membranes are widely used in analytical/research applications due to its biological inert mixed composition of cellulose acetate and cellulose nitrate.

The MF-Millipore™ membrane filter specifications are:

Trade name: MF-Millipore
Code: GSWP09000
Filter colour: White
Maximum operating temperature: 75 °C
Filter type: Filter discs
Wettability: Hydrophilic
Pore Size: 0.22 µm
Bubble Point at 23 °C: ≥3.52 bar, air with water
Gravimetric Extractables: 2%
Porosity: 75%
Air Flow Rate: 2 L/min/cm²
Water Flow Rate: 18 mL/min/cm²
Thickness: 150 µm
Filter Diameter: 90 mm
Chemistry: Mixed Cellulose Esters

Merck Millipore. 2014. *MF-Millipore™ Membrane Filters*. [Online]. Available: http://www.emdmillipore.com/GB/en/product/MF-Millipore%E2%84%A2-Membrane-Filters,MM_NF-C152. [Accessed 26 September 2014].

D.2. Experimental Setup Materials

D.2.1. Cooler Master Axial flow Fans

Cooler Master MegaFlow
Dimensions: 200 x 230 x 30 mm
Rated Voltage: 12 V DC
Rated Current: 0.40 A
Fan Speed: 900± 10% RPM
Air Flow: 150 ± 10% CFM

Figure D.4: Cooler Master MegaFlow

Cooler Master. 2014. *MegaFlow 200 Red LED Silent Fan*. [Online]. Available: http://eu.coolermaster.com/uk/product/Detail/cooling/megaflow/megaflow-200-red-led-silent-fan.html. [Accessed 25 September 2014].

Cooler Master SickleFlow X
Dimensions: 120 x 120 x 25 mm
Rated Voltage: 12 V DC
Rated Current: 0.35 A
Fan Speed: 2000 ± 10% RPM
Air Flow: 90 ± 10% CFM

Figure D.5: Cooler Master SickleFlow X

Cooler Master. 2014. *SickleFlow 120 2000 RPM Green LED*. [Online]. Available: http://eu.coolermaster.com/uk/product/Detail/cooling/sickleflow/sickleflow-120-2000rpm-green-led.html. [Accessed 25 September 2014].

D.2.2. BISCA 2500 Water Pump

The BISCA 2500 is small water feature or pond pump functioning with a small rotor to pump water.

Figure D.6: BISCA 2500 water pump

AllPondPumps.com. 2014. *Pond Pump HQB-2500 530gph*. [Online]. Available: http://www.allpondpumps.com/pond/Pond-pumps/water-pump-HQB-2500.html. [Accessed 25 September 2014].

The pump specifications as listed on the packaging:
Dimensions: 153x105x135 mm
Rated Voltage: 110 V/230 V

Frequency: 60 Hz/50 Hz
Power: 55 W
Max.head: 2.5 m
Max.output: 2000 L/h
Weight: 1.2 kg

D.2.3. Heating Pads

Rated 9 W the heating pads (21 x 15 cm) can reach temperatures of up to 40 ºC if it is well insulated. The heating pads are connected directly to a 230 V AC power supply.

Figure D.7: Heating pad
Reptile City. 2014. *Foil Heating Pad, Small (15x21cm) 9w*. [Online]. Available: http://www.reptilecity.co.za/catalog/product_info.php?pName=foil-heating-pad-small-15x21cm-9w&cName=heating-pads-cables. [Accessed 25 September 2014].

D.2.4. Hailea HC-150A Water Chiller

The Hailea HC-150A is a small aquarium water chiller functioning with a standard refrigeration cycle and temperature control unit.

Figure D.8: Hailea HC-150A water chiller

The chiller specifications as listed:

Model: HC-150A
Power: 1/10 HP
Voltage: 220~240 V(110~120 V)

Frequency: 50 Hz(60 Hz)
Working Current: 1.1 A(2.2 A)
Water Refrigerated: 50~400 L
Iced Medium: R134a
Rate of Flow: 250~1200 L/h
Weight: 15 kg
Size: 420x248x365 mm
Pull down from ambient: 150 L 12 ºC or 300 L tot 6 ºC

Hailea. 2014. *Chiller: Model HC-150A*. [Online]. Available: http://www.hailea.com/e-hailea/product1/HC-150A.html. [Accessed 25 September 2014].

D.2.5. RS232 BTU-PSYCHROMETER AZ 8912

RS232 BTU-PSYCHROMETER AZ 8912 is able to measure air velocity and relative humidity information with its built-in remote vane.

Figure D.9: AZ 8912 Psychrometer

The psychrometer specifications are:

Stellenbosch Serial Number: 9635754
Air Velocity: 0.3 ~ 35 m/s
Accuracy: ±5%
Resolution: 0.1
Air Volume: 0 ~ 99999 m^3/s
Accuracy: ±5%
Resolution: 0.1(0~9999.9)
BTU Capacity: 0 ~ 99999 BTU/H (KW)
Accuracy: ±3%
Resolution: 0.1
Vane Dimensions: 170x77x40 mm^3
Meter Dimension: 175x70x33 mm^3

AZ Instrument. 2014. *8912 Anemometer+RH%*. [Online]. Available: http://www.az-instrument.com.tw/en/productsinfo/142.html. [Accessed 25 September 2014].

D.2.6. Huato S100-EX+ Data Logger

The Huato S100-EX+ is a portable battery operated and convenient data logger which monitors ambient air temperature, relative humidity and dew point temperatures with its measuring probe. It also includes a USB interface for easy data retrieval. The unit comes complete with a certificate of quality assurance and traceable calibration.

Figure D.10: Huato S100-EX+ data logger

The Huato S100-EX+ specifications are:

Air Velocity: 0.3 ~ 35 m/s
Accuracy: ±0.5°C; ±5%RH
Resolution: 0.1°C, 0.1%RH
Memory: 43,000 readings
Measurement Range: -40 to +85°C
Storage Temperature: 35 to +80°C
Battery: 2 * AAA (1.5V Battery)
Logging rate: 2s ~ 24h
LCD display area: 42x20mm^2
Vane Dimensions: 92x57x20mm^3
Weight: 150g(without battery) / 200g(with battery)

Huato. 2014. *S100 Temperature and Humidity Data Logger*. [Online]. Available: http://www.huato.cn/s100_th.html. [Accessed 25 September 2014].

D.2.7. 34970A Data Acquisition / Data Logger Switch Unit

The Agilent Data Acquisition / Data Logger Switch Unit is a product from Keysight Technologies. It contains a three-slot mainframe with a built-in 6 1/2 digit digital multimeter. Each channel can be configured independently to measure one of 11 different functions such as voltage or temperature etc. Various plug-in modules allows either a data logger or data acquisition system or a switching unit. On-module screw-terminal connections are employed to connect the various measuring probes. A convenient built-in thermocouple reference is featured with the 34901A plug-in module

The 34970A Data Acquisition / Data Logger Switch Unit specifications are:

3-slot mainframe with built-in GPIB and RS232 interfaces
6 1/2-digit (22-bit) internal DMM, scanning up to 250 channels per second
8 switch and control plug-in modules to choose from
Built-in signal conditioning measures thermocouples, RTDs and thermistors, ac/dc volts and current; resistance; frequency and period
50k readings of non-volatile memory holds data when power is removed
Hi/LO alarm limits on each channel, plus 4 TTL alarm outputs
Free BenchLink data logger software to create tests without programming

Figure D.11: Agilent 34970A data acquisition unit

KEYSIGHT TECHNOLOGIES. 2014. *34970A Data Acquisition / Data Logger Switch Unit.* [Online]. Available: http://www.keysight.com/en/pd-1000001313:epsg:pro-pn-34970A/data-acquisition-data-logger-switch-unit?&cc=ZA&lc=eng. [Accessed 25 September 2014].

APPENDIX E: CALIBRATION PROCEDURE AND RESULTS

The following appendix contains the procedure as well as results for the thermocouple probes. The results were used to adjust the measured thermocouple temperatures to a more accurate temperature.

The thermocouple probes where calibrated with a platinum resistance thermometer (ISOTECH 4W model no.: 935-14-72, S/N: 191069) which was calibrated separately at RAPID INSTRUMNETATION (on 4 February 2013, Certificate: RAP15738). A Hewlett Packard 34401A multimeter (S/N: hp3146745396) was used to measure the resistance of the platinum resistance thermometer at particular time which can then be manually related back to an accurate measured temperature. The thermocouples and platinum resistance thermometer were placed in a custom aluminium billet (able to hold 8 thermocouples at a time) which was then slotted into a FLUKE Metrology Well (S/N: B29291). This allowed the thermocouples and platinum resistance thermometer to be exposed to the same temperature which was set on the FLUKE Metrology Well. Lastly, the Agilent 34970A Data Acquisition Unit (S/N: 398470) together with 34901A plug-in module (S/N: MY41141227) and USB converter (S/N: MY52293667) was used to acquire temperature measurements from the thermocouples.

The calibration certificate indicates that the platinum resistance thermometer was calibrated for 0 ºC, +50 ºC, +100 ºC, +180 ºC and +300 ºC. However the experiments conducted during the project would not exceed 50 ºC and therefore the calibration set points were limited to 0 ºC, +50 ºC and +100 ºC. A maximum of eight thermocouples were tested at a time for a particular calibration set point. During each thermocouple set, a measurements were only taken once the thermocouples readings and platinum resistance thermometer readings were steady. A single calibration test thus entailed comparing the thermocouple readings for a particular thermocouple set to the corresponding platinum resistance thermometer reading at each calibration set point. The entire procedure was done for 17 thermocouples (2 thermocouple sets) in total and repeated three times. The resistance readings for the platinum resistance thermometer was converted to reference temperature readings by use of the calibration certificate. The degree of uncertainty for the platinum resistance thermometer as stated on the calibration certificate is ±0.7 °C at all calibration set points. Figure E.1 shows the average error for the various thermocouples probes from the platinum resistance thermometer reference temperature over the three calibration tests at the three calibration set points.

Here it is shown that the average thermocouple error from the platinum resistance thermometer reference temperature does not exceed ±0.3 °C. The thermocouple probe results were then linearly fitted between 0 ºC and 50 ºC to match the platinum resistance thermometer reference temperature. The following Equation (E.1) relates the platinum resistance thermometer reference temperature and the thermocouple probe readings, where the coefficients are listed in Table E.1.

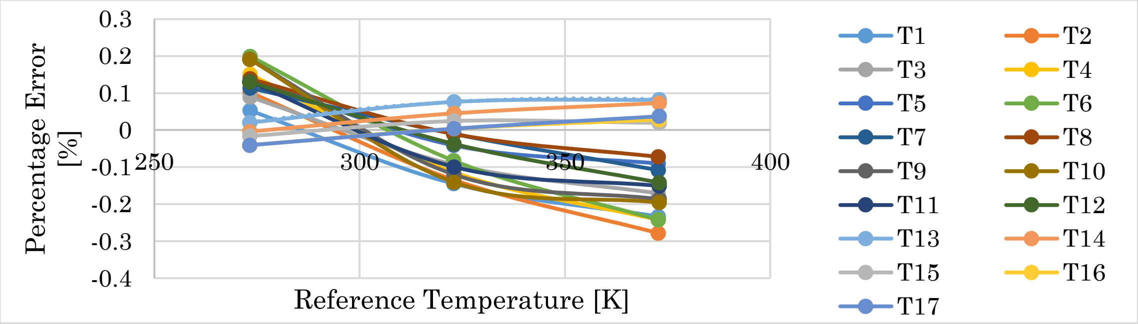

Figure E.1: Percentage error of each thermocouple as compared to the platinum resistance thermometer reference temperature at three calibration set points

$$T_{adjusted} = mT_{reading} + c \tag{E.1}$$

Table E.1: Calibration coefficients for linear curve fit

Probe	m	c	R^2
T_1	1.0124	-0.1477	0.9990
T_2	1.0145	-284.0000	0.9990
T_3	1.0111	-0.2485	0.9990
T_4	1.0159	-0.4201	0.9990
T_5	1.1040	-0.3827	0.9990
T_6	1.0166	-0.5560	0.9990
T_7	1.0070	-0.3137	0.9990
T_8	1.0083	-0.3818	0.9990
T_9	1.0181	-0.5305	0.9990
T_{10}	1.0196	-0.5323	0.9990
T_{11}	1.0134	-0.3609	0.9990
T_{12}	1.0093	-0.3592	0.9990
T_{13}	0.9958	-0.0547	0.9990
T_{14}	0.9965	0.0115	0.9990
T_{15}	0.9972	0.0450	0.9990
T_{16}	0.9972	0.1111	0.9990
T_{17}	0.9972	0.1111	0.9990

APPENDIX F: SUNDRY READING

The following appendix contains sundry material considered during the research for the topic of surface tension driven pumping. More information on topics of surface tension and plant physiology are listed here to gain a deeper understanding on the subject at hand.

F.1. Surface Tension

This sundry material refers to surface tension, how it might be implemented, how it may be measured, further examples of Marangoni flows and finally thin film spreading.

F.1.1. Young-Laplace Implementations

Figure F.1 and Figure F.2 show a sessile drop and a wetting liquid next to a plane vertical wall, respectively. The usual procedure is to define a function $z = z(x, y)$ or $z = z(r)$ depending on whether the problem is stated in Cartesian coordinates or permits a symmetrical axis of revolution. For the sessile drop in Figure F.1, $z = z(r)$ is chosen and the primary radius is then given by:

$$\frac{1}{r_1} = \frac{{d^2z}/{dr^2}}{\left[1 + \left({dz}/{dr}\right)^2\right]^{3/2}} \tag{A.1}$$

And the secondary radius by:

$$\frac{1}{r_2} = \frac{{dz}/{dr}}{r\left[1 + \left({dz}/{dr}\right)^2\right]^{1/2}} \tag{A.2}$$

For the vertical plane and a free liquid, as seen in Figure F.2, $z = z(y)$ and the primary radius is given by Equation A.1 but in terms of y instead of r. The secondary radius is equal to zero as the free surface is seen as an infinite plane. The next step is to relate these curvatures to the Laplace pressure and solve the resulting differential equations. These steps are presented clearly in Carey (1992) and may be viewed for further interest. For the sessile drop it can be found that the maximum diameter is found at $\Omega = \theta$

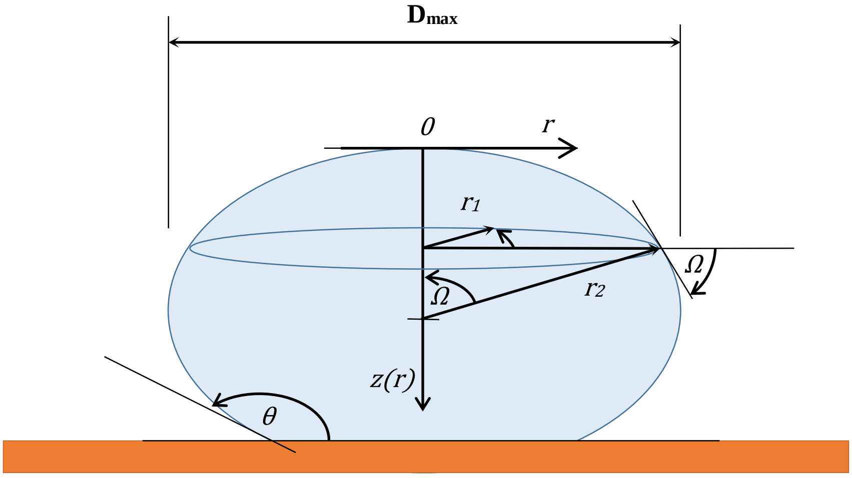

Figure F.1: Sessile drop [Modified from Carey (1992)]

For a free liquid in contact with a vertical wall, the height at which the liquid climbs up the vertical can be found to be: (Carey, 1992)

$$z_0 = z(0) = \left[\frac{2\sigma\left(1 - \sin(\theta)\right)}{(\rho_l - \rho_g)g}\right]^{1/2} \tag{A.3}$$

where g is gravitational acceleration and θ is the contact angle. The contact angle is always defined to be the angle between two lines which are respectively tangent to the solid and liquid interface (Çengel and Cimbala, 2010). The phenomenon observed in Figure F.2 where the liquid free surface rises at the contact line with a solid vertical wall, will occur in a similar manner for liquids in small tubes and porous media.

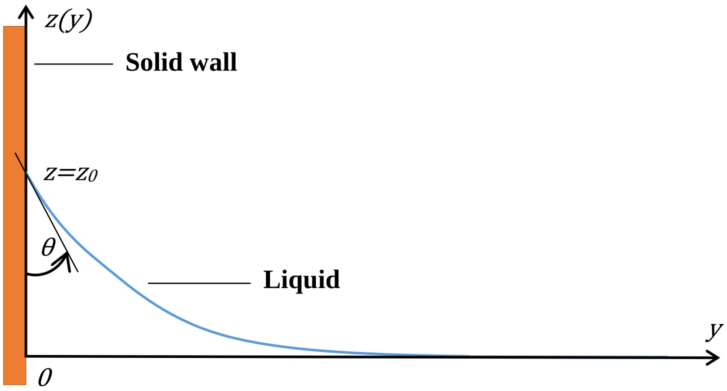

Figure F.2: Free wetting liquid next to a plane vertical wall [Modified from Carey (1992)]

F.1.2. Surface Tension Measurement

Surface tension may be noticeable in various ways and therefore a multitude of measuring methods are available. The optimal method depends on the liquid itself, its stability as well as the measuring conditions. It is however extremely difficult to measure surface tension accurately without precise and accurate lab equipment and conditions. Typical methods require expensive well balanced and calibrated balances, tensiometers or even optical equipment (Roman et al., 2000). Following are some well-known surface tension measuring methods:

- *Du Noüy ring:* One of the oldest methods employed to measure surface tension. This method utilises the interaction between a surface being tested with a platinum ring. The ring is submerged below the liquid surface and is then pulled from the surface. This lifts the meniscus of the liquid until the meniscus tears. This maximum force required to break the ring free from the liquids surface is then measured, typically through a force tensiometer. This method is relatively simple and minor compensations have to be made (PHYWE, 1998; Attension, 2012).

- *Wilhelmy Plate:* This method is a highly accurate and easy method to measure surface tension at equilibrium conditions. A very thin plate, typically platinum, is attached to a balance or tensiometer. The wetted plate is brought into contact with the heavy liquid, but not submerged in it. A zeroth depth is set and the liquid raised and dropped again to the zeroth depth. This ensures complete wetting of the surface. The force is then registered and used to calculate the surface tension (Attension, 2012; Butt et al., 2006). Figure F.3 shows a simple force diagram of the Wilhelmy plate.

  $$F_M = F_s \tag{A.4}$$

  where

  $$F_\sigma = p\sigma\cos\theta \tag{A.5}$$

  and p is the perimeter. Thus:

  $$\sigma = \frac{p\sigma\cos\theta}{F_M} \tag{A.6}$$

  In application the contact angle is rarely used and due to complete wetting assumption:

  $$\theta \sim 0° \tag{A.7}$$

  This then presents and easy and effective method for surface tension measurement which does not require any correction factors.

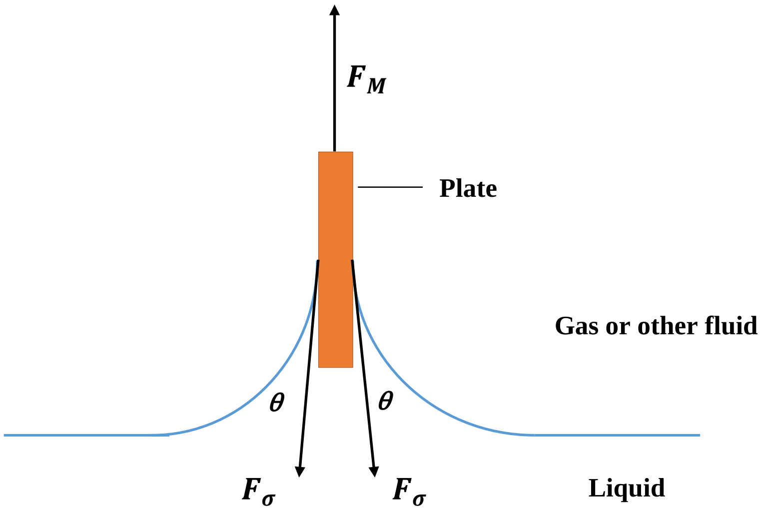

Figure F.3: Force diagram of Wilhemly plate

- *Optical tensiometry:* This involves measuring the geometry of drop optically. This is also called the pendant drop analysis. A drop of liquid hanging from a syringe tip is analysed and the shape determined. A force balance is applied to ultimately determine the surface tension. The Young-Laplace equation is applied and with advances made in numerical methods have made this technique quite affordable and easy to implement. High accuracy measurements on low volumes and low surface tension liquids can be obtained. This method is mostly applied for pure liquids however this technique can also be applied for complex solutions. (Attension, 2012; Gaddum, 1931)

- *Bubble pressure method*: This method attempts to measure the pressure difference of the interface and applies the Young-Laplace equation to determine the surface tension. Typically suited for young surfaces, this technique can be effectively applied to soapy solutions etc. The advantages of this method is that no careful handling of equipment is necessary, nor are highly sensitive force measurement devices necessary. (Roman et al., 2000)

- *Other*: Most other methods are simple variations of the previously discussed methods. The Du Noüy method may be adapted to use a small diameter metal needle instead of a ring. This minimised version allows for much smaller sample volumes and there is no need to correct for buoyancy. This method however requires a highly accurate and sensitive microbalance. A variation on the Wilhemy plate method is the use of a platinum rod or probe. This is quite useful when there are limited quantities of the sample liquid. The probe is lowered into a small diameter tube containing the liquid and levelled at the interface and the force recorded. This method is less accurate than the plate method due to higher accuracy equipment being required as well as the effect of the meniscus if the tube diameter is too small in comparison to the probe diameter. Capillary rise can also be used to determine surface tension. Other optical methods include spinning drop method and sessile drop method.

F.1.3. Marangoni Effect

Marangoni flows are characterised by fluid motion due to surface tension gradients at the interface (Carey, 1992). There are also other methods, besides surface tension gradients, to achieve motion from surface tension; and therefore not Marangoni effects. An example is simply vector control where advantage is taken from contact angle manipulation, such as the larva of Pyrrhalta employs to evade predators (Sang Kug et al., 2009).

Temperature Effects

A special case of liquid flow induced by temperature related surface tension gradients are Bernard circulation cells. Due to localised temperature differences a steady flow can be achieved as seen in Figure F.4.

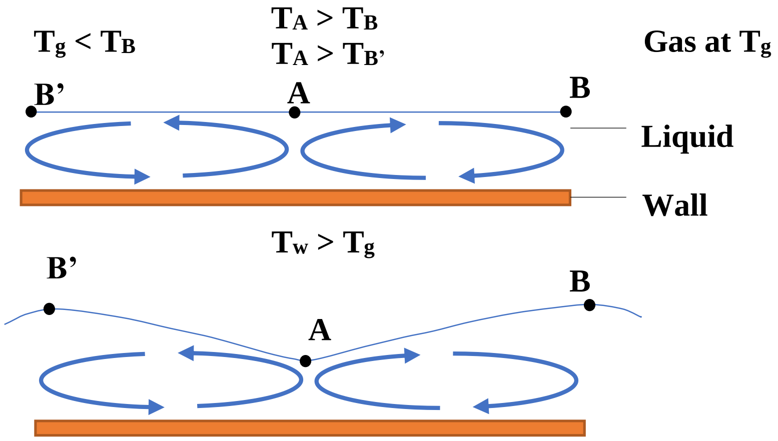

Figure F.4: Cellular driven flow by surface tension [Modified from Carey (1992)]

At steady state, warm liquid flows upward to point A and then turns and flows toward either points B or B'. Due to convection heat losses to the surrounding cooler gas, the temperature at B and B' is less than the temperature at A. The surface tension gradient is therefore maintained, and liquid is pulled from point A to B and B'. Due to symmetric convergence at points B and B', the flow is forced downward upon which it then obtains heat from the wall and the cycle repeats. In some cases, the cellular flow may even cause interfacial deflection as seen in Figure F.4. (Carey, 1992) Another example of where temperature variation is used to induce the Marangoni effect is work done by Okawa et al. (2009), where a laser is used to locally heat the back side of a small object floating on the interfacial surface.

This results in the local decrease in surface tension of the liquid at the back of the object and a surface tension gradient is produced. This then propels the object forward.

Contaminant Effects

Surface tension gradients may form due to the local addition of surfactants into a liquid. This rapidly drives liquid and surfactant from the source to regions of higher surface tension. The addition of the surfactant causes a shock to develop near the leading edge of the surfactant front. In thin film applications this can result in film rupture. More on surfactant wave propagation and spreading can be found in Bull and Grotberg (2003).

As discussed previously interesting flow phenomena may occur due to interfacial tension gradients, such as Bernard cells. Interfacial turbulence or qausi-cellular flow patterns may also emerge due to one or more species being transferred across a liquid-vapour interface. These irregular flows are somewhat periodic in nature and are driven by interfacial concentration gradients. Concentration typically dominates any temperature effects regarding the variation in surface tension. Interfacial turbulence plays a significant role as it greatly enhances heat and mass transfer at the interface.

Marangoni flows can also arise due to evaporation from liquid films in two-phase flow and can be of particular importance in multicomponent systems. Depending on the nature of the multicomponent system, the Marangoni effect may act to destabilise or stabilise the interface. Examples include falling film of a binary liquid mixture on a heated vertical plate. If the more volatile component has a higher surface tension, the Marangoni flow may cause a transverse wavy perturbation of the liquid film interface. The resulting thinner film regions would consequently result in more rapid evaporation of the volatile component and therefore flow is drawn to the thicker film regions due to a concentration gradient. Here the Marangoni effect promotes film breakup into rivulets or streams. However, if the more volatile component were to have a lower surface tension, film breakup or rivulet formation would be opposed. Similarly, droplet spreading on a warm surface can be affected by interfacial tension brought on by concentration gradients, as shown in Figure F.5. Once again consider a binary liquid mixture where the more volatile component has a lower surface tension. Around the perimeter of the droplet, the droplet thickness is at its lowest. The evaporation of the volatile component would thus be increased in this region and therefore result in a concentration gradient which produces a surface tension difference that pulls liquid from the bulk droplet to the advancing perimeter and effectively enhances this motion. This overall increases the spreading rate of the liquid over a solid. Another quite common occurrence is the formation of “wine tears”. This too is a result of the Marangoni flow of the spreading of binary liquid mixtures. Effectively, wine can be seen as a mixture of water and ethanol. Ethanol is more volatile than water and has a lower surface tension. This results in a similar proses as describe before and Marangoni flow allows enhanced liquid spreading up the walls of the wine glass until enough liquid accumulates to form droplets or "tears" which then run down the glass (Carey, 1992).

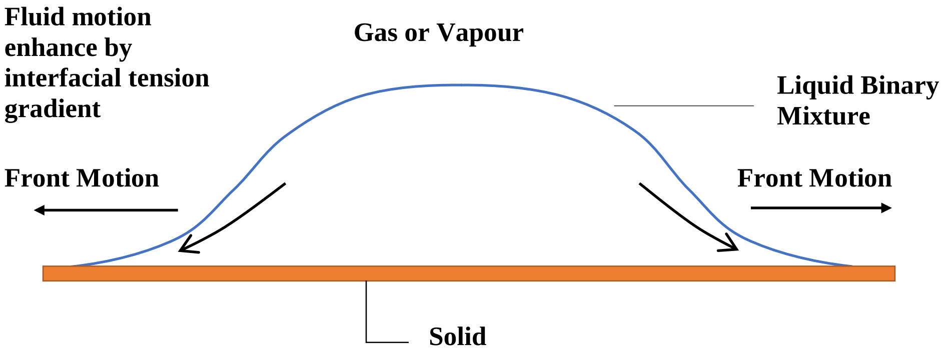

Figure F.5: Droplet spreading on a warm surface [Modified from Carey (1992)]

F.1.4. Thin Film Spreading

As mentioned in before in the case of a positive spreading coefficient for liquid on a solid, the liquid will spread into a thin film over the solid surface. Thin film spreading is to be expected for liquids with low surface tensions and high surface energy solids. As seen in Figure F.6, liquid helium is contained in a Dewar flask spontaneously spreads up the walls of the flask, against gravity, over the rim and forms a thin film on the outside of the flask which either evaporates or drips of the bottom of the flask.

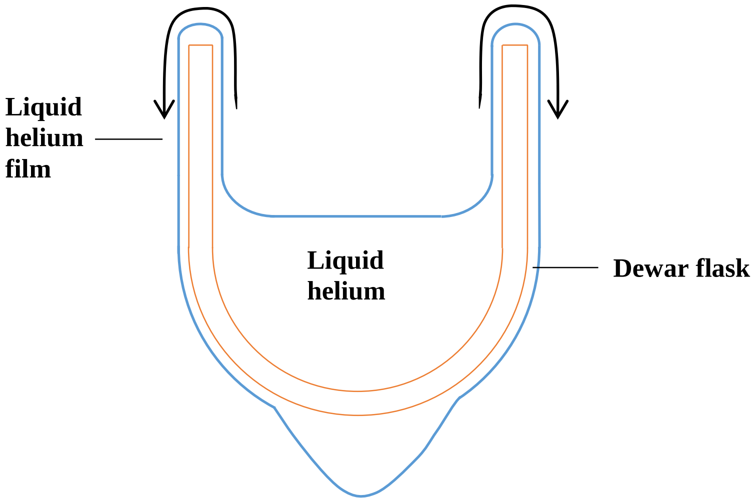

Figure F.6: Liquid helium spreading in a Dewar flask [Modified from Carey (1992)]

The reason for this occurrence is due to the extremely low surface tension of liquid helium (σ_{LV} below 1 mN/m) and the rather high surface tension of the glass-gas/vapour interface (σ_{SV} greater than 500 mN/m). Therefore the adhesion forces are much greater than the cohesion forces involved which results in spreading of the liquid helium. Another example would be low viscosity oils which spontaneously spreads on most metal and non-metal surfaces, for similar reasons as mentioned before (Carey, 1992). With thin films, the concept of disjoining pressure arises. The disjoining pressure (P_d) is defined as the pressure that arises due to the attractive forces between the liquid molecules and solid interface. As the film thickness decreases, the attractive forces act to pull the liquid into the layer as if the liquid layer's pressure were below ambient pressure.

The disjoining pressure is taken to be negative, if the affinity of the liquid for the solid draws liquid into the film. The attractive forces between the liquid molecules and those of the solid surface are expected to increase, and therefore the disjoining pressure as well, as the film thickness decreases. The total pressure required to separate from the surface due to the thin film presence is:

$$P_{tot} = P_{amb} - P_d \tag{A.14}$$

where P_{amb} is the ambient pressure and P_d is the disjoining pressure which is a function of the film thickness (δ). Considering the case where a free fully wetting liquid is in contact with a vertical plane wall, similar to Figure F.2, an extended meniscus exists. The extended meniscus can be divided into two regions, namely an intrinsic meniscus and thin film region. The intrinsic meniscus is defined to be the portion where the disjoining pressure is negligible and the Young-Laplace equation dominates the meniscus profile. Figure F.7 shows the extended meniscus formed where a highly wetting liquid contacts a solid wall (Carey, 1992).

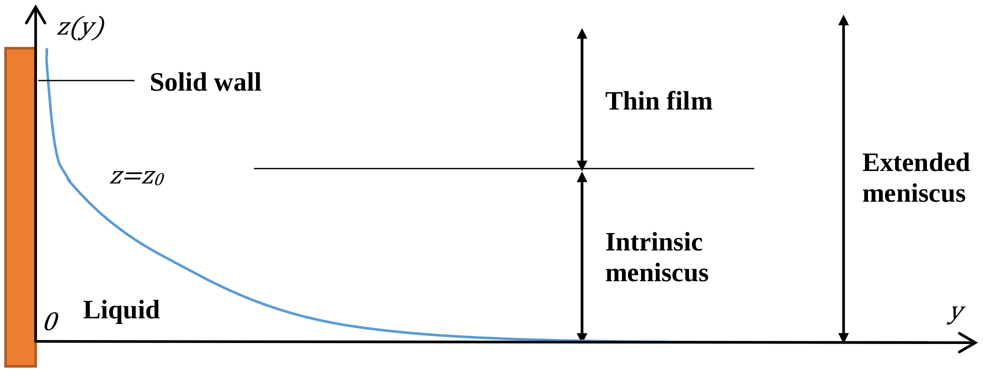

Figure F.7: Extended meniscus due to highly wetting liquid [Modified from Carey (1992)]

Further analysis of this case, where the extended meniscus is in equilibrium and there is no evaporation, can be found in Carey (1992). It can be shown that the disjoining pressure difference ultimately supports the thin liquid film against gravity. A decreasing film thickness gradient results in a disjoining pressure which is equal to the hydrostatic pressure gradient. Further complexities and aspects of the extended meniscus as well as transport during evaporation of an extended meniscus can be evaluated.

F.2. Plant Physiology

The following section contains basic background information for plant studies, plant cellular structures which include material transport structures as well as a detailed description of the internal leaf area.

F.2.1. Plant Overview and Terminology

Plant life is an essential part of human life and without it our daily lives would be rather impossible. Oxygen which is a by-product of photosynthesis sustains aerobic life and many valuable resources and numerous industrial and medicinal products are provided by plants. There are many various and diverse plant species found in nature, ranging from fresh water, sea and land based plants and can vary in size from microscopic algae to Giant Redwoods. Botanists divide the plant kingdom into two large groups: *vascular* and *non-vascular*. Vascular plants are defined to have a well-developed vascular system or -tissues which transports water and solutes to various body regions. Non vascular plant are known to have very simplistic to no internal transport systems. A definitive vascular system is much more typical plants and it has been that there are much fewer non vascular species (chiefly algae and bryophytes) in nature than vascular species. The majority of vascular plants are seed producing and sub divided into *gymnosperms* and *angiosperms*. Gymnosperms mainly include needle leaved conifers such as pines and redwoods, where angiosperms are flowering plants such as broad leaved trees (maple and oaks), vegetables (potatoes and carrots), grasses and others plants such as roses and daffodils. Flowering plants are further dived into two classes, informally referred to as, *monocots* and *dicots*. There are many similarities which include a shoot system consisting of stems and leaves as well as flowers that serve as reproductive system. The main difference is that monocot seeds have a single *cotyledon* where dicot seeds have two. In seed bearing plants, cotyledons are leaf like structures that are part of the plant embryo which upon germination either emerges or remains within the seed and starts to grow. Other differences are found in Table F.1: (Starr et al., 1978; Brower, 2013)

Table F.1: Distinct differences between monocots and dicots

[Modified from (Starr et al., 1978; Speer, 1995)]

	Monocots	**Dicots**
Cotyledons in embryo	single	double
Floral parts	Occurs in multiples of three	Occurs in multiples of four and five
Leaf veins	Parallel	Reticulated (net like)
Pollen grains	Single pore or furrow	Three pores or furrows

Vascular system	Usually scattered	Ring like
Roots	Adventitious roots which form fibrous or fleshy root system	Primary root forms strong taproot with smaller secondary roots
Secondary growth	Absent	Often present
Growth form	Mostly herbaceous with few tree like	Herbaceous or woody

Each plant species is unique, however they all share a common structure: the plant body consist of roots, stems and leaves. Through the process of photosynthesis sugars are produced and transported, together with water and minerals, to various locations in the plant body in similar fashions. Environmental factors such as predation and competition, ambient temperature, light intensity, rainfall, humidity as well as gravity affect all plant species and they must be able to adapt to an ever changing environment (Brower, 2013).

F.2.2. Plant Tissue and Cells

Tissue is defined as a group of intermolecular substances and cells functioning together as to perform some specialised activity e.g., water conduction. All vascular plants have two different organ systems, namely the *root* and *shoot* system. The root system is usually underground and absorbs water and minerals, where the shoot system is found above ground and absorbs light needed for photosynthesis. *Primary growth* originates in the root and shoot tips and as these tissues grow allow for roots, stems and leaves to increase in length. *Secondary growth* is also prevalent in many vascular plant species and results in an increase in girth at older root and stem regions e.g. woody parts in trees (Starr et al., 1978; Brower, 2013; Campbell and Reece, 2008).

Meristems are regions of continuous cell division and growth. Here cells are produced that quickly specialise and become permanent tissue and lose their ability to divide further. Three main types are distinguished: *ground*-, *vascular*- and *dermal* tissues (Starr et al., 1978; Brower, 2013; Campbell and Reece, 2008).

Ground Tissue

Ground tissues make up the bulk of the plant body and provides photosynthetic sites, a support matrix for the vascular tissue and helps store water and sugars as well as. Further, ground tissue is subdivided into three types: *parenchyma*, *collenchyma* and *sclerenchyma*. A short summary of these ground tissue cells can be found in Table F.2 derived from Campbell and Reece (2008) and Starr et al. (1978).

Table F.2: Summary of ground tissue

	Parenchyma	Collenchyma	Sclerenchyma
At maturity	- Live cells - Most prominent cells in plant body - Least specialised cells - Retains its ability to divide into other plant cells	- Live cells - Found in Stems and leaves	- Dead cells - Found in mature parts of plant
Functions	- Metabolic functions - Allows CO_2 and O_2 diffusion in leaves	- Provides flexible support - Does not restrain growth - Elongates with plant	- Provides structural support - Protects seeds and nuts
Structure	- Has a thin flexible primary walls - Lacks secondary walls - Has large central vacuoles	- Grouped in strands beneath dermal tissue - Has thick and uneven primary cell walls - Lacks secondary walls	- Forms continuous long strands or sheets - Sometimes scattered among other cell types - Sometimes impregnated with lignin - Can be subdivided into sclereids (short, thick and irregular) and fibers (long, slender and arranged)

In Figure F.8 light microscope images of parenchyma, collenchyma as well as sclerenchyma can be found. Here it is possible notice the structure of the cells as described in the above table.

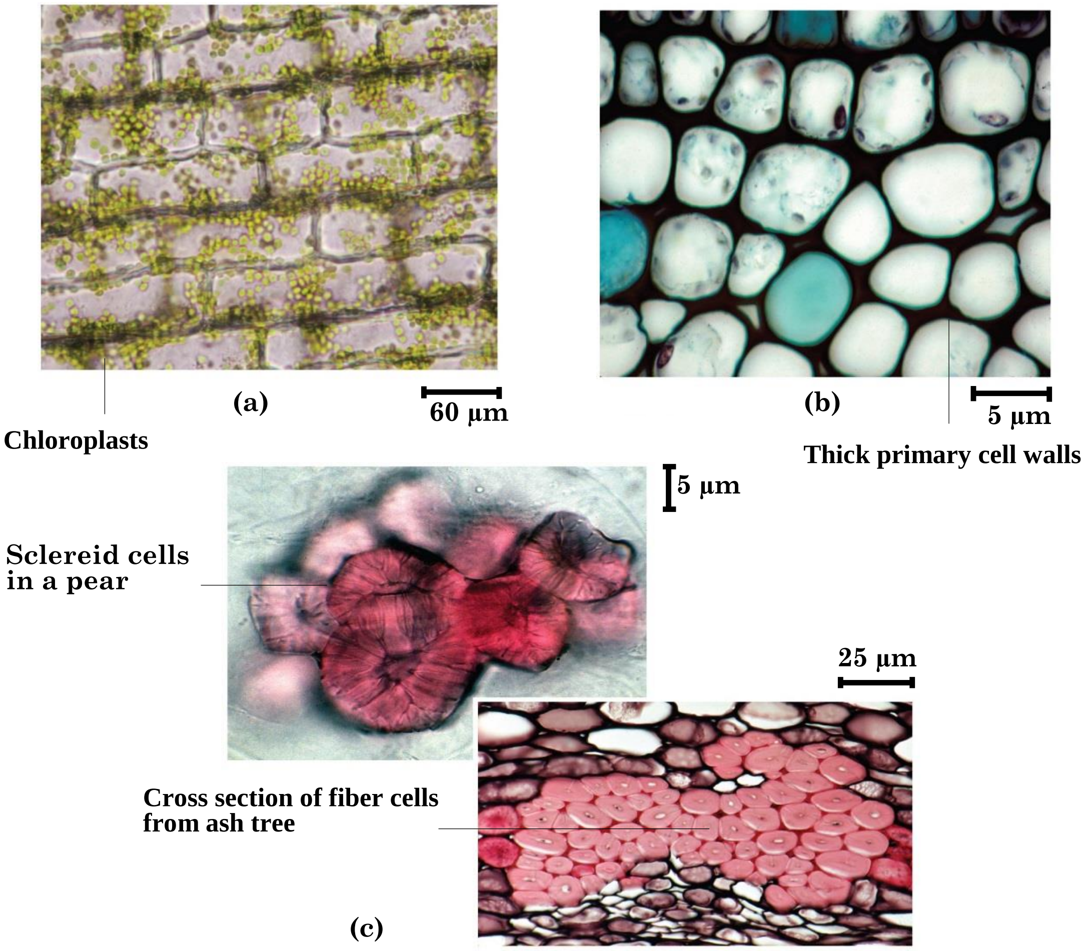

Figure F.8: (a) Parenchyma cells in *Elodea* leaf with chloroplasts; (b) Collenchyma cells (in *Helianthus* stem); (c) Sclerenchyma [Modified from Campbell and Reece (2008)]

Vascular Tissue

Vascular tissue transports water, minerals and sugars to various regions of the plant body and is threaded throughout the ground tissue. There are two main types of vascular tissue called *xylem* and *phloem*. A brief summary of vascular tissue cells is shown Table F.3: (Campbell and Reece, 2008; Starr et al., 1978; Brower, 2013)

Table F.3: Summary of vascular tissue

	Xylem	Phloem
At maturity	- Dead cellulose cells	- Living cells
Function	- Transports water and dissolved minerals absorbed from soil, upward from roots into stem - Lends some mechanical support	- Transports organic nutrients from where they were produced to where they are needed

Categories of cells	- *Tracheid* cells (long cells with tapered overlapping ends) - *Vessel element* cells (Shorter cells joined end to end to form micro-pipes or vessels)	- *Sieve-tube element* cells (common in angiosperms) - *Sieve cells* (mainly in gymnosperms)
Structure	- Both cells have strong thick walls with crisscrossed layers of cellulose, impregnated with lignin - Both contain recesses or pits which matches up with pits in adjacent cells - Water moves through tracheids through pit pairs concentrated at overlapping regions - Water moves through vessels elements either uninterrupted or through a perforated plate	- Thick walled with regions of enlarged *plasmodesmata* (channels connecting adjacent cell cytoplasm) - Only sieve tube members have large pores or sieve plates at end walls. - Joined end to end to form sieve tubes. - Have companion cells that assist in the movement and storage of sugars

Figure F.9 contains colourised scanning electron micrograph images of vessels, tracheids and detailed drawings as visual aid, where Figure F.10 shows phloem sieve tube members.

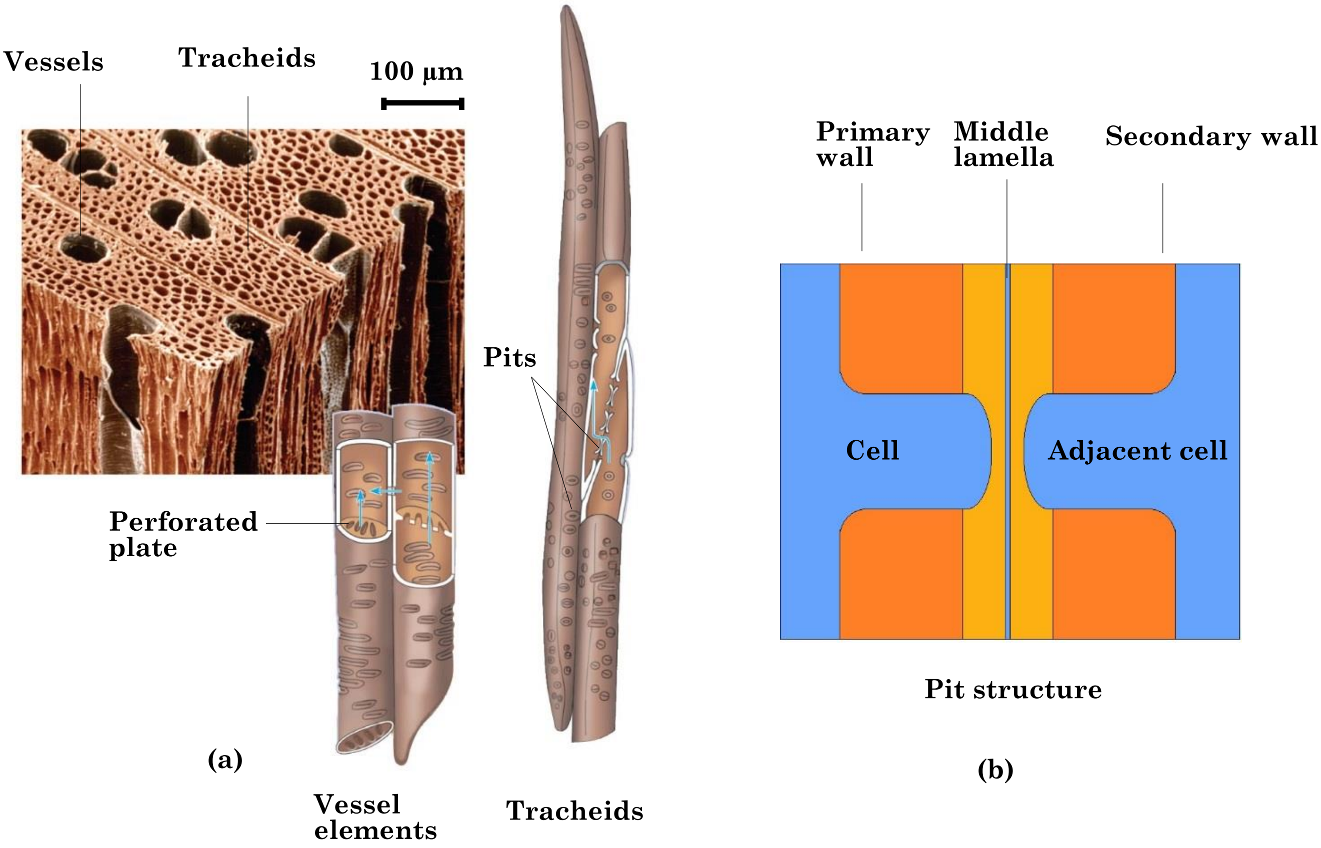

Figure F.9: (a) Xylem; (b) Pit structure
[Modified from Campbell and Reece (2008) and Starr et al. (1978)]

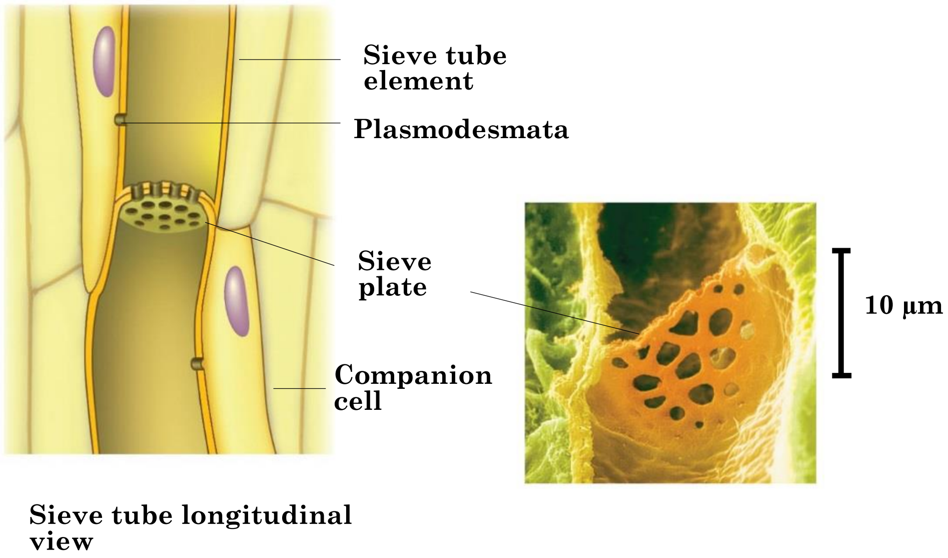

Figure F.10: Phloem: Sieve tube element [Modified from Campbell and Reece (2008)]

Vascular tissue typically occurs in vascular bundles were the vascular bundles found in monocots are smaller and scattered as opposed to the vascular bundles found in dicots which are larger and arranged in a ring-like formation. Figure F.11 shows a typical cross section of a vascular plant stem where (a) is a detailed drawing and (b) is a light micrograph image.

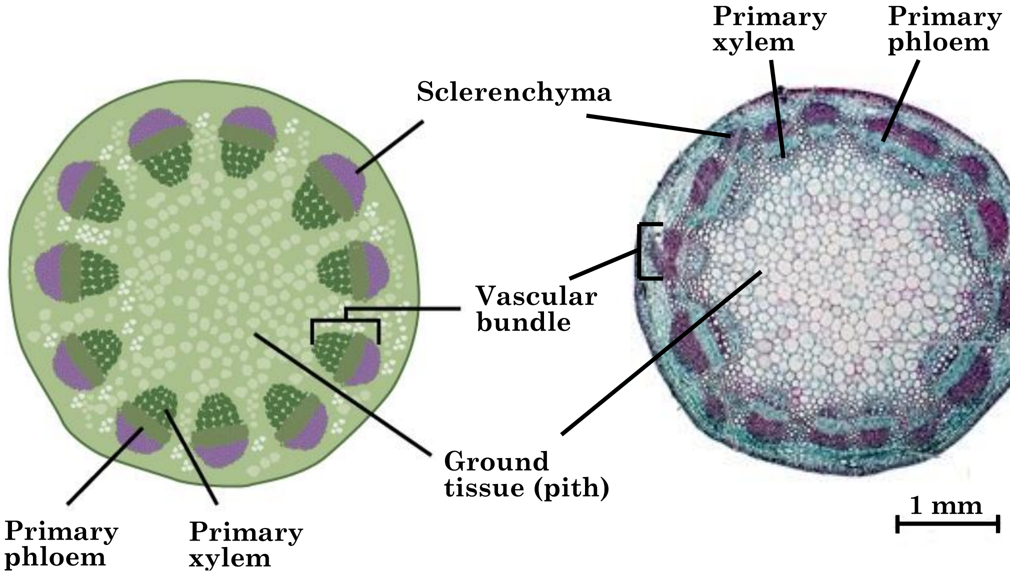

(a) (b)

Figure F.11: Cross section of a typical young vascular plant stem [Modified from Brower (2013) and Campbell and Reece (2008)]

In between the primary xylem and –phloem a thin layer named *procambium* is present which responsible for the growth of primary vascular tissue. Later, as the stem ages, *vascular cambium* forms which results in the addition of secondary xylem and –phloem. This annual formation of new secondary vascular tissue increases the diameter of the stem and gives rise to the so-called year rings present in trees. A further more detailed account on how plant tissue arises from meristems may be found in Starr et al. (1978) as well as Campbell and Reece (2008).

Upon closer inspection, tracheid cells are typically much narrower than vessel members and rely solely on narrow pits to transfer water and solutes to the adjacent cells. Due to this the hydraulic efficiency of vessel members are much higher than that of tracheid cells (Hacke and Sperry, 2001). Typical tracheid diameters and lengths are 5 to 80 μm and 0.1 to 1 cm, respectively, where for vessels they vary between 15 to 500 μm and 1 to 1000 (rare) cm, respectively. Pits allow water to pass through the conducting tissue, but also act as a "safety valve" which protects the adjacent conduits from gas bubbles, due to cavitation, spreading and causing a loss of hydraulic conductivity. Two main pit variations have been observed, namely, pit membrane (or capillary-seal) and torus-margo types. The pit membrane is a very thin membrane, varies from 70 to 500 nm, of uniformly distributed micro-fibrils with a very low porosity and minute pore sizes, raging to as small as 5 nm. This structure thus severely restricts flow where the torus-margo contains centred thickened torus surrounded by a very porous margo (Choat et al., 2008). For further study of pit variations and evolution see Sperry (2003).

Dermal Tissue

Dermal tissue covers the plant body and has the function of protecting the plant. There are two main types known as the *epidermis* and the *periderm*. The epidermis is a continuous layer of tightly packed cells that covers the whole primary plant body where the periderm is a protective cover that replaces the epidermis when secondary growth occurs. The cells found in the epidermis are typically highly specialised, for example, root hairs that increase water and mineral absorption, where the periderm contains non-living cells in its outermost layer that aids to waterproof certain plant regions. More information on dermal tissue and specialised cells may be sourced from Starr et al. (1978) as well as Campbell and Reece (2008).

F.2.3. Leaf Structure and Tissue Organisation

Plant leaves are typically designed to have a high surface to volume ratio and thus have a very large external surface which is exposed to carbon dioxide in the air as well as sunlight. The membranes of photosynthetic cells found inside leaves however present a vast surface area (10 to 30 times greater than the external surface area) for sunlight reception and gas exchange. The outermost layer of the leaf is covered with protective dermal tissue, which consists of an upper and lower epidermis with a cuticle covering. In between the dermal tissue ground tissue and vascular tissue can be found. The ground tissue consists of palisade- and spongy mesophyll cells which are both specialised photosynthetic parenchyma cells. The palisade mesophyll cells are typically elongated and loosely packed on the upper epidermis where the spongy mesophyll cells are packed less dense below the palisade mesophyll with a labyrinth of air spaces in between. This allows oxygen and carbon dioxide to circulate around the cells and up into the palisade region. Around this area between 30 and 50% of the leaf consists of air spaces. The leaf contains a network of vascular tissue called veins which are synonymous with vascular bundles that have a protective bundle sheath. This network provides a skeletal support structure for the leaf as well as permitting photosynthetic tissue to be in close proximity with the xylem and phloem. The xylem brings needed water and minerals to the photosynthetic tissue where the phloem receives the organic products to be transported to various parts of the plant. Finally, small openings or pores are generally found in the lower epidermal layer through which oxygen and water vapour moves out of the leaf and carbon dioxide enters the leaf. These openings are called stomata which consists of two guard cells which regulate the gas exchange from the leaf to and from the environment. The density of stomata on a leaf may be as high as 20 000 per square centimetre and this is under genetic as well as environmental control (Starr et al., 1978; Campbell and Reece, 2008). Figure F.12 shows a detailed drawing of the leaf anatomy as described.

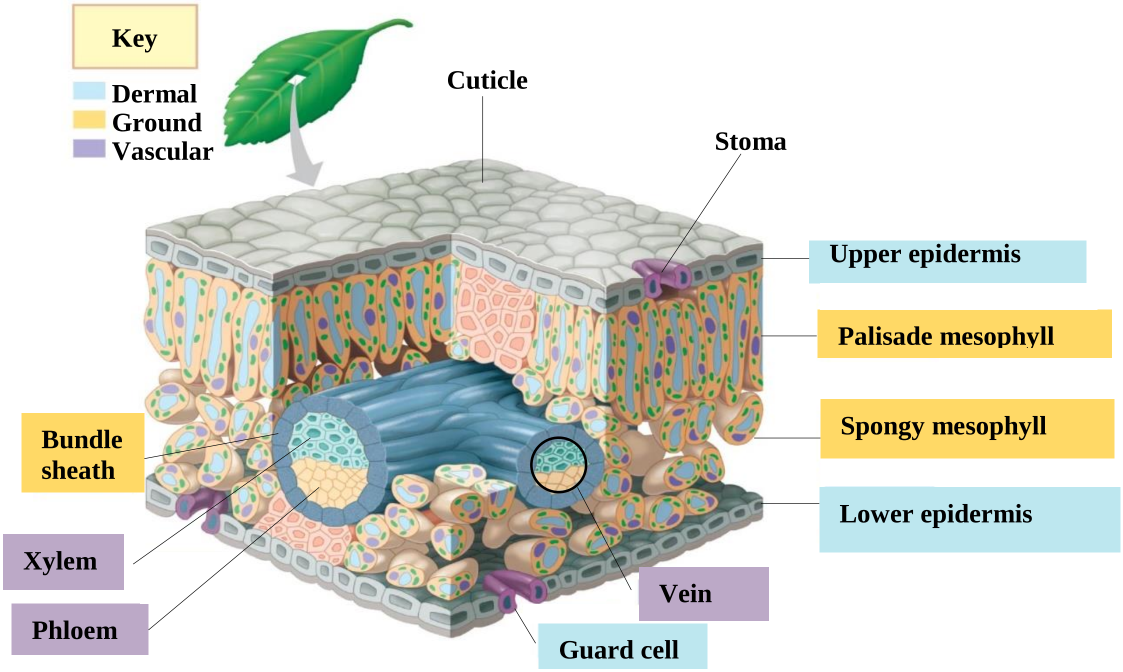

Figure F.12: Overview of leaf anatomy [Modified from Campbell and Reece (2008)]

Figure F.13 (a) shows a light microscope image of a closed *Vicia Faba* (Broad bean) stoma where Figure F.13 (b) shows a light microscope image of open *Commelina communis* (Asiatic dayflower) stomata; both were treated with DNA fluorophore. Additional images of stomata taken are shown Appendix A.1. Guard cells swell under turgor pressure which distorts its shape such that the opening widens. As cellulose micro-fibrils are radially orientated in guard cell walls and as guard cells are joined at the tips, the cells increase more in length than in width when turgor pressure is increased which causes them to bow outward. When turgor pressure decreases the guard cells become flaccid and closes the opening. This mechanism allows the stomata to vary the amount of gas exchange in response to environmental conditions and so limit water loss during drought or at night (Starr et al., 1978; Campbell and Reece, 2008).

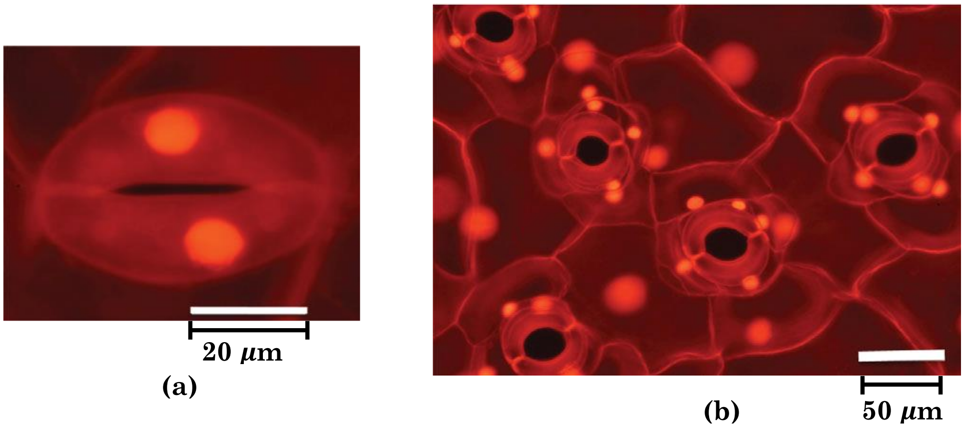

Figure F.13: (a) Closed stoma; (b) Open stomata [Modified from Franks (2012)]

This and further reading on leaf structures, -adaptations, stomatal control as well as photosynthesis can be found in the aforementioned sources. For further interest on topics such as stomatal densities, -structures, liquid penetration of stomata as well as stomatal control and leaf thermal hydraulic capacitances consult articles by Franks (2012), Zarinkamar (2007), Camargo and Marenco (2011), Kouwenberg (2003) and Schönherr and Bukovac (1972) and Schymanski et al. (2013), respectively.